POLITECNICO DI TORINO

Department of Electronics and Telecommunications

Master's Degree in Electronic Engineering

Master's Degree Thesis

Design of innovative Transparent Smart Electromagnetic Skins working in Transmitting Mode

Supervisors
Prof. Paola Pirinoli
Dott. Michele Beccaria

Candidate
Pio Francesco Lupinacci

October, 2024

"Ogni cosa è nel suo raggio in divenire"
(Jovanotti)

Dedicated to Giulia,
the most beautiful gift life has given to me

Acknowledgements

A Febbraio del 2022 lasciavo il mio paese per trasferirmi a Torino. Ricordo ancora le emozioni che ho provato, un misto di ansia e curiosità che ha caratterizzato quei giorni. Ben presto però tutte le paure e preoccupazioni furono spazzate via, grazie a questa città che mi ha dato molto e che porterò sempre nel mio cuore, ma soprattutto, grazie alle persone che conoscevo già e che ho incontrato, le quali hanno reso il tutto ancora più bello.

Prima di tutto, ci tenevo a ringraziare chi, in questi ultimi mesi, mi ha permesso di arrivare a questo punto, guidandomi durante questo percorso di tesi. Ringrazio quindi la prof.ssa Paola Pirinoli per il tempo che mi ha dedicato e per essere stata sempre disponibile e gentile con me, fin dal primo giorno. Inoltre, desidero ringraziare il dott. Michele Beccaria per il suo prezioso supporto e per tutti i consigli che mi ha offerto con esperienza e professionalità, grazie ai quali, il percorso è stato ancora più piacevole. Inoltre ringrazio anche il dott. Andrea Massaccesi, con la quale ho avuto il modo di incrociarmi durante una parte del percorso, per essere stato sempre disponibile.

Un ringraziamento speciale va ai miei genitori e alla mia famiglia, per avermi sostenuto durate questo percorso e avermi dato sempre la forza di rialzarmi quando le cose non andavano per il verso giusto. Grazie a mia sorella Giulia, alla quale ho scelto di dedicare questa Tesi e al forte legame che ci unisce.

Grazie a Martina, per essere stata la mia forza quando non ne avevo. L'idea di una vita insieme migliore al termine di questo percorso mi ha sempre spinto a dare il massimo.

Grazie ai miei nonni, ai miei zii e i miei cugini per tutti i consigli datomi e per avermi dimostrato sempre la loro vicinanza. L'amore che mi date lo porterò sempre con me.

Grazie ai miei amici di giù. Mi avete dimostrato di poter sempre contare su di voi, anche quando la distanza si fa sentire.

Ringrazio la famiglia della mia ragazza, per aver sempre visto con ammirazione il mio percorso.

Infine, grazie ai miei colleghi, sempre pronti a darmi una mano e per essere stati una valvola di sfogo al di fuori dello studio durante questo periodo. Grazie ad Alessandro, per tutto il periodo condiviso durante questi anni e quelli precedenti. Grazie a Tommaso per esserci stato sempre, ma soprattutto per avermi fatto scoprire un posto stupendo. Grazie a Francesco, con il quale è stato formato un duo di successo.

Grazie a tutti voi.

Pio

Abstract

The development of modern communication systems such as 5G, showing enhanced performance despite of no need of additional Base Stations and lower power supply, is made possible by employing among the other devices the so-called Smart Electromagnetic Skin (SES). Thanks to their use, the environment in which the propagation of the signal occurs represents no longer a limitation but a valuable resource and for this reason it is named Smart Electromagnetic Environment (SEE). The reason for relying on this approach is to enhance the performances of these technologies, which requires high data rates wide bandwidth and low latency as main goals. SES are planar or curved surfaces discretized with a suitable number of unit cells with resonant or sub-wavelength size, designed in such a way to provide anomalous reflection or transmission, thanks to which an incident field can be redirected in not Line of Sight (LoS) regions. Strictly speaking, SES are full passive surfaces, able to provide a pre-defined coverage but also reconfigurable configurations, identified as Reconfigurable Intelligent Surfaces (RIS), can be obtained by adding active elements in the unit cells that can be dynamically adjusted. While the usage of these surfaces in reflection mode with the aim to cover blind spots or a pre-defined area and overcome obstacles has been widely investigated in literature, their application in transmitting mode is still almost unexplored. A transmitting SES has the aim to mitigate one of the most problematic issues in dealing with the last communication technologies, i.e. the high loss experienced to the signal due to the penetration through a building, establishing an Outdoor to Indoor Link. This thesis project has the aim to implement this idea, considering a passive innovative SES that can be integrated into a building window. The design of such a structure is challenging, since it has not only to satisfy the requirements relative to its performance, but also to minimally affect the window optical transparency. While the few configurations already discussed in literature are made up with unit cells adopting thin metallizations, the idea exploited here is to design a Dielectric-Only SES, that could be manufactured for instance using an Additive Manufacturing (AM) technique.

The starting point of the carried-out activity is the design of a suitable unit cells; different structure are analysed, characterized by one or more geometrical parameters to control both the provided transmission and reflection coefficients, but always including a layer of glass, that takes into account the presence of the window. While the transmission coefficient is the parameter adopted for the design of the SES, since each unit cell must provide the value of its phase that guarantees the focusing of the transmitting field in the desired direction for a giving incidence, a low value of the reflection coefficient assures reduced back radiation. The most promising unit cells are then adopted for the design of different SESs: the numerical analysis confirms the feasibility of the proposed structures and permits to define which is the most effective unit cell among the introduced ones. In view of these promising results and for their further validation, a Transmitarray Antenna (TA) is designed, that is a planar lens aimed to focus and redirect the incident field radiated by a prime feed, with the purpose realizing a prototype to be experimentally characterized.

Contents

List of Tables

List of Figures

Chapter 1

Introduction

1.1 Introduction

Recently, the possibility to increase the performance of fifth generation (5G) and beyond communication systems through the involvement of the environment in which the propagation occurs is investigated. By properly introducing different devices, a Smart Electromagnetic Environment is designed, in which the objects and obstacles within become key enabling factors, rather than uncontrollable impairments, to achieve an improved Quality of Service (QoS) [1].

Figure 1.1: SEE scenario

Among the different devices that make the environment smart, there are the Smart Electromagnetic Skins (SES), "intelligent" surfaces working in reflection or transmitting mode and able to improve the coverage in a desired area. In particular, the activity carried on during the thesis has been focused on the design of SESs working in transmitting mode and useful for increasing the connectivity between outdoor and indoor scenarios. In fact, if the use of higher frequencies as those in the millimeter band, could have several positive effects on the performance of communication system, it has also some drawbacks, in particular the higher attenuation and the stronger effect of the interaction with the objects along the propagation path. For these reasons, the signal generated from a Base Station (BS) antenna could arrive inside a building strongly degraded. To overcome this problem the proposed solution is that of introducing in the window SES working in transmitting mode, suitably designed to guarantee the coverage inside a building.

The problem is particularly challenging, since the smart skin must not only provide the required performance but also be optically transparent. In view of this, different types of resonant size unit cells have been investigated, even if they differ each others, they are cell characterized by the presence of a layer of glass, to take into account the effect of the window and one/two layers of 3D -printable dielectric material. The most promising solutions have been used for the design of Transmitarrays and smart skins, that have been analysed with a full-wave approach in order to validate their performance.

1.2 Work Objective

In the previous discussion was said that the SESs are introduced to improve the network efficiency exploiting the environment in which they're integrated and that one of the most common environments in which they're used are cities. As already said, mm-wave frequencies are more affected by interaction with obstacles and therefore also by the penetration losses when they propagate through a wall or a window, with the consequent reduction of the indoor coverage.
About this last issue, in [2] there is an explanation about penetration losses for multiple indoor obstructions in an office environment at 28 GHz.

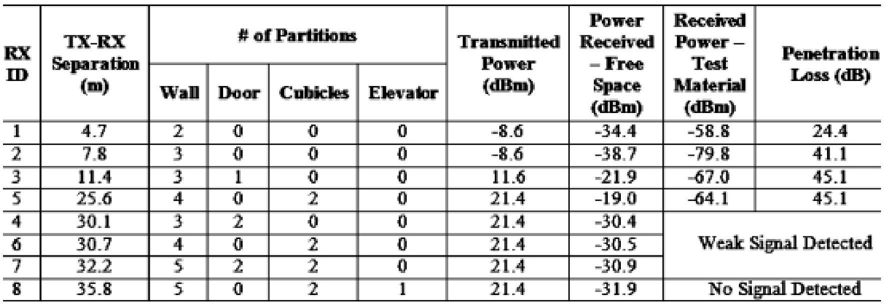

RX ID	TX-RX Separation (m)	# of Partitions				Transmitted Power (dBm)	Power Received – Free Space (dBm)	Received Power – Test Material (dBm)	Penetration Loss (dB)
		Wall	Door	Cubicles	Elevator				
1	4.7	2	0	0	0	-8.6	-34.4	-58.8	24.4
2	7.8	3	0	0	0	-8.6	-38.7	-79.8	41.1
3	11.4	3	1	0	0	11.6	-21.9	-67.0	45.1
5	25.6	4	0	2	0	21.4	-19.0	-64.1	45.1
4	30.1	3	2	0	0	21.4	-30.4	Weak Signal Detected	
6	30.7	4	0	2	0	21.4	-30.5		
7	32.2	5	2	2	0	21.4	-30.9		
8	35.8	5	0	2	1	21.4	-31.9	No Signal Detected	

Figure 1.2: Penetration losses for multiple indoor obstructions in an office environment at 28 GHz [2].

The data are categorized into three sections: signal acquired (that reports the listed values), signal detected, and no signal detected. The first "Signal acquired" refers to locations where the Signal-to-Noise Tatio (SNR) is high enough for accurate acquisition, meaning the penetration loss relative to the 5-meter free space test is less than 64 dB. "Weak Signal detected" refers to locations where the SNR is high enough to slightly distinguish the signal from the noise but not strong enough for full acquisition and "No signal detected" denotes when the penetration loss is at least 74 dB greater than the 5 m free space test.

The activity developed in this thesis actually aims to address this issue with the design of a SES able to focus an incoming beam from a Base Station to an indoor environment. The proposed solution is suitable either for buildings with offices, generally characterized by many windows, either for industrial applications. In both cases the smart skin integrated in the window must be transparent, even if in case in which it is thought for industrial buildings it is sufficient that light passes through. The idea exploited here is that of using a totally dielectric structure, using a suitable material.

1.3 Chapters Organization

The work organization will be as follows. In the second chapter, the device object of this work and the Transmitarray Antenna from which SES derives, are presented. It includes a review of their state of the art and the design procedure.

The third chapter is centered on the unit cells implemented for this purpose, from the layout to the simulation results.

The fourth instead relies on the realization of the structures based on the unit cells introduced in the previous chapter and their numerical analysis.

The final chapter (the fifth) will focus on the realization of one of these structures. In view of the facilities available at Politecnico di Torino for its experimental characterization, the manufacturing of a TA is considered. Since it is developed using additive manufacturing techniques, an introduction to these techniques with the state of the art for 3D printed Transmitarray is provided. Following this, the prototype is described and simulated.

Chapter 2

Planar Transmitting Surfaces

2.1 Transmitarray Antennas Introduction

Merging the best features that stand at the basis of planar phased arrays and lens antennas, a Transmitarray antenna (TA) is obtained[3], that, as already mentioned, is the antenna closest to smart skins working in TX mode. In fact, TA is a particular type of antenna made by an array of elements, named **Unit Cells** (UCs), designed to focus a beam. Today, they can be employed in many sectors such as earth remote sensing, wireless communications, spatial power combining for high power applications, THz images and sensors, and solar energy concentrator. Another very important feature, is that they belongs to the **high gain** antennas. Where with **gain** is intended how much power is transmitted compared to an isotropic source. And for antennas that belongs to high gain category, usually the gain is higher than 20dB [3].

There are two principal parts composing these type of devices: a **feeding** part and a **transmitting** part, as shown in figure 2.1.

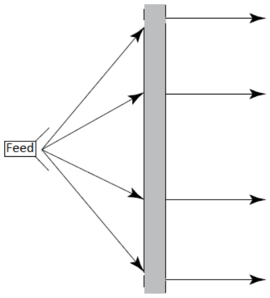

Figure 2.1: TA scheme [3]

And clearly in this type of antenna, the parameter that needs particular attention is the **Transmission coefficient** (S_{21}). It is very important to have a S_{21} as close as possible to 0 dB, but its phase, it will be seen, also plays an important role for the performance.

2.1.1 TAs State of art

In the following, the best TA solutions found in literature are presented. One of the most challenging issues is to obtain a UC which has the transmission coefficient magnitude very close to the ideal value of 0 dB and at the same time, a range variation for the transmission coefficient phase that's at least of 360°. Usually this cannot be reached by a single layer UC and it needs a **multi-layer approach**. A clear example of what is just said is in [4], where a UC based on a double square ring centre patch is designed for a transmitarray antenna at 12 GHz (Figure 2.3 and 2.4). But what is very interesting is the presentation of the improvements that the multi-layer approach takes, indeed the UC was analyzed from a single layer to 4 layers.

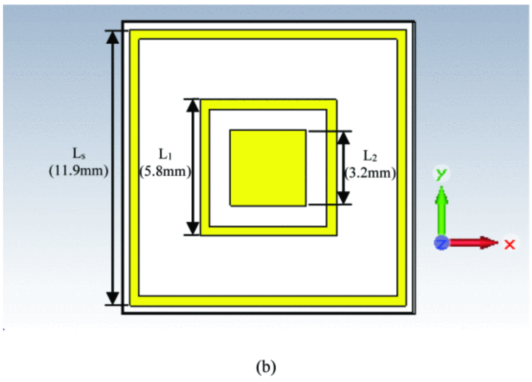

Figure 2.2: UC Front view [4]

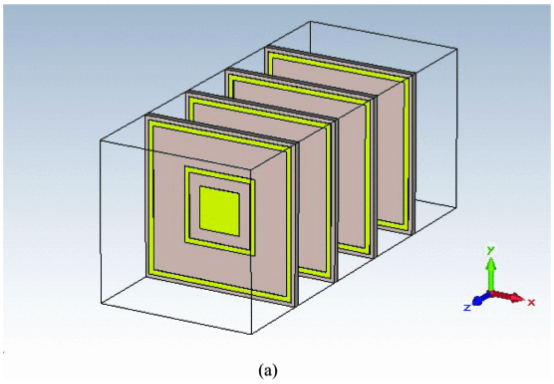

Figure 2.3: 4-layers UC [4]

The transmission coefficient behaviour is studied by varying the length of the side of the external square loop (L_s) and the results is presented in Figure 2.4 and 2.5. Essentially, it is easy to see that the higher the number of layers which composes the UC and the higher the phase coverage for the S_{21} phase.

However, using a high number of layers could increase costs, complexity and also the volume occupied by the entire structure, therefore, an important challenge is to define structures that have good performance with a reduced number of layers. This can be found in [5], where a high performance UC can be obtained with just 2 layers, by loading L-shaped branches and four vias, the UC achieves

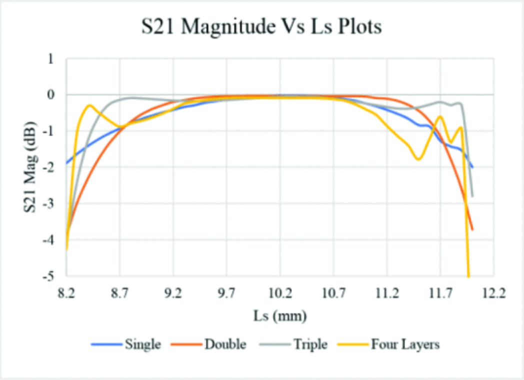

Figure 2.4: S_{21} magnitude [4]

Figure 2.5: S_{21} phase [4]

a low transmission loss and full phase shift in a wide frequency band (the cell is that in Figure 2.6 where the UC evolution is represented).

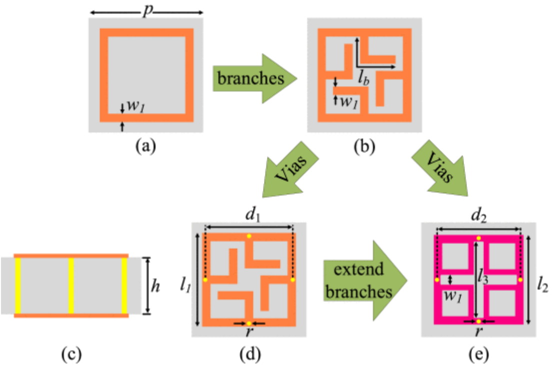

Figure 2.6: UC double layer structure evolution.Top view of (a) the square ring and (b) the square ring loaded L-shaped branches. (c) Side view. Top view of (d) UC I and (e) UC II [5]

The design parameters displayed in UCs are $p = 11\,\mathrm{mm}$, l_1=9 mm, $l_2 = 8.4\,\mathrm{mm}$, $w_1 = 0.8\,\mathrm{mm}$, $r = 0.4\,\mathrm{mm}$, $h = 3\,\mathrm{mm}$, $g = 1.5\,\mathrm{mm}$, while l_b and l_3 are the variable parameter, where $l_b = 0.1$ to 5.6 mm and $l_3 = 2$ to 7.8 mm.

As is possible to observe, two versions of the UC are introduced, this because using just one of the 2 will not cover 360° for the transmission phase. What was just mentioned is reported in the figure 2.8. The fully phase range is achieved merging both plots, while keeping good values of transmission coefficient module.

Another very important challenge in the TA characterization is the band enhancement. In the same paper a TA of 400 elements is fabricated and measured, providing a peak gain and aperture efficiency measured at 12 GHz are 27.1 dB and 52.5 % (Figure:2.8) respectively, but especially a -1 dB bandwidth of 20.4 % or a -3 dB bandwidth of 32.6 %.

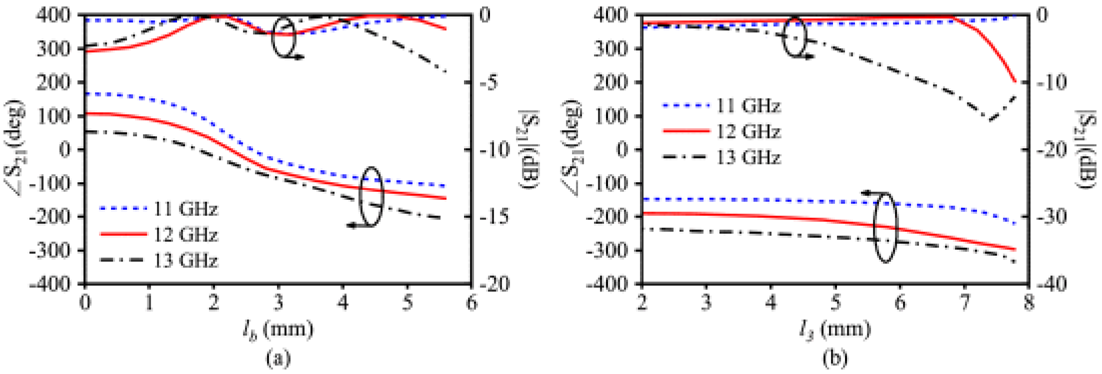

Figure 2.7: S_{21} module and phase [5]

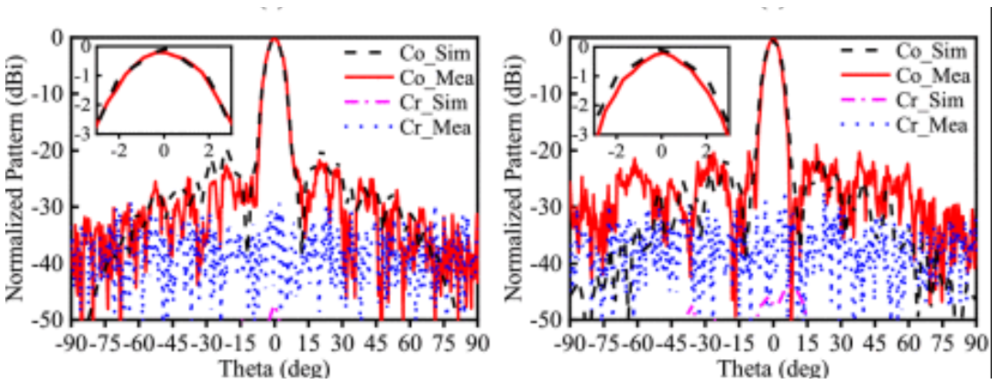

Figure 2.8: Simulated and Measured Gain [5]

Another efficient solution is also presented in [6] where a TA is designed with a particular approach that consists of a semi-planar structure with a reduced transmission coefficient phase from 360° to 51.5° that allows to enhance the bandwidth and efficiency. This is based on the use of a UC as that in Fig. 2.9 done again with the multi-layer approach, but executed in an innovative way, shown in 2.10. Where the number of layers is not always the same but can vary between 2 and 5.

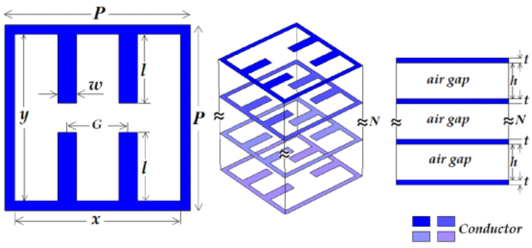

Figure 2.9: UC for wideband application[6]

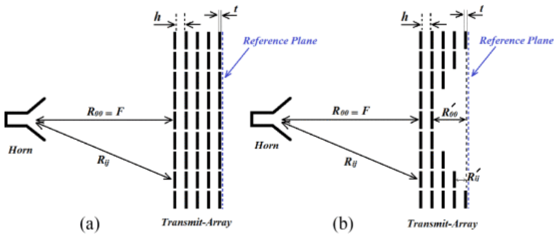

Figure 2.10: ML view [6]

This approach is based on considering for each multi-layer structure just the phase range less sensitive to the frequency as depicted in Figures 2.11 and 2.12. It is also possible to see that the maximum phase range is 51.5°, defined for the 2-layer structure.

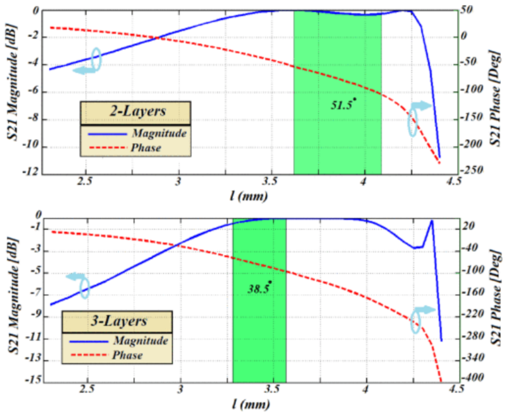

Figure 2.11: Transmission coefficient module and phase for 2 and 3 layers structure [6]

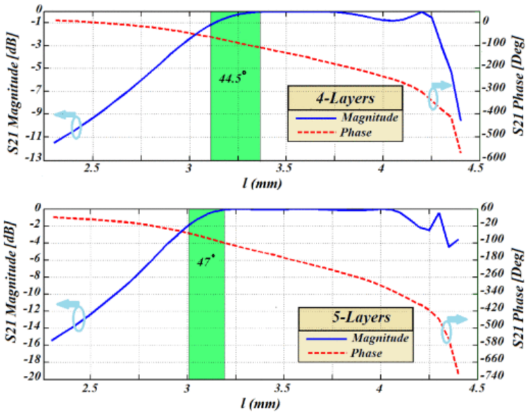

Figure 2.12: Transmission coefficient module and phase for 4 and 5 layers structure [6]

Based on this approach a prototype is designed and manufactured. It will result that at the centre the structure will be composed of just 2-layers, while going out the number of layers increases. It is done at 10 GHz, with a diameter of 15 cm and a $F/D = 0.9$. The results are very important as illustrated at Figures 2.13 and 2.14, that will report a 22.3 dB measured gain, 65 % of aperture efficiency and above all, a measured −1 dB bandwidth of 23.4 %.

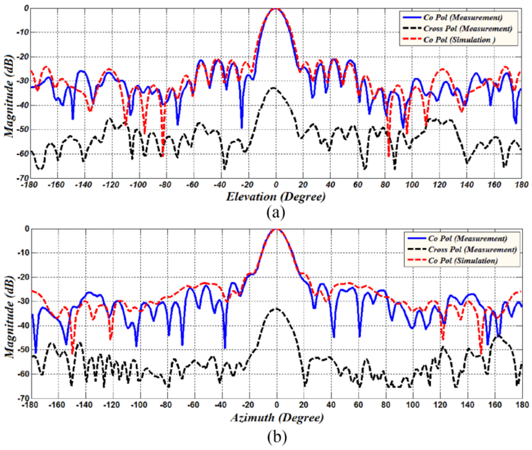

(a)

(b)

Figure 2.13: Gain of UWB structure [6]

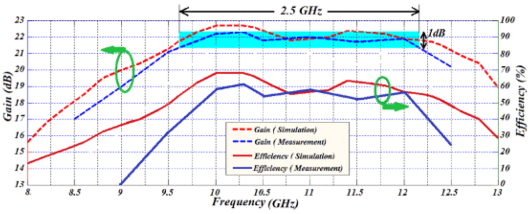

Figure 2.14: Gain vs Frequency of the proposed structure[6]

Particular attention, considering the aim of this work, must be given for the **optically transparent TA** that are present in literature. In [7], a TA who operates in a frequency band from 27.5 GHz to 29.5 GHz is analyzed. It is composed of meshed double-circle rings printed on PMMA substrates, a plastic Optically Transparent (OT) material. This UC covers a phase range about 300° and exhibits a low transmission loss as shown in Figure 2.15:

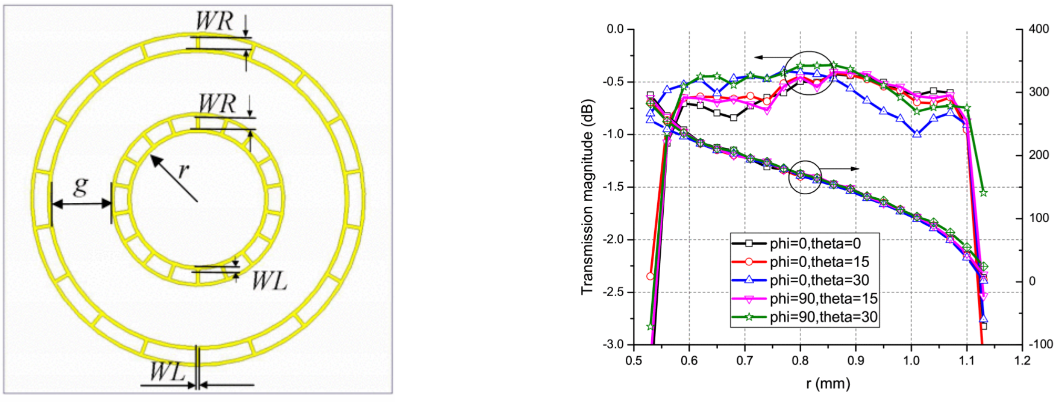

(a)

(b)

Figure 2.15: (a) PMMA UC, (b) Transmission coefficient module and phase [7]

Using this unit cell, a TA is designed and its prototype constructed, where: $D = 9.9 \cdot \lambda_0 = 104.4\,\text{mm}$, where $f_0 = 28.5\,\text{GHz}$ and it's fed with a 2×2 - element array of aperture-coupled microstrip patch (ACMP) antennas positioned at $F/D = 0.5$. The measured results give a gain of 25 dBi and -1 dBi gain bandwidth of 1.8 GHz as shown in figure 2.16.

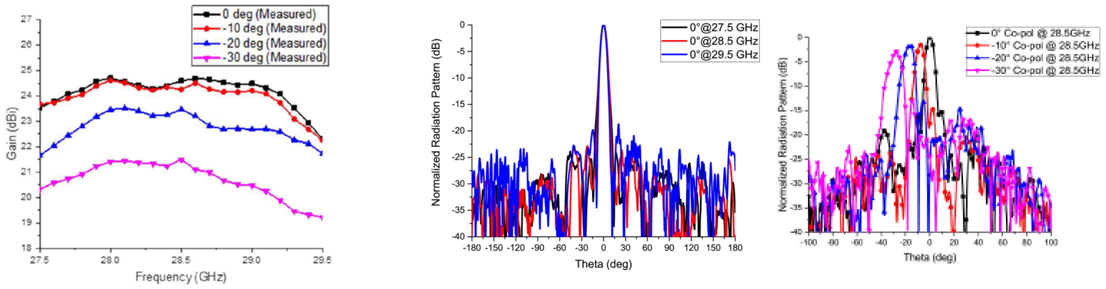

(a)

(b)

(c)

Figure 2.16: (a) Measured Gain vs frequency (b) Normalized Measured Radiation pattern in E-Plane (c) Normalized Radiation pattern in H-Plane[7]

Another example that could be of interest is shown in [8], where again an optically transparent TA is developed, but this time, also a glass window is considered in the design itself. The particularity consists also in having now a very huge dimension TA, that is 720 mm for each side at 28 GHz made by 3 meshed metallic layers and 2 glass substrates. While, 8 UCs are implemented in such a way to cover 315° of phase range as reported in Figure:2.17

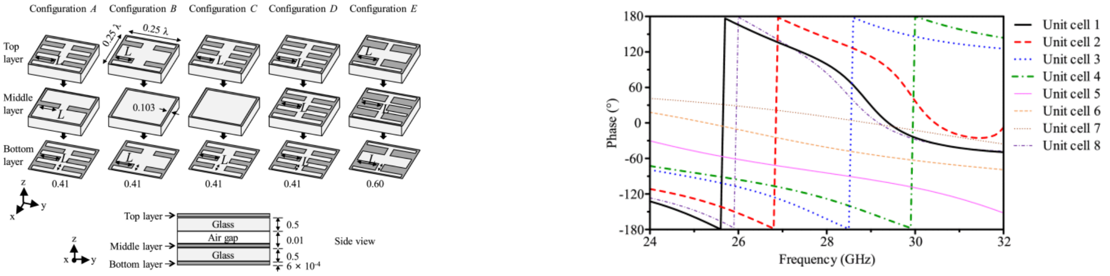

(a) (b)

Figure 2.17: (a) UC configurations (b) Transmission coefficient phase [8]

At first moment the metallic cell layers were fabricated with full copper, but then, in such a way to reduce the transmission loss, it will be substituted with meshed copper. Since the full TA structure will be made by 290x290 UCs, a particular approach to handle this huge dimension is implemented, that consists in analyzing some more little structures made of 15x15 UCs, another of 20x20 UCs and a last of 25x25 UCs. Using this approach, the gain of the entire structure is predicted to be of 37.5 dB-39.3 dB. In order to develop the large aperture TA layout, a specialized process that converts the digital information of the 290 × 290 UCs into a Graphic Data System file (GDSII) using KLayout is developed [9]. Then, the measured gain is reported in Figure:2.18, it presents a peak of 37.5 dB at 28 GHz, but considering the use of a Yagi antenna as feed source, the gain enhancement is 29.7 dB.

Now what has been discussed up to this point is about TAs implemented in multi-layer approach, but clearly, this is not the only way to create TAs. Another way to do this is by **receiver-transmitter design**, which essentially consists in "two planar arrays of printed antennas, where the elements are coupled or

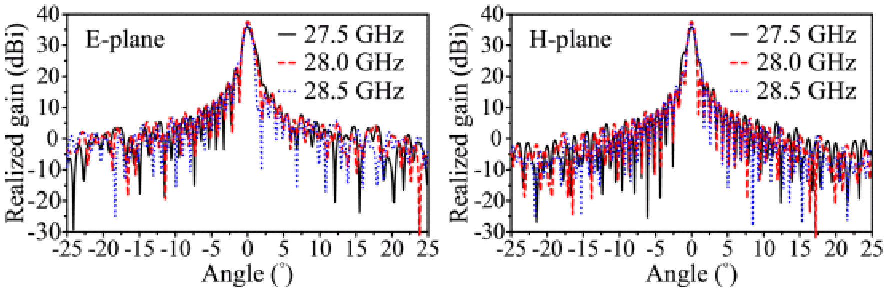

Figure 2.18: (a)E-Plane and (b)H-Plane measured Gain [8]

interconnected by transmission lines"[3]. Is possible to see an example at Figure 2.19

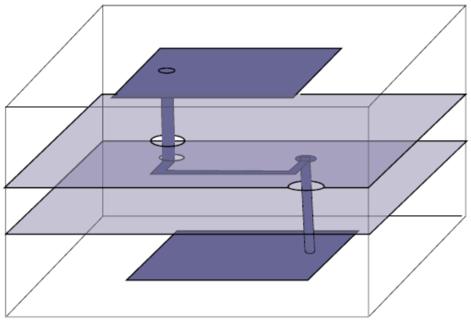

Figure 2.19: Receiver-Transmitter TAs [3]

One of the two arrays will be illuminated by the feed source and therefore, will act as a receiver and the second as a transmitter. The coupling part (transmission line) has a very important task, indeed, since it has to be designed in such a way to achieve a specific phase and magnitude distribution from the first array to the second array [3].
Following this concept in [10] a circularly polarized double-folded TA (DFTA) is proposed and verified. A single difference with respect to what was said before is that the Receiver-Transmitter metasurface (RTMS) is fed with a linearly polarized patch antenna. The measured results exhibits a peak gain of 21.8 dBic at 9.8 GHz and a maximum aperture efficiency of 40 %, while the −1 dB bandwidth is around 6 %.

A very last type of TA which is quickly growing today is the **reconfigurable TA** (RTA). Which is introduced in alternative to the phased array structures, that despite have good radiation performances, are so expensive and complex due to their feeding networks. The RTAs are always made with a Transmitting and a Receiver modules, but now they are spatially fed. This means that two antennas are combined together: one antenna receives the signal and sends it to the transmitter, which radiates into space after the phase is manipulated [11]. The reason why these antennas are growing up is due to the fact that to enhance the antenna performances the pattern needs to be dynamically adjusted and using RTAs instead of the phased arrays, means that instead to adjust the pattern by the feeding network, it will be done by changing the characteristics of the incident EM waves to perform beam steering, beam focusing, and polarization control [12].
Some important examples of these antennas can be found in literature; as for example in [13], where a 1-bit reconfigurable transmitarray antenna (RTA) based

on a Yagi-Vivaldi UC for wideband and beam scanning application at the Ku-band is presented. For the UC the receiving element is made by a tightly coupled microstrip Yagi antenna and a Vivaldi antenna as transmitter. The RTA prototype designed consists in a 16x16 UCs, giving a measured $-1\,\mathrm{dB}$ bandwidth of $14\,\%$ with a maximum gain of $22.3\,\mathrm{dB}$ at $13.6\,\mathrm{GHz}$, corresponding to an aperture efficiency of $25.6\,\%$.

2.2 Smart Electromagnetic Skins (SES) Introduction

The fifth and beyond generation of communication networks will work at higher frequencies than the previous one (mm-waves or sub-THz bands), since they are asked to provide several improvements as very high bandwidth and very high speed in terms of data rate. On the other side, their use has some drawbacks as the high free-space loss and high penetration loss.
A possible solution to this problem should be the increasing of base stations, but on the other hand it will increase the network complexity. Therefore a better solution consists in create the already mentioned Smart Electromagnetic Environment (SEE) [14].

The SEE definition overcomes the previous view of the environment in the wireless scenario, that was considered fundamental but uncontrollable [15]. Indeed now, the environment is used as a resource in which an incoming signal can propagate through it with for example, reflections through buildings. In this view the environment represents a "main character" on the propagation and no more just an obstacle.

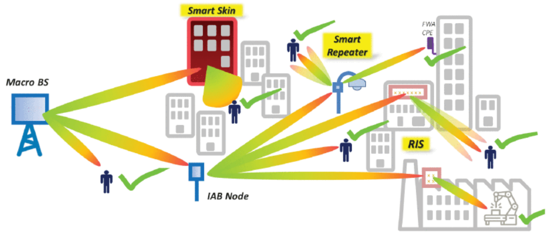

Figure 2.20: SEE actors [16]

One of the devices that could be involved to create this as depicted in Figure 2.20, is indeed the SES. The SES is a quasi-periodic surface since it is made by a number of cells designed to manipulate an incoming beam, in such a way to cover areas that would be inaccessible without other base stations. Then, since they're usually passive structures, this means that they do not need any power supply and this makes them very low-cost and low-complex devices. However, sometimes there is the need to control the output beam in real time and this can be done by a more complex device, that is the Reconfigurable Intelligent Surface (RIS), realized with unit cells that should be dynamically adjusted [17]. From an installation point of view, they could be integrated in walls, building facades, ceilings, or even hung on lamp posts, poles or towers [16].

Now, at the beginning these innovative surfaces were used to cover blind spots working in reflection mode. But nowadays, also the SES working in transmitting mode starts to be explored, and an example is for the Outdoor to Indoor (O2I) applications, where an incoming beam is focused inside a building. The SES that works in transmitting mode is something very similar to a TA except for the fact that the transmitting surface is generally in the far field region of the BS, and therefore the incident field can be modeled with a plane wave.

2.2.1 SES state of art

In the following pages an overview about what is present in literature about Smart Electromagnetic Skins is provided. As already highlighted, at the beginning their application in reflection mode was widely investigated, where they are able to manipulate and redirect an incoming beam with no specular reflections.

In [18] there is a very good example that puts into practice what was previously mentioned about SEE. It consists in a particular way to exploit a building's facade with these passive skins for improving the coverage in urban millimeter-wave communication scenarios. The particularity is found in the total structure, that does not have a conventional shape, due to the fact that the facade is divided into tiles, that essentially represent the minimum building block that composes the entire Electromagnetic skin, and then will be positioned in such a way to have the maximum performance, carried out with a **binary multi-objective optimization method**.
First of all, a single SES is essentially made up by an array of elements (cells) and in this case the cell is very simple, Figure 2.21, that's a metallic patch printed on a single-layer Rogers 3003 dielectric substrate with thickness 0.508 mm

It was simulated on HFSS [20] in a structure made by several of these cells designed to reflect the output beam at $\theta_r = 40°$ and $\phi_r = -20°$ (Figure:2.22).

Now, in Figures 2.23 and in Figure 2.24 is reported the application scenario and the optimized implementation of the skin in the building's facade and its spatial power distribution.

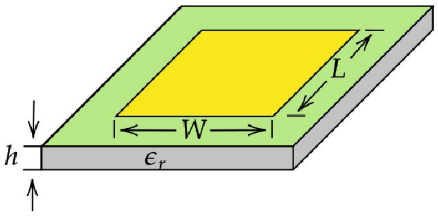

Figure 2.21: Patch cell [19]

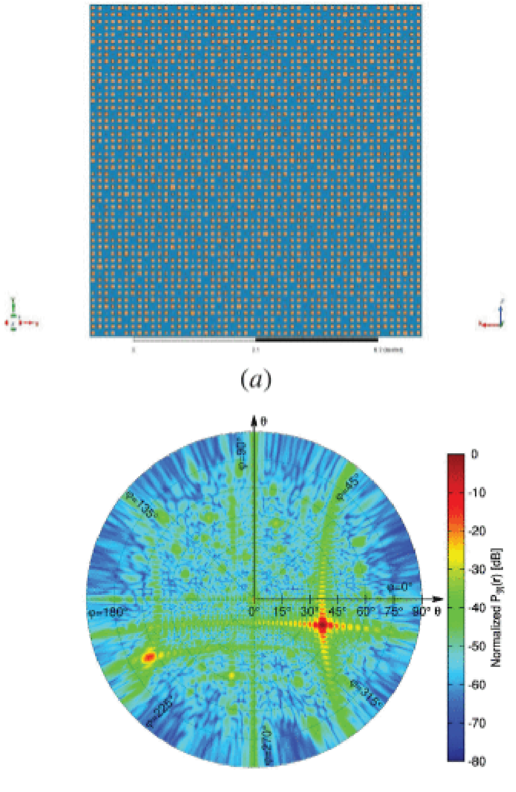

(a)

(b)

Figure 2.22: (a) ANSYS HFSS model of the single-tile EMS (b) angular distribution of the power reflected from the EMS on a sphere at a distance of 5 [m] and computed with (b) ANSYS HFSS [18]

Another interesting urban application, again that works in reflection mode is reported in [14], which investigates the potential of integrating a smart electromagnetic skin into street lights or traffic light poles, but now, instead of using a planar SES, with a curved one, in such a way to be better integrated into the pole due to its cylindrical shape.

As before, the cell used is a square metallic patch as that in Figure 2.21 designed with 5.45 mm x 5.45 mm (that is equal to $\lambda_0/2$ (at $f_0 = 27.5$ GHz that is within the Italian band of 5G defined from 26.5 GHz to 27.5 GHz) printed on a grounded

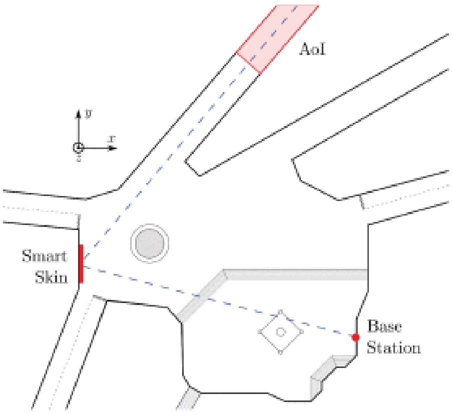

Figure 2.23: Application Scenario [19]

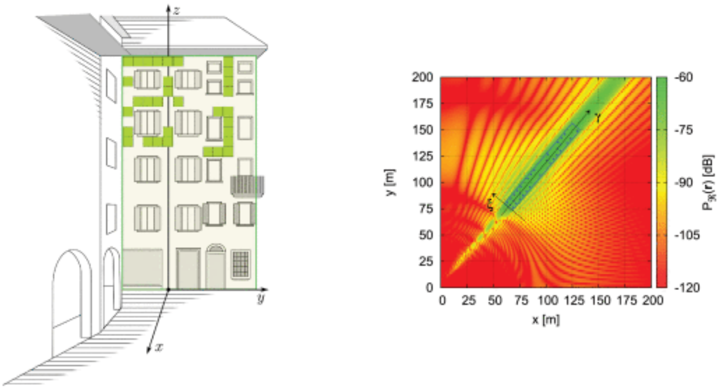

(a) (b)

Figure 2.24: (a) Layout of the Electromagnetic Skin, (b) Spatial distribution of reflected power [19]

dielectric DiClad527 ($\epsilon_r = 2.55$ and $tan(\delta) = 0.0022$) and in Figure 2.25 there is its behaviour in terms of reflection coefficient amplitude and phase:

The SES is designed with 55x62 cells with an incoming plane wave at angles of $\theta_i = 10°$ and $\phi_i = -90°$ and designed to redirect the beam at $\theta_o = 30°$ and $\phi_o = 70°$.

And at the end (Figure: 2.27) could be interesting to see the behaviour of the Radar Cross Section at 27 GHz that confirms the better behaviour of the curved SES with respect to the planar one.

The work presented in [21] focuses on a SES implementation that is designed with cost-effective materials. The approach adopted for the design is based on the use of Non-Radiating (NR) sources, i.e. current distributions belonging to the null-space of the radiation operator and in wireless communications are exploited as additional Degrees of Freedom (DoF) for the SES design. This DoF is employed

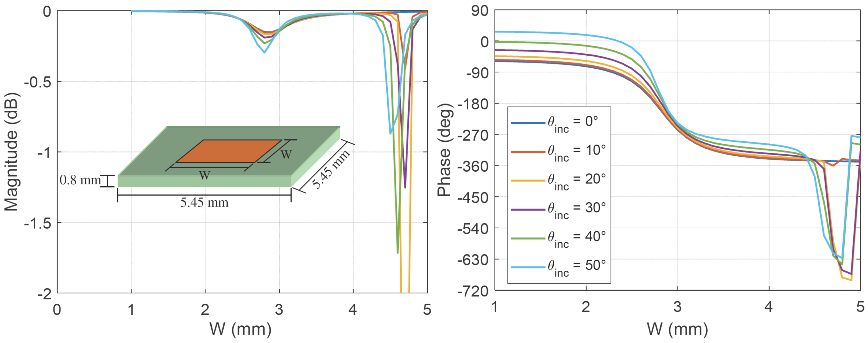

(a) **(b)**

Figure 2.25: S_{11} Amplitude and phase [14]

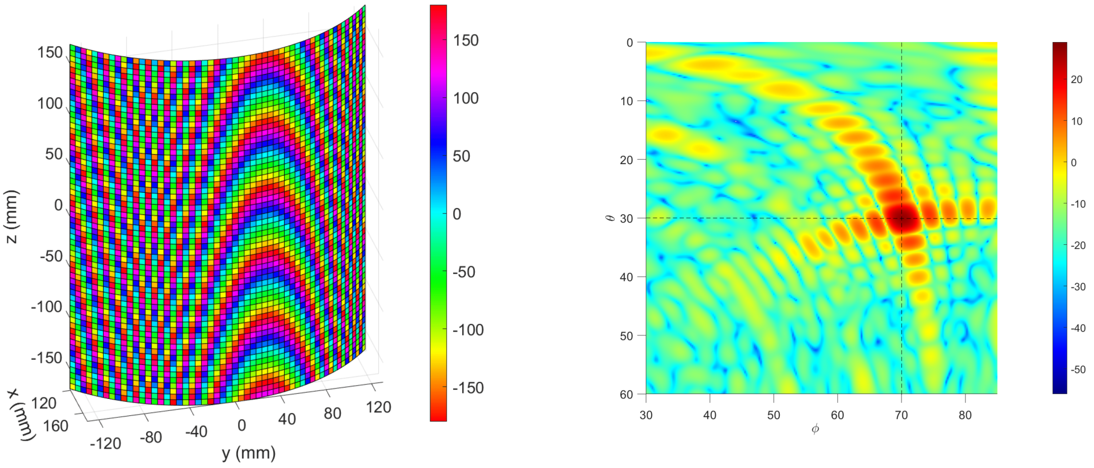

Figure 2.26: (a) Phase map (b) 2D-view of the Radar Cross Section of the designed SES at 27 GHz [14]

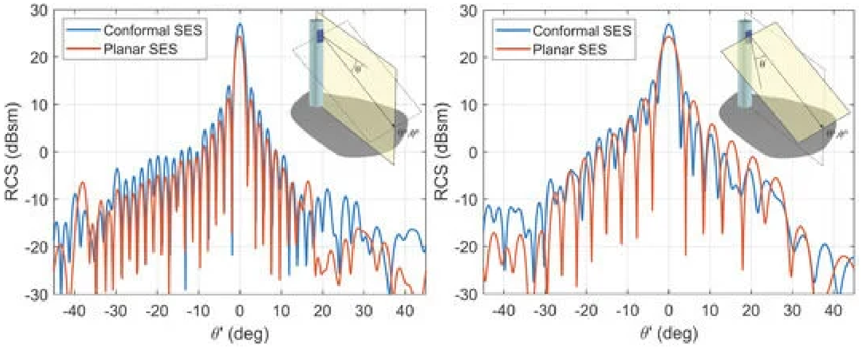

Figure 2.27: RCS for (a) vertical plane (b) horizontal plane

by simply adding a term in the desired SES source distribution as follows:

$$I_{des} = I + I_{NR} \tag{2.1}$$

where I_{des} is the current distribution that provides the desired pattern and I is a term related to the SES pattern and the **Green's Operator (G)**:

$$E = GI \tag{2.2}$$

Now, in figure 2.28 there is reported the radiation pattern for a 55x55 cell structure at $f = 5.5\,\text{GHz}$ based on a square metallic cell printed on a FR-4 substrate, where an incoming plane wave with normal incidence is reflected at $(\theta_r, \phi_r) = (30°, -45°)$. What is immediately possible to see looking at the radiated field is that the NR approach gives an $8\,\%$ less error with respect to the case in which NR is not present.

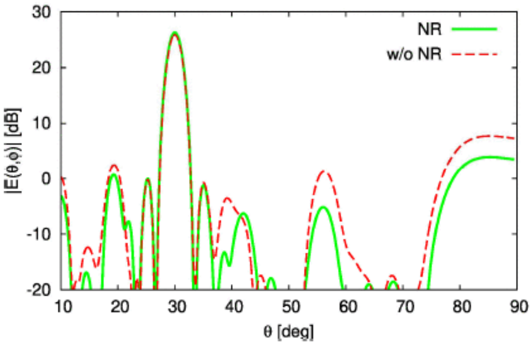

Figure 2.28: Radiation pattern with and without NR term [21]

In [22] it is reported an example in which the scenario is similar to that of interest, but the SES developed works in reflection mode again. The article deals with the problem of integrating a very small surface, made up with just 20x20 UCs into a building facade, but now at centre aperture some cells are missing due to the presence of a window, therefore the window here represents an obstacle. The structure is designed at $f = 3.5\,\text{GHz}$ and to redirect an incoming beam from a base station from $(\theta_i, \phi_i) = (0°, 0°)$ to $(\theta_r, \phi_r) = (30°, -20°)$ and the design is carried starting from the **current density distribution** needed by each structure element. At the end the u-v plot of the radiation pattern is given at Figure 2.29.

These are the simplest types of SESs, where they're just able to redirect an incoming beam in a direction of interest and not specular reflections. However, many times there is a need to change the direction or the shape of the beam without changing the entire structure. This can be done with the Reconfigurable Intelligent Surfaces, where as the name suggests, the surface employed now can be reconfigurable to meet the desired beam specifications, just by adding some elements in the structure that can be reconfigured. In [23], a Reconfigurable Passive Electromagnetic Skin is considered (RP-EMS) and different structures are

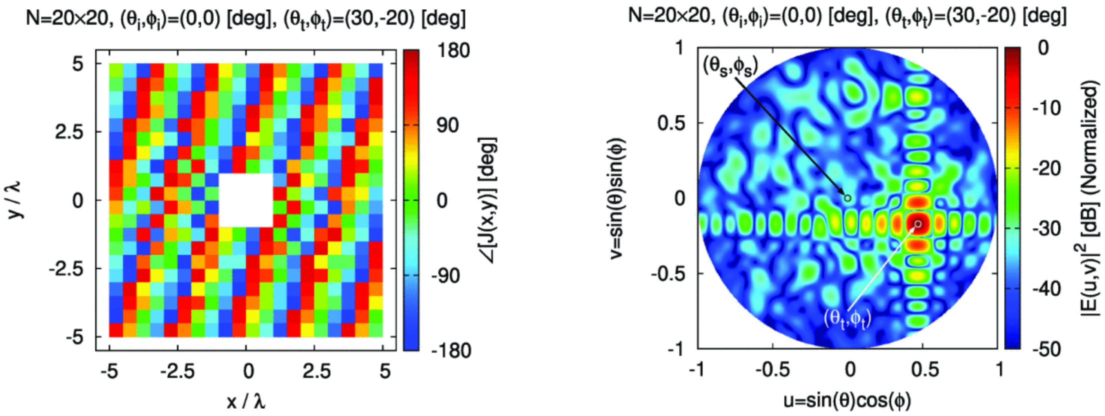

Figure 2.29: (a) Current Density map (b) u-v plot of the radiation pattern [22]

implemented to address the challenge of adapting the coverage area dynamically as the user distribution or environment changes, that's is crucial for maintaining optimal network performance. The reconfigurable element present in the UC part of the structure should be a varactor with $V = 2^B$ different capacitance values, where B is the number of bits supported the varactor as shown in Figure: 2.30.

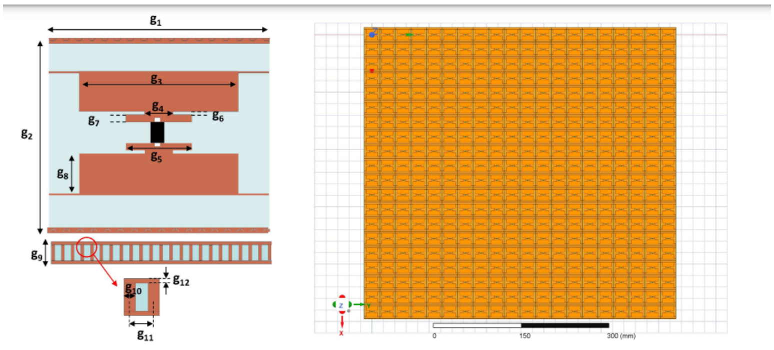

(a) (b)

Figure 2.30: RP Meta-Atom and Skin Layouts - Sketch of (a) the UC geometry and (b) a finite RP-EMS consisting of U = 20 × 20 meta-atoms [23]

Then, is very interesting to see what happens for different numbers of bits used and structure dimensions, shown in Figure: 2.31

Is possible to see that passing from B=1 to 4 it allows a finer beam control, while instead the power efficiency is increased when the dimensions are increased. The paper also exploits the possibility to adjust the beam shape and intensity by reconfiguring the varactor in terms of capacitance values, for example passing from a square footprint to Olympic flag.

As previously mentioned, SES can also be adopted for working in TX mode. In

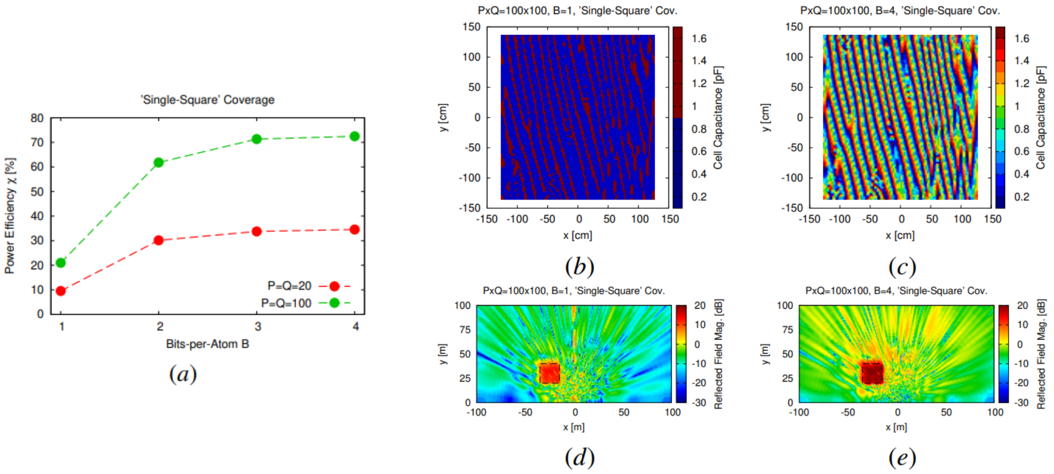

Figure 2.31: (a) Power efficiency (b) Cell capacitance map with B=1 (c) Cell capacitance map with B=4 (d) Square footprint for B=1 (e) Square footprint for B=4 [23]

[24] an application of Reconfigurable Electromagnetic Skin that works in transmitting mode is explored (T-RIS). It is based on a structure made up with some p-i-n diodes to reconfigure the structure, a 90° phase shifter and biasing circuits and the UC view is proposed in Figure:2.32(a):

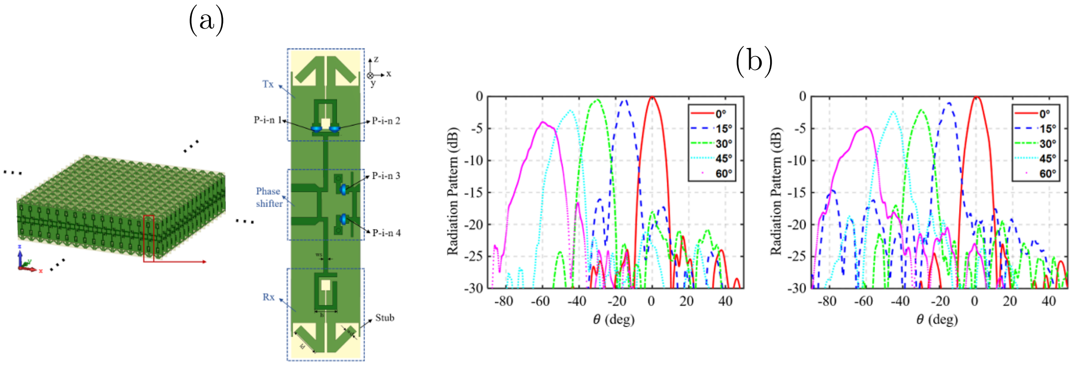

Figure 2.32: (a)UC of T-RIS, (b) Radiation patterns in E-Plane and H-Plane [24]

Then, based on the proposed structure a 16x16 RIS prototype is composed with 16 × 16 elements, fabricated, and measured to experimentally validate the performance of the proposed RIS element and the results are again depicted in Figure: 2.32(b).

The latest researches are keeping in considerations also the usage of RIS works both in transmission and in reflection mode at the same time, especially in communication systems of sixth-generation (6G), allowing in this way to cover larger areas that represent maybe the best benefit introduced by these devices. However, designing these may be a very hard challenge, because until this moment all the introduced SES were designed by controlling just one between Reflection coefficient or transmission coefficient respect to their employment in TX or RX mode, instead, now, both of these two parameters have to be properly controlled. In [25], a general overview to facilitate the design and implementation of these type of RIS in 6G scenarios and network topologies is presented. First of all, the operating protocols for different communication modes are introduced followed by the design concepts, research challenges, potential solutions, and future directions.

2.3 Optically Transparent SES

Once that SES and the purpose for which they're used in this work are introduced, it is necessary to go more in depth and see what is present in literature about OT-SES. However, considering that transmitting SES become object of consideration in the very last research, their integration in building's facades represents a new topic. Starting from this, here can be found all the best structures and their simulated results that could be directly mounted into a window, also analyzing the design procedure that is very similar to that of Transmitarray Antennas, apart from the type of incoming field. As previously introduced, the window now will be part of the structure itself, indeed every unit cell will be composed of a glass sheet and a dielectric OT material that in the most of cases is a plastic.

2.3.1 OT SES State of Art

OT SES are a matter of research that is easily growing in order to increase their integration and since represent a very recent innovation, it can be quite difficult to find many information in literature. Now, apart from the EM surfaces, in literature the first approach to optically transparent surfaces and their integration in windows belong to another type of electromagnetic surfaces, know as Frequency Selective Surfaces (FSS).

The FSS is an electromagnetic surface that is very similar to that object of this work. According to [26], an FSS is "a periodic surface made up of two-dimensional arrays of identical elements arranged on a dielectric substrate", which serves as an electromagnetic filter. This allows the transmission (or reflection) of a signal within a specific frequency range while blocking all others. In [27] a FSS is implemented to reduce the attenuation introduced by a low-emissivity (low-e) energy-efficient glass, which is a double glass used to achieve thermal insulation and reduce energy consumption. The FSS here is inserted within the 2 glass sheets of 6 mm which are filled with an air gap of 12 mm, while the UC shape is represented in Figure 2.33. In the same Figure is reported also the aim of the paper, where the simulated and measured structure with FSS and the single glass transmission module are plotted, so it is possible to see that with just the full-coated low-e glass the signal is attenuated by 25 dB to 30 dB in the frequency range that goes from 1 GHz to 5 GHz.

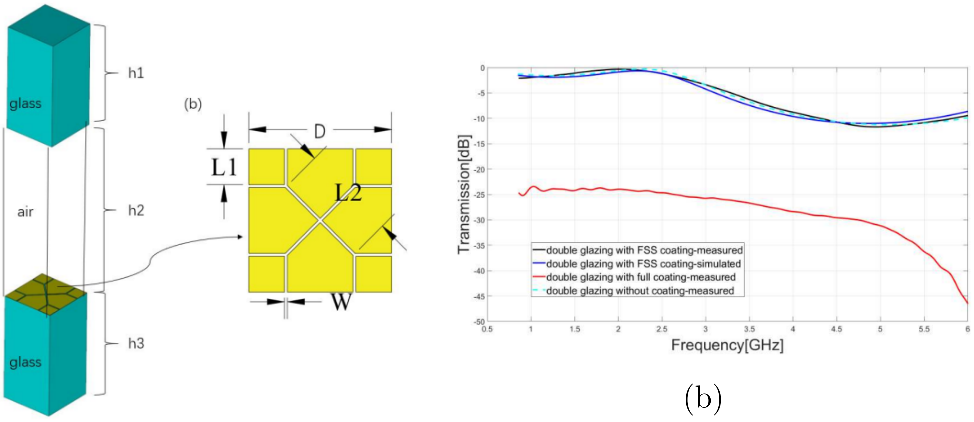

(b)

(a)

Figure 2.33: (a)UC structure (b) S_{21} module [27]

Then, despite FSS being low-cost devices characterized by a simple design procedure, their performance strongly depends on the polarization and incident angles of the EM wave due to the large size of the resonant elements, therefore, polarization- and incident-angle-insensitive FSSs are fastly growing in recent reasearches. Another problem related to the FSS is due to their structure, since the single layer FSS has not the best performances in terms of transmission coefficient amplitude and phase and for this reason, a multi-layer approach is necessary to enhance their performance, or another solution could be recurring in **metasurfaces**.

Metasurfaces are electromagnetic surfaces realized with artificial material made again by cells, who generates a periodic structure. These devices provide numerous advantages for this application. They allow the placement of unit cells within a limited space and offer a more stable frequency response across different angles of incidence. Additionally, they are highly efficient for transmission through surfaces with small openings, such as windows, in this way the 5G coverage indoors is enhanced [28]. In the same paper there's another example that could be of interest, where could be found two transmissive metasurfaces coated on a glassy window to enhance the 5G outdoor to indoor (O2I) coverage inside vehicles and buildings.

The analysis refers to cases of just a single glass and double glass where an Indium Thin Oxide (ITO) film metasurface is integrated, therefore, with the metallization presence. The UC design is carried with a Boroflat glass of 1.1 mm at the top, followed by a ITO square and again a boroflat sheet and an ITO film that are all mounted on a single glass. So, the aim of this work is to analyze the transmission enhancement with the metasurface's UC with respect to the single glass sheet and can be appreciated at Figure 2.34 from which is possible to conclude that the proposed metasurface improves signal strength through a single glazed glass for incidence angles ranging from 0° to 75°.

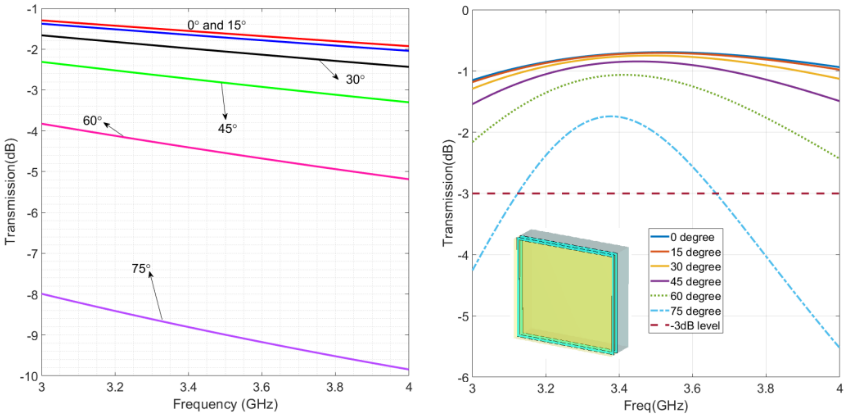

Figure 2.34: Transmission coefficient of single glass (left) and of metasurface's UC (right) [28]

But exploring now some more similar examples to the work aim, a good starting point could be what is done in [29], where Optically-transparent opportunistic electromagnetic skins (OTO-EMSs) are proposed to create Outdoor-to-Indoor (O2I) link, exploiting millimeter-wave (mmW) wireless communications and considering also the windows.

According to the authors, the "OTO-EMS is a static passive Electromagnetic Skin that consists of one or more conducting, but optically-transparent, patterned layers which are attached using an optical clear adhesive to a glass window", so the aim is to establish an Outdoor to Indoor (O2I) link without any visual impact. Now, the UC shape is made with meta-atoms realized with copper mesh mounted on an insulating glass, which is a type of glass made from two sheets separated by a space, usually filled with air, that is usually filled with air, to significantly reduce heat transfer from the exterior to the interior of the building. The shape of the unit cell can be seen in Figure 2.35. Then, the geometric features of the

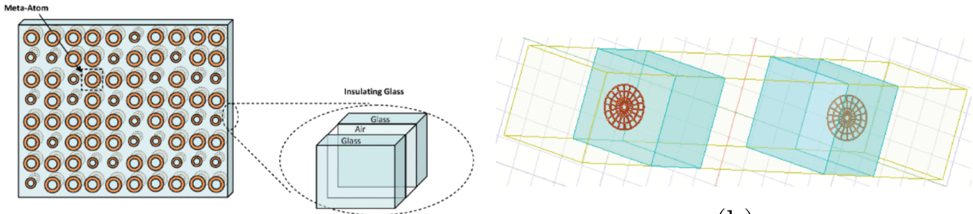

(a) (b)

Figure 2.35: (a)Structure and (b) Unit Cell shape [29]

UC are the following: the glass is 4 - 10 - 4 Insulating glass type, that means is made with two glass sheets of thickness 4 mm, relative permittivity $\epsilon_r = 5.5$ and loss tangent $tan\delta = 3.0 \cdot 10^{-2}$, which are separated by an air-filled space of 10 mm thick, so that the total thickness is 18 mm. The metalizations which composes the meta-atom, as already mentioned, are made with copper characterized by conductivity $\sigma = 5.8 \cdot 10^7 [S/m]$ and thickness $30 \cdot 10^{-6} [m]$, while the meta-atom lattice periodicity has been set to $\Delta = 3.7$ mm. Finally, the entire 30x30 structure could be simulated at $f = 26$ GHz and the transmitted pattern $|E_\phi^{trans}(r)|^2$ vs the angle θ could be plotted at Figure 2.36, which reports the case where the output beam is in broadside direction (that's normal to the structure and is equivalent to a reflection angle $\theta^{rx} = 180°$). On the same plot can be found information also when the output beam is 20° shifted and the contribute of the Insulating Glass of the same dimension of the EMS structure (blue line) with an empty region always of the same dimension.

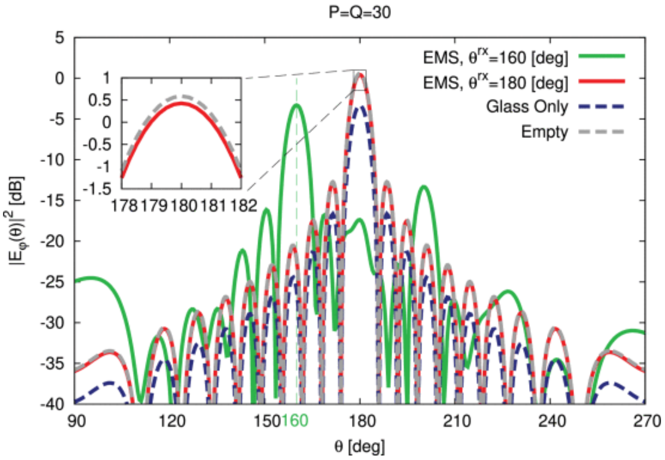

Figure 2.36: Plots of the transmitted pattern [29]

At the end, could be interesting to extend the analysis of the performance degradation versus the scan angle, reported at Figure 2.37, which allows to understand that the focusing capabilities of the structure are well despite the limited phase range of the UC (around 220°). Following the same idea but in a different application, in [30] an EM surface is implemented for an O2I application embedded into a laminated car glass at 38.5 GHz that is the frequency manifesting the highest penetration loss for 5G.

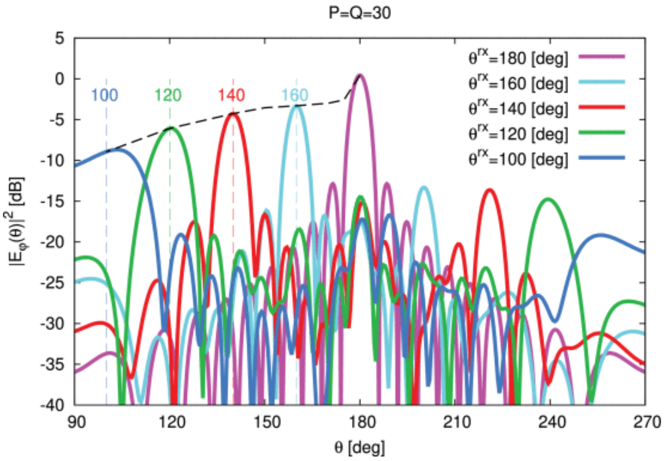

Figure 2.37: Plots of the transmitted pattern vs different scan angles [29]

Consider that the conventional laminated car glass is made of two pieces of glass of 2.1 mm each with a PVB film between the two sheets, used to prevent the glass breaking. As in the previous example, metallization will be present, which will have the Jerusalem cross pattern shape of 1 µm thickness made of silver, instead of the commonly used ITO film, since it exhibits higher durability. Another reason why the Jerusalem cross pattern is used is due to the ensured transparency, for the fact that thanks its shape, this cross will occupy only the 10 % of the UC area. Now, apart for the metallization, the UC will also introduce an optically transparent plastic film within the PVB sheet in such a way as to provide a wide range of phase shifts by spacing the two metal layers. In the end, the UC will be characterized as reported in Figure 2.38,where it is also possible to see the transmission coefficient module and phase related to 7 different UCs implemented just by changing the geometrical dimensions of the Jerusalem cross and is possible to see by the plots that at the frequency of interest the insertion loss is minimized and the phase variation is about 123°.

Now, the structure will be 20 cm x 20 cm and will be attached to the passenger's window and is designed to take the incoming plane wave and focus it at a distance of 30 cm, which is approximately the distance in which is located the intended user. To be precise, the paper discusses about the implementation of a

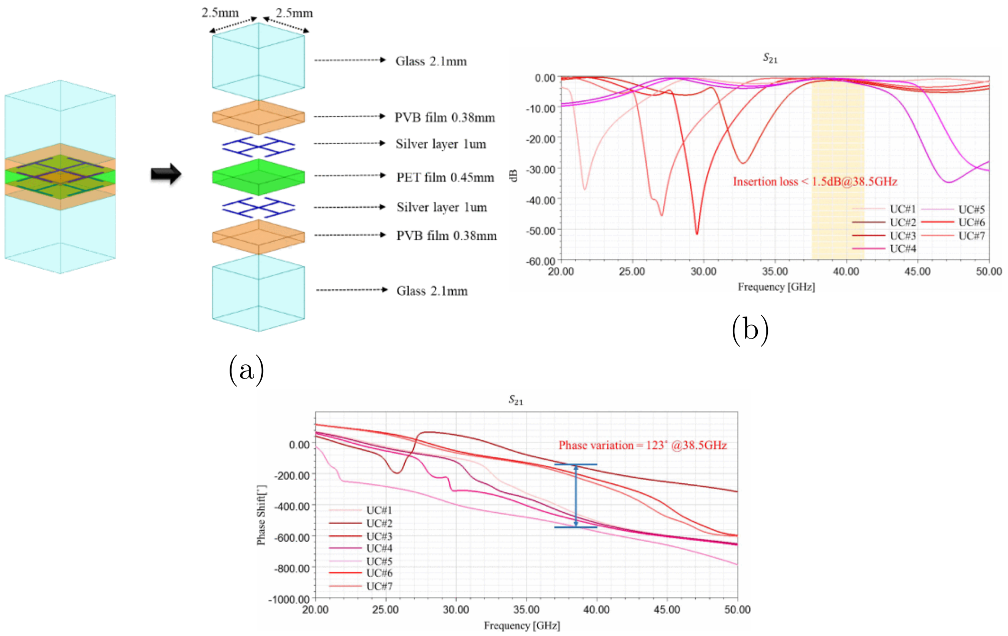

(a)

(b)

(c)

Figure 2.38: (a)UC structure, (b) S_{21} module vs frequency, (c)S_{21} phase vs frequency [30]

Transmitarray antenna, but the horn is located at 2 m and the field that arrives at the structure could be approximated as a plane wave and for this reason it is very similar to the SES. Both measured and simulated results aim to show the increased field intensity obtained with the structure embedded in the glass compared to conventional glass. This results from both simulated results and measured one that the field exhibit an increasing in its intensity around 5 dB. Specifically, an RX antenna is positioned in 27 different points in the passenger's seat and the best results provide a measured field that passes from −45 dB of the conventional window to −40.45 dB with the structure inserted in the glass, providing a 4.55 dB increasing in field intensity.

2.4 Design and Analysis of Planar Surfaces

As introduced before, TA is made by two essential parts and the design procedure will focus on the transmitting part design, that has the task of transforming the impinging field generated by the feed, from spherical wavefront to planar wavefront, that is the key-feature which stands at the bases of lens antennas. Since the transmitting part is composed of several unit cells that will be affected by a phase shift, it highlights the analogy with the planar phased array antennas.

There are essentially 3 steps from which is possible to characterize the TA transmitting part belonging to the multi-layer approach design. The other design techniques are one based on the receiver-transmitter design (mentioned in the Paragraph 2.1.1) and one based on metamaterials, where the idea consists in varying the effective substrate permittivity and permeability using 3D structure made of two or more materials.

1. **UC analysis**;
2. **Phase distribution evaluation**;
3. **Total structure definition**;

The first step is made considering that UC is a part of a **periodic structure**. The approach consists of taking an element and allowing a **geometric parameter**, part of the element itself, to vary in such a way as to analyze its behaviour in terms of transmission coefficient amplitude and phase. In the Figure 2.39 there is a very simple UC example,that represents a simple block of a material with an ϵ_r of 2.7 and a $\tan(\delta)$ of 0.01, where p is fixed to 5.55 mm and it is also known as **cell periodicity**. The periodicity dimension is fixed to a sub-wavelength or resonant-wavelength, in fact here is equal to $\lambda/2$.

An idea should be for example, to let the height of this block to vary from 1 mm to 14 mm and look its S_{21} phase and amplitude behaviour, as reported in Figure 2.40.

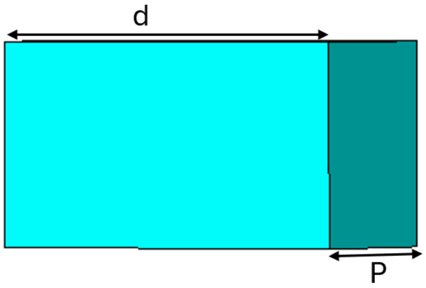

Figure 2.39: UC example

However, looking at this example, one can understand that the UC behaviour for transmission coefficient module and phase is not the best, since it provides a module with an oscillating behaviour, with several negative peaks from −1.1 dB to almost −1.5 dB. This can also be confirmed by the **reflection coefficient** (S_{11}), which is the dual of the transmission coefficient.

As shown in Fig. 2.41, the duality is highlighted by the reversal from negative peaks to positive peaks.

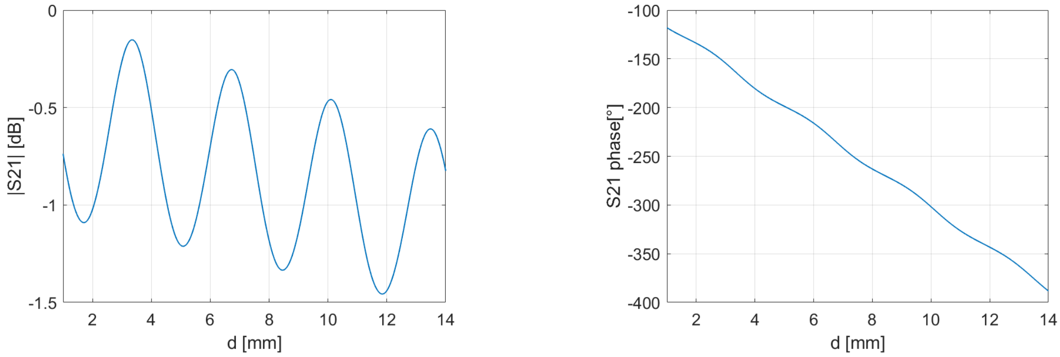

(a) (b)

Figure 2.40: S_{21} module (a) and phase (b)

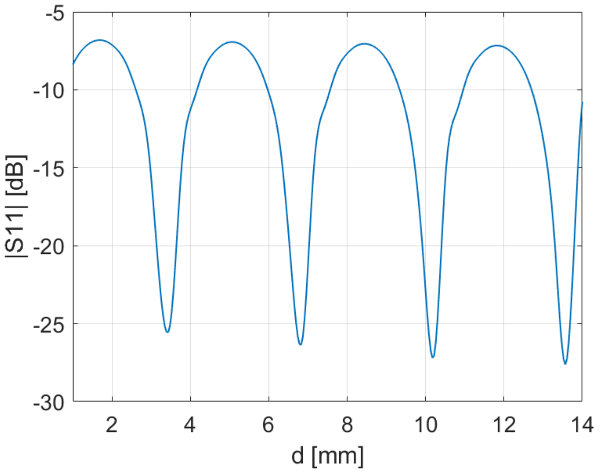

Figure 2.41: S_{11} module

Also the S_{21} phase is not the best, since it covers around 260°, which is far from the 360° required.

Thus, it is possible to conclude that the UC is the very essential first element to be designed because its behaviour will affect that of the whole structure. An UC with a transmission coefficient module so far from the ideal value of 0 dB can increase the reflections from the structure itself. Furthermore, the phase deviation can directly impact on the gain reducing it or in the change of the desired direction.

This is just an example to see how the UC can be designed, but clearly if the performance of the entire structure wants to be improved is necessary to start from the UC. Indeed, many times a proposed solution to increase the performance of the cell and, therefore, the structure, is to use a **multi-layer approach** as previously reported in paragraph 2.1.1. This means that the UC is now made up of several layers, which are usually the same as shown in Figure 2.42.

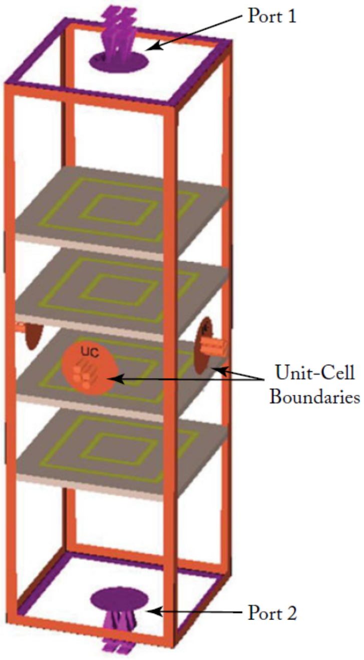

Figure 2.42: Multi-layer UC [3]

In the following, the UC simulation is performed with CST Microwave Studio [31] adding the UC boundary condition, which means the simulation is done assuming that the UC is embedded in a periodic lattice.

After the UC has been designed the next step is to determine the **phase distribution**. Once that the dimension of the entire structure is determined and consequently, the number of elements that composes it, the required phase of each element of the TA has to be evaluated in order to compensate the spatial phase delay from the feed horn to the element itself. In this way, thanks to the phase distribution produced, the TA is able to focus the beam in the wanted direction . In doing this an important approximation is taken, in fact is assumed that the elements are in far-field region. Therefore, the incoming field from the horn is approximated as that of a plane wave [3]. The phase distribution is obtained by the 2.3.

$$\phi_i = k(R_i - \vec{r_i} \cdot r_0) - \phi_0 \tag{2.3}$$

Where:

- **k** represent the propagation constant in free space;
- R_i the distance from the feed source to the single element i;

- $\vec{r_i}$ the distance of the element i from the centre of the antenna;
- r_0 the main beam direction;
- ϕ_0 that represent a constant reference phase;

Quantities that can be appreciated from the illustration at Figure 2.46.

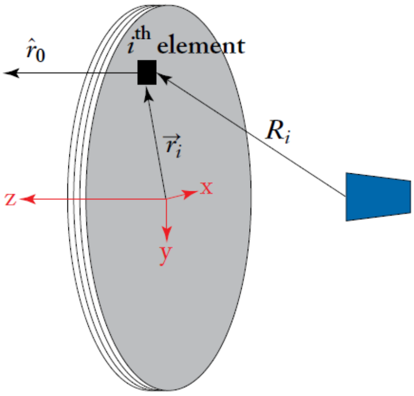

Figure 2.43: Phase distribution scheme [3]

When the centre element is considered, R_i corresponds to the **focal length** (F), which is the distance from the feed to the centre element itself. This is important because usually, these types of antennas are characterized by the parameter F/D, where D is the antenna's diameter. Then, an important simplification of the 2.3 is when the output beam is in the broadside direction, this means that is normal to the structure and more in detail, that r_i and r_0 are perpendicular one to the other and since they're linked by a scalar product, it will give zero.

In Fig. 2.44 it is shown an example for phase map evaluation considering the case in which the field radiated by the feed impinges with angles $(\theta_i, \phi_i) = (0°, 0°)$ on the TA and that this last is designed to focus the main beam in a direction characterized by $(\theta_{max}, \phi_{max}) = (0°, 0°)$.

In this example the planar surface is discretized with 347 element. The periodicity is 16.5 mm and it correspond to a diameter of 34.5 cm. The TA is designed at the frequency of 11.3 GHz and with a F/D=0.8, corresponding to a focal distance of 27.65 cm.

At this point could be worth focusing on the computation of the radiation pattern for the Transmitarray Antenna. Among all the possible solutions, one of them is based on array theory, in which the radiated pattern of a bi-dimensional planar array of MxN elements (unit cells) can be computed by the 2.4 [3].

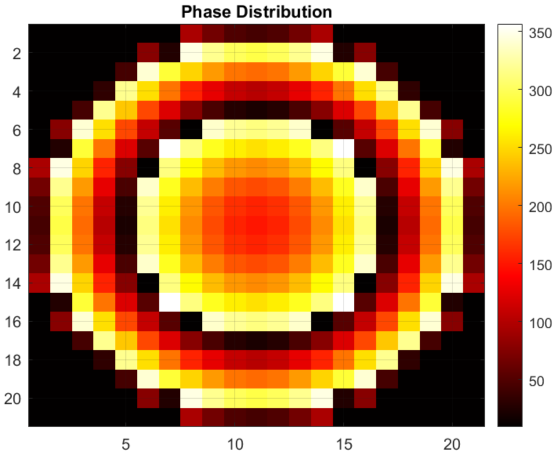

Figure 2.44: Phase Distribution

$$\vec{\mathbf{E}}(\hat{u}) = \sum_{m=1}^{M}\sum_{n=1}^{N} \vec{\mathbf{A}}_{mn}(\hat{u}) \cdot \mathbf{I}(\vec{\mathbf{r}}_{mn}) \tag{2.4}$$

Where $\hat{u}$ is given by the 2.5 and $\vec{A}_{mn}$ represent the element pattern vector function, instead $\vec{I}$ is the element excitation vector function.

$$\hat{u} = \hat{x}\sin\theta\cos\varphi + \hat{y}\sin\theta\sin\varphi + \hat{z}\cos\theta \tag{2.5}$$

Considering that usually the coordinate system is given by that in Figure 2.45, where the origin is located at the centre of the transmitting surface and x and y are located in the surface. The feed is located at height H and has coordinates $(0, -H\tan(\alpha), -H)$ where α is the offset angle.

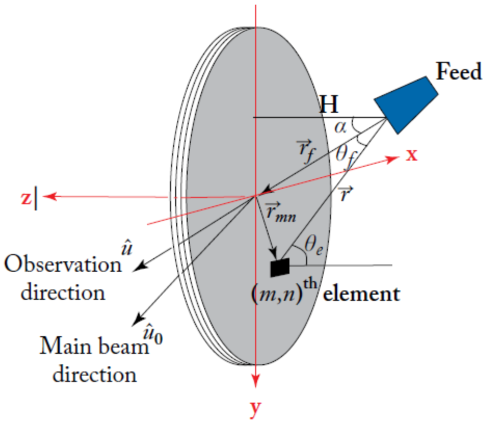

Figure 2.45: General TA coordinate system [3]

Generally, to simplify computations, in the element pattern vector function $\vec{A}_{mn}$ a cosine q model is used and no azimuthal dependency is present.

$$\vec{A}_{mn}(\theta, \varphi) \approx \cos^{q_e}(\theta) e^{jk(\mathbf{\vec{r}_{mn}\hat{u}})} \tag{2.6}$$

$$\vec{I}(m,n) \approx \frac{\cos^{q_f}(\theta_f(m,n))}{|\vec{\mathbf{r}}_{mn} - \vec{\mathbf{r}_f}|} \cdot e^{-jk|\vec{\mathbf{r}}_{mn} - \vec{\mathbf{r}}_f|} \cdot |T_{mn}| e^{j\psi_{mn}} \tag{2.7}$$

In 2.6 q^e represents the element pattern power factor. The element excitation can be implemented as in 2.7, where $\theta_f(m,n)$ is the spherical angle considering the feed's coordinate system, q_f is the feed pattern power factor, since also the feed horn pattern can be approximated with a cosine q model, $\theta_e(m,n)$ is the angle defined by the line that goes from the feed to the mn^{th} element ($|\vec{r}|$) and the normal direction of the aperture plane, $\mathbf{r}_f$ is the vector that expresses the feed position, $|T_{mn}|$ is the transmission magnitude of the mn_{th} element which is obtained directly from the unit-cell analysis, and ψ_{mn} is the required phase delay of the mn_{th} element to direct the main beam in the $\hat{u}_0$ direction.

Considering the periodic boundary conditions for the unit cells, a mutual coupling effect can be considered between the elements according to the infinite array approach. In fact, in this approach each element is considered to be within an infinite array environment, where all the surrounding elements are identical to it. Thanks to this approximation the radiated pattern can be simplified in a scalar form as that in 2.8.

$$\mathbf{E}(\theta, \phi) = \sum_{m=1}^{M} \sum_{n=1}^{N} \cos^{q_e}(\theta) \frac{\cos^{q_f}(\theta_f(m,n))}{|\vec{\mathbf{r}}_{mn} - \vec{\mathbf{r}_f}|} \cdot e^{-jk(|\vec{\mathbf{r}}_{mn} - \vec{\mathbf{r}}_f| - \vec{\mathbf{r}}_{mn} \cdot \hat{u})} \cdot |T_{mn}| e^{j\psi_{mn}} \tag{2.8}$$

Thanks to this equation, it is possible to evaluate the radiation pattern of rectangular aperture transmitarray antenna made by MxN elements. In view of the TAs that will be simulated in Chapter 4, since all have circular aperture, the 2.8 can still be used neglecting the elements located outside the circular aperture (those where $|\vec{r}_{mn}| > R$, where R is the aperture radius).

Another important parameter during the TA analysis is the directivity. According to [3] "The directivity of an antenna is the ratio of the maximum radiation intensity to the average radiation intensity over all directions", expressed in 2.9:

$$D_0 = U_{max}/U_0 \tag{2.9}$$

But if the TA radiation pattern is obtained by the 2.8 it can be rewritten as in 2.10, where θ_0 and ϕ_0 are the direction of the main beam.

$$D_0 = \frac{|E(\theta_0, \phi_0)|^2}{\frac{1}{4\pi}\int_0^{2\pi}\int_0^{\pi}|E(\theta,\phi)|^2 sin(\theta) d\theta d\phi} \tag{2.10}$$

Also the gain has to be defined since it is a key-parameter for the TAs. It was defined at the beginning of this chapter, but now is important to know that is directly linked with the directivity by means of spillover frequency and the average element loss (Eq 2.11):

$$G_0 = D_0 \times \eta_{spill} \times E_{avg} \tag{2.11}$$

In the [3] is provided a definition for the spillover as "part of the power from the feed, which is not intercepted by the antenna aperture", so the spillover efficiency is defined as in 2.12.

$$\eta_{spill} = \frac{\iint_{\sigma} \vec{P}(\vec{r}) \cdot d\vec{S}}{\iint_{\Sigma} \vec{P}(\vec{r}) \cdot d\vec{S}} \tag{2.12}$$

Where the flux integral present at numerator represent the part of the power incident on the array aperture, while at the denominator that radiated by the feed. Instead for what concern the average element loss can be determined only when the transmission magnitude of each element is known (Eq. 2.13).

$$EL_{avg} = \frac{\sum_{i=1}^{T} I_i^2 |T_i^2|}{\sum_{i=1}^{T} I_i^2} \tag{2.13}$$

Where I_i is the illumination magnitude and T_i is the transmission coefficient magnitude.

Starting from the UC behaviour and the phase distribution required for TAs, it is possible to determine the full structure. Once that the phase distribution is determined, is possible to see how the total structure is created. Indeed is necessary to take the required phase for the i-th element according to the phase distribution and check which abscissa value of the UC phase curve corresponds to it. If the abscissa is a geometric parameter such that in Figure 2.39, then this means that the the i-th element needs to be constructed with this parameter value to meet the desired phase.

To better understand the situation, if the centre element of a phase distribution requires a phase of 160° and the UC desired to construct the TA is that in Figure 2.39, there is a match with the curve (b) in 2.40 at $d \approx 5\,\mathrm{mm}$ (160° for these problem purposes is equal that consider 160°-360°=-200°).

The problem now is that the match between values does not always occur. In particular, for UCs as that in Figure 2.39 where the phase curve doesn't cover 360°, but only 260°, this missing match will introduce **phase error** and its consequences were already briefly explained. When the phase distribution for the i-th element require a value out from the curve, it will be approximated with the closest value, that usually corresponds to the first or last value. Considering again, for example, the curve of Figure 2.40 and a required phase value of 250° it will not find any match with the curve and its values ±360° and it will be approximated with the first value of the phase curve since it is the closest one, introducing a phase error of 10°.

Another type of phase error with lower intensity is due to the curve resolution. Since the curve is made by several points, is very unlikely that the phase required matches perfectly with a curve value. Therefore, the higher the number of points used to represent the curve the lower will be this other phase error.

Once all the evaluation for the entire structure are done this can be created. An example for a TA is reported in the Figure 2.46.

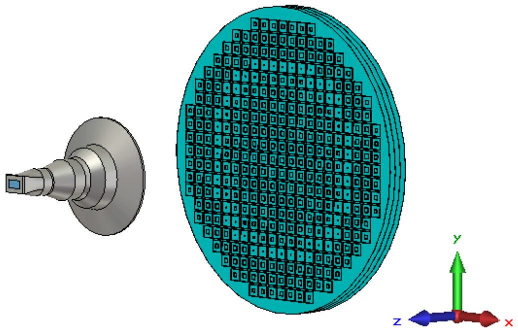

Figure 2.46: Full TA example

This is referred to a double square loop UC designed with the multi-layer approach where clearly, since the transmissions has to be maximized, the distance to the layers has to be as close as possible to a quarter of wavelength. Once, the structure was designed, it must be fed with an horn in this case that is at $F/D = 0.9$, therefore at a distance of 0.9 the TA diameter.

Since as already mentioned, the SES derives from Transmitarray antenna, it can be imagined that also the design procedure that stand at the basis of SES is almost equal to that of TAs. For TAs the planar lens is generally located at a distance equal to the focal length from the feed, comparable to the size of planar surface itself as shown in Figure 2.47. On the contrary, SESs are supposed to be located on far field region with respect to the BS, and therefore the incident field can be approximated as a plane wave.

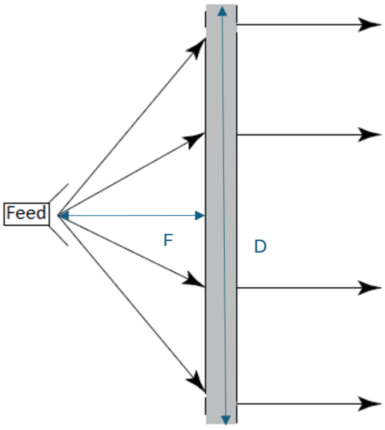

Figure 2.47: Focal length to Diameter [3]

Therefore, could be of interest looking how an incoming field should be approximated as plane wave. The [32] examines the field of an extended source in the far-field illumination region with a particular attention about the conditions under which an extended source field can be approximated by a spherical wave or a plane wave, where doing this last is the actual interest.

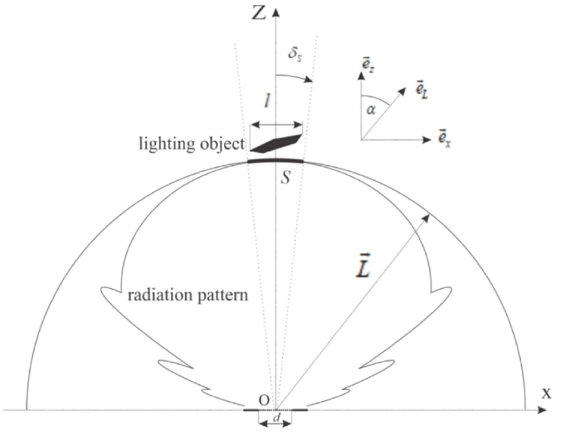

Figure 2.48: Radiation pattern example [32]

At the beginning, the conditions for which the far-field region can be considered are explained and are [32]:

$$x_p << L \tag{2.14}$$

$$x_p^2/\lambda L << 1 \tag{2.15}$$

That, by looking at Figure 2.48, is possible to identify the quantities under investigation, where:

- x_p is the abscissa value in the x-z plane for the radiation pattern.
- L is the radius of the half circle in which the radiation pattern is inscribed.
- λ the wavelength.

Then, by looking again at Figure: 2.48, there is a portion of the half-circle in which the radiation pattern is inscribed, identified with l, where the field of the source at O is *flat* (Figure:2.49). This will happen for an angle θ [32]:

$$\theta = \lambda/L \tag{2.16}$$

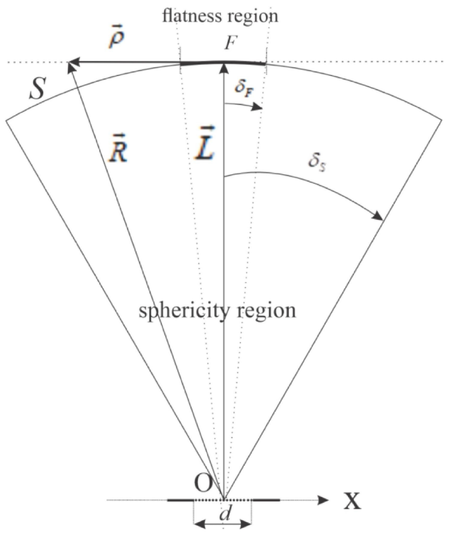

Figure 2.49: Flatness Region [32]

In this flatness region there is the possibility to approximate the sphere wave to a plane wave if the following sufficient conditions are satisfied [32]:

$$\rho^2 << L^2 \tag{2.17}$$

$$\rho^2 << \lambda L \tag{2.18}$$

Starting from the consideration that the phase distribution on a TA to produce a beam in the desired scatter direction from array theory is given by [33]:

$$\phi(x_i, y_i) = -k_0 \cdot (sin(\theta_b)cos(\phi_b)x_i + sin(\theta_b)sin(\phi_b)y_i) \tag{2.19}$$

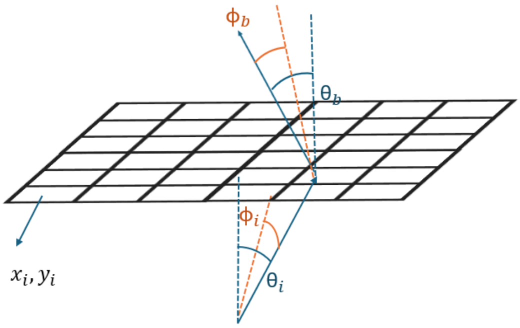

Figure 2.50: Transmitting part of TA

where: k_0 is the propagation constant in the free space at the frequency f_0, xi, yi represents the coordinate centre of the array elements and (θ_b, ϕ_b) the desired angle in which the beam has to be focused.

Now, is important to know that the phase of the transmitted field is give by the sum of the phase of the incident field plus the phase shift introduced by the elements itself:

$$\phi(x_i, y_i) = -k_0 d_i + \phi_r(x_i, y_i) \tag{2.20}$$

And $\phi_r(x_i, y_i)$ represent the phase of the transmission coefficient introduced by the element located at x_i, y_i, while d_i is the distance of the array from the source. But, since an incoming plane wave has to be considered, this distance is approximately infinite and therefore, a good approximation is:

$$k_0 d_i = k_0(x_i sin(\theta_i)cos(\phi_i) + y_i sin(\theta_i)cos(\phi_i)) \tag{2.21}$$

Where now (θ_i, ϕ_i) represent the angle of incidence of the incoming plane wave. So is finally possible to determine the phase required by each element in case of plane wave illumination:

$$\phi_r(x_i, y_i) = -k_0[x_i(sin(\theta_i)cos(\phi_i)+sin(\theta_b)cos(\phi_b))+y_i(sin(\theta_i)cos(\phi_i)+sin(\theta_b)sin(\phi_b))] \tag{2.22}$$

Once this is implemented the result consists in a phase map that is equal to that of TAs. Therefore, just to summarize, the design of the UC is the same as that of a TA, the determination of the phase map is different because has to consider the incoming plane wave and at the end the structure can be obtained in the same way as before.

Once the SES design procedure is explained a mathematical expression about the transmitted electromagnetic field can be introduced. A well-explained formulation is proposed at [29] where the transmitted electric field of an Electromagnetic skin operating in transmitting mode is considered to be illuminated by an outdoor source. The case of study is very similar to that proposed in this thesis, indeed the outdoor source is a time-harmonic electromagnetic field modelled as a plane wave that will impinge on an EM skin, with a surface Ω, integrated on a window. The plane wave E^{inc} is composed by a wave vector k^{inc} and has an incidence described by the angles $(\theta_{inc}, \phi_{inc})$, while the transmitted component E^{tran} is defined through the EM skin in a point r expressed by the coordinates x, y, z and depends on the geometrical descriptor of the EM skin D (Eq. 2.23).

$$D \equiv (d_{pq}; p = 1...P; q = 1......Q) \tag{2.23}$$

In d_{pq} are contained the features of the unit cells, while p and q are the identifier of the considered UC.

The optimum descriptor D (D^{opt}) can be seen as that which minimize $\Phi[E^{tran}(r; D)]$, therefore that which minimize the function that contain the radiation objectives defined or the total transmitted pattern.

For what concerns the transmitted field a reliable expression has to be found, and in [29] it is provided and is based on the Love's equivalence principle and the homogenization of the surface current [34]. In particular, the field transmitted through the EM skin in far field region is computed as in Eq. 2.24.

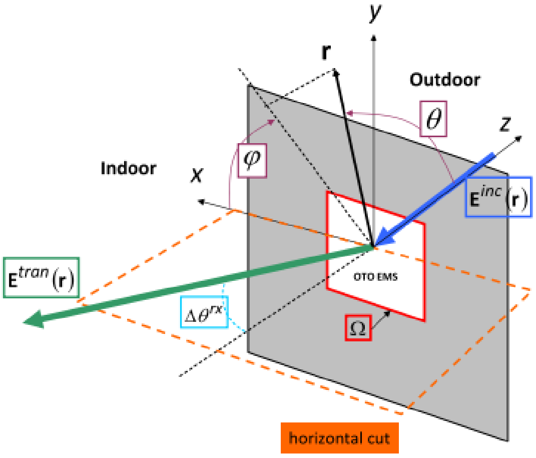

Figure 2.51: Graphical representation of quantities used for transmitting EM skin mathematical formulation

$$
\begin{aligned}
E^{tran}(r; D) \approx & \frac{jk_o \exp\left(-jk_0|r|\right)}{4\pi|r|} \\
& \times \sum_{p=1}^{P}\sum_{q=1}^{Q} \widehat{\mathbf{r}}' \times \left[\eta_0 \widehat{\mathbf{r}}' \times \mathbf{J}^e_{pq}\left(\underline{d}_{pq}\right) + \mathbf{J}^m_{pq}\left(\underline{d}_{pq}\right)\right] \\
& \times \int_{\Omega_{pq}} \exp\left(jk_0 \widehat{\mathbf{r}} \cdot \mathbf{r}'\right) \mathrm{d}\mathbf{r}'
\end{aligned}
\tag{2.24}
$$

Where $\widehat{\mathbf{r}}' = \frac{r'}{|r'|}$, while k_0 and η_0 are respectively the free space wave number and impedance. Matrices $\mathbf{J}^e_{pq}$ and $\mathbf{J}^m_{pq}$ contains electric and magnetic surface currents related to each UC and are reported in Eq. 2.25.

$$
\begin{cases}
\mathbf{J}^e_{pq}\left(\underline{d}_{pq}\right) \approx \frac{1}{\eta_0}\widehat{\mathbf{z}} \times \mathbf{k}^{inc}\left(\mathbf{r}_{pq}\right) \times \left[\overline{\overline{T}}_{pq}\left(\underline{d}_{pq}\right) \cdot \mathbf{E}^{inc}\left(\mathbf{r}_{pq}\right)\right] \\
\mathbf{J}^m_{pq}\left(\underline{d}_{pq}\right) \approx \left[\overline{\overline{T}}_{pq}\left(\underline{d}_{pq}\right) \cdot \mathbf{E}^{inc}\left(\mathbf{r}_{pq}\right)\right] \times \widehat{\mathbf{z}}
\end{cases}
\tag{2.25}
$$

In which r_{pq} is the barycenter of the each UC area, while $\overline{\overline{T}}_{pq}$ is the transmission tensor and is expressed in Eq. 2.26.

$$
\overline{\overline{T}}_{pq}\left(\underline{d}_{pq}\right) = \begin{bmatrix} T_{pq}\left(\underline{d}_{pq}\right)\rfloor_{TE} & T_{pq}\left(\underline{d}_{pq}\right)\rfloor_{TE/TM} \\ T_{pq}\left(\underline{d}_{pq}\right)\rfloor_{TM/TE} & T_{pq}\left(\underline{d}_{pq}\right)\rfloor_{TM} \end{bmatrix}
\tag{2.26}
$$

Therefore, according to this paper the "macro-scale" behavior of the structure is strictly related to tensor matrix elements that are controlled by the "micro-scale" descriptors D.

Chapter 3

Unit cell design

3.1 Materials presentation

As already explained in the first chapter, the main purpose here is to design a structure to be attached to a window establishing an Outdoor-to-Indoor link. So, the **material transparency** used for these structures turns crucial in this case.

The material transparency refers to the ability of material to let light pass through itself and is quantified by a parameter as the **light transmittance**, also, having highly transparent material is very important to avoid blocking the intended visual and environmental linkage between outside and inside spaces. Apart from this, another important consideration in material selection is a cost analysis of the overall expense. The goal would be to settle on a material that is cost-effective and easy to manufacture. This requires a balance between cost-effectiveness and functionality so that the material chosen will not be expensive for the project and will meet the required technical and operational needs.

In the light of these considerations, a careful review of what is already present in literature is necessary and at its end would appear that the so-called **transparent plastics** represent the best compromise. These materials represent a good choice for economic constraints and are also easy to be manufactured in view of prototype realizations, since they can be treated by additive manufacturing processes. Hence, they represent the best candidates that fulfill all the imposed constraints. Not all plastics are transparent and as specified in [35] the level of crystallinity and the presence of additives significantly influence the material's transparency and also, to enhance this transparency, various additives can be incorporated. According to all this features and to their good resistance to impact, this make them widely used today in several applications (as for optical devices and for packaging), especially in substitution to the glass, that is more expensive and less resistant.

However, this is not sufficient for the work purpose, indeed the selected material, apart from its mechanical and transparency features, needs to respect also electrical constraints. The electrical properties are those that have the strongest impact on the overall performance and these types of plastics usually are characterized by dielectric constants around $\epsilon_r = 2,4$ and dielectric loss $tan(\delta) = 0.0001, 0.01$.

This is confirmed in [36], where, by means of a Fabry–Pérot open resonator, that is a tool dedicated to broadband accurate microwave and mm-wave characterization of dielectric sheets, the measurement of the dielectric constant and loss tangent of various types of commonly used dielectric materials, such as semiconductors, electronic substrates, glasses, and plastics, in the 20–110 GHz range, as reported (see Figure 3.1). This is a very interesting paper, since finally, are provided some measurement about the dielectric constant of these plastics at high frequencies, that usually in literature could be found, but at low frequencies.

As it is possible to see, PETG Polycarbonate (PC) and PVC have higher dielectric constants compared to the others. This, in fact, implies a classification of these plastics based on their dielectric constant, as explained in [37], distinguishing between **polar plastics** and **non-polar plastics**. As reported in this website the dielectric properties of the polymers are highly dependent on their structure and it provides also a definition about the dielectric constant, as "the ratio of the charge stored in an insulating material placed between two metallic plates to the charge that can be stored when the insulating material is replaced by vacuum or air".

The classification of the plastics is based on their structure, which leads to a distinction among:

- **polar polymers**, where dipoles are created due to the imbalance in the electron distribution that tend to be aligned in the presence of an electric field. This will create the dipole polarization that will make this material good as insulators. Belong to this categories, as is possible to see in Figure 3.1, PETG, PC but also Polymethyl Methacrylate (PMMA) and PVC.
- **non-polar polymers**, that have symmetrical molecules and there are no polar dipoles present in them, due to this in presence of electric field does not align the dipoles. Here, electron polarization occurs due to the movement of electrons in the direction of electric field and these polymers have high resistivities and low dielectric constants.

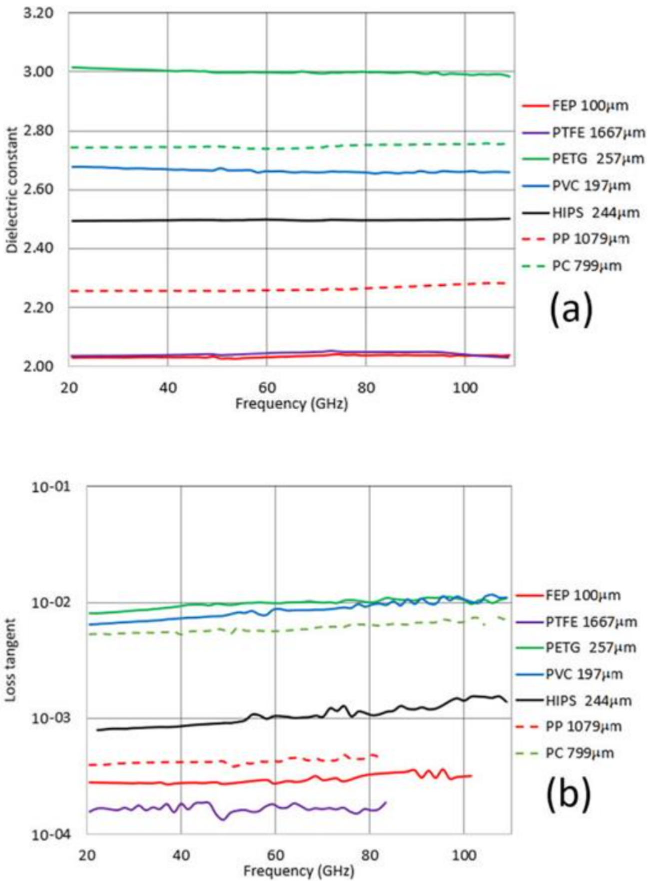

Figure 3.1: (a)Dielectric constant of common plastics, (b) Loss Tangent of common plastics [36]

Now, several materials are suitable for the structure implementation, as for example the PETG, PMMA and PC, because also in view of the prototype implementation they represent cost-effective materials with optimal transparency guaranteed. This is supported by data sheets for filaments available for 3D printing. For instance, on the website of the 3DJAKE manufacturer, one can purchase 1 kg of PETG or PC transparent filament of 1.75 mm/1000 g at 30€ and 35€ respectively and by looking for example just at the PETG filament data sheet it has a transparency of 90 %, means that the filament allows the 90 % of light to pass through. In view of this, an average estimation on their electrical properties make possible to conclude that good values for the material used to implement the following structures could be:

- $\epsilon_r = 2.7$
- $tan(\delta) = 0.01$

Where the $tan(\delta)$ is a parameter that describes the dielectric losses that a material suffers.

Since the SES must be integrated in a window, the idea explored here is to consider the presence of a layer or more of glass directly in the unit cell. There are several type of glasses that are used in buildings, the most common being **float**, **tempered** or **laminated** glass. The first refers to a very strong and durable glass obtained by floating molten glass on top of a bed of molten metal, that's the most common method to obtain the glass used for windows. Tempered glass instead results from a process that involves heating the glass and then cooling it quickly, this allows to obtain again a strong glass but with superior resistance to thermal and mechanical shock. Tempered glass is widely used in applications where people might accidentally bump into the glass or where the glass needs to handle extreme temperatures. For example, it's commonly used in shower doors, where people are close to the glass, and in large windows or glass walls in buildings, where the glass is exposed to significant heat from the sun and may also need to be strong against impacts. Finally, Laminated glass is fabricated by combining two or more panes of glass, using one or more plastic within panes. The plastic layer, usually of PVB (polyvinyl butyral), holds the glass layers firmly together in case of any breakage. This glass is strong and durable, hence does not break that easily. Laminated glass is very helpful in those places where safety matters, such as windows and doors that people frequently touch. It also works well to block out noise. Therefore, laminated glass is a good option for areas where lowering the noise is important, like offices or houses near busy roads.

In this section, are considered the features of the most common types of glass used for the windows in buildings. However, in order to place the SES in the windows of an industrial shed, it might be sufficient to only differentiate the windows based on the number of glass panes. The classification is very simple and does not require many explanations, in fact windows can be also distinguished as:

- **Single glazed windows**. When the window is made with a single glass pane, that typically goes from 3 to 12mm [38].
- **Double glazed window**. Already mentioned [28], are made by two glass panes of 4 mm or 6 mm and an air space within of usually 16 mm with the aim to create an highly insulating windows for both thermal and acoustic issues.
- **Triple glazed window**. Implemented to enhance the insulation properties of the double glazing window but increasing the total thickness that now can arrive to 48 mm.

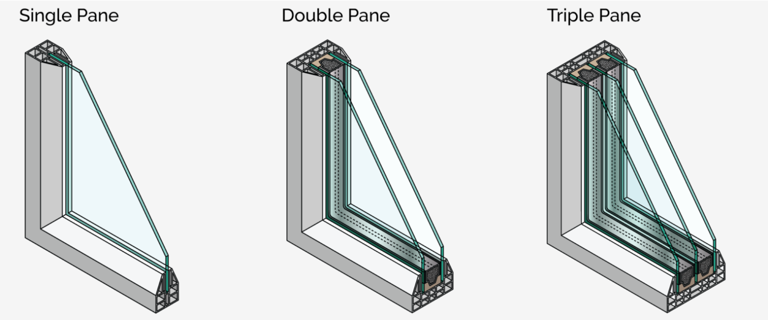

Figure 3.2: Single, double and triple glazing windows [39]

Since double and triple glazing are more commonly used in homes and office buildings, it is reasonable to assume that industrial plants are typically made by single-pane windows. Additionally, some of these windows might be made of the OT plastics previously mentioned, which are now used as a glass substitute due to their cost-effectiveness and durability.

3.2 Holed Structure UC

After properly introducing the materials, one can now introduce the first structure that is realized using only OT plastic and one glass pane. This represents a difference from what is present in literature at this moment, and it is one step further into the design and application of these materials, as compared to the structures mentioned in [29] and [30], since metallization is totally removed. In fact, traditional designs typically rely on the incorporation of a metallic part within the structure to achieve desired properties, but this design adopts a novel route by depending on dielectric-only materials.

The use of a totally dielectric unit cell seems particularly convenient for the application of interest, since the removing of a metallic part helps to improve the transparency of the structure, still providing good performance for this reason, several dielectric-only structures have been analysed, the most promising of which are described in the following, while their application to the design of TAs or SESs will be discussed in Chapter 4.

The first considered unit cell consists in a layer of glass and a layer of dielectric material, presenting a square hole whose side d is verified to control the behavior of the UC itself. The unit cell is represented in Figure 3.3.

It is characterized by the following quantities:

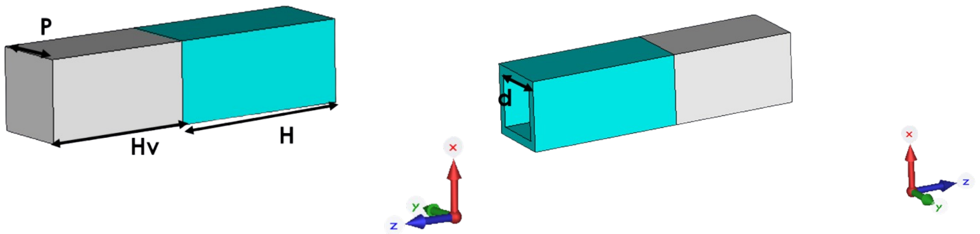

(a)   (b)

Figure 3.3: (a)Front view of UC, (b) Back view of UC

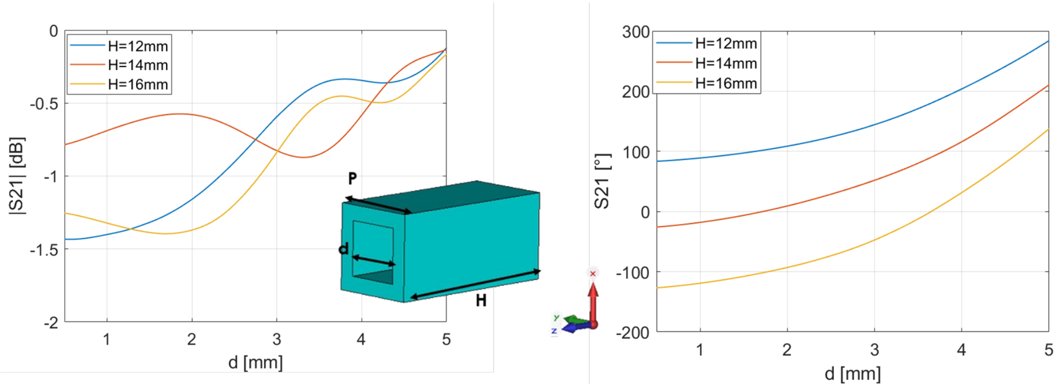

Figure 3.4: S_{21} module (left) and phase (right)

- H_v is the glass thickness.
- H is the plastic thickness.
- P is the cell periodicity.
- d is the diameter of the hole.

In order to cover the italian 5G frequency band that ranges from 26.5 GHz to 27.5 GHz the surface will be designed at the frequency of $f = 27$ GHz and this will give a periodicity of 5.55 mm obtained by setting it at $\lambda_0/2$.

With the help of CST Microwave Studio [31], the behavior of the UC, considering only the plastic pane for a first moment and that it is embedded in a periodic structure, is obtained. In particular, the variation of the amplitude and phase of S_{21} with respect to d for different values of H is studied. The results of this analysis, which are important for understanding how the plastic-only part affects the overall performance, are shown in Figure 3.4.

As is possible to see, for $H = 14$ mm there is the best module curve, which means it is the closest to the ideal value of 0 dB, while for $H = 16$ mm there is the highest phase range covered, around 260°, while with $H = 14\,\text{mm}$ and $12\,\text{mm}$ are covered only around 235° and 200° respectively and since the importance of the phase curve and the negative effects caused by phase errors have already been explained, a reasonable choice could be to fix the width to $16\,\text{mm}$.

Once that the thickness of the plastic block has been fixed to that value, has been carried out, now considering the glass and different values for H_v. The obtained plots are reported in Figures 3.5 and 3.6, while in Table 3.1 are listed the results of the mean value for the S_{21} module and the phase range.

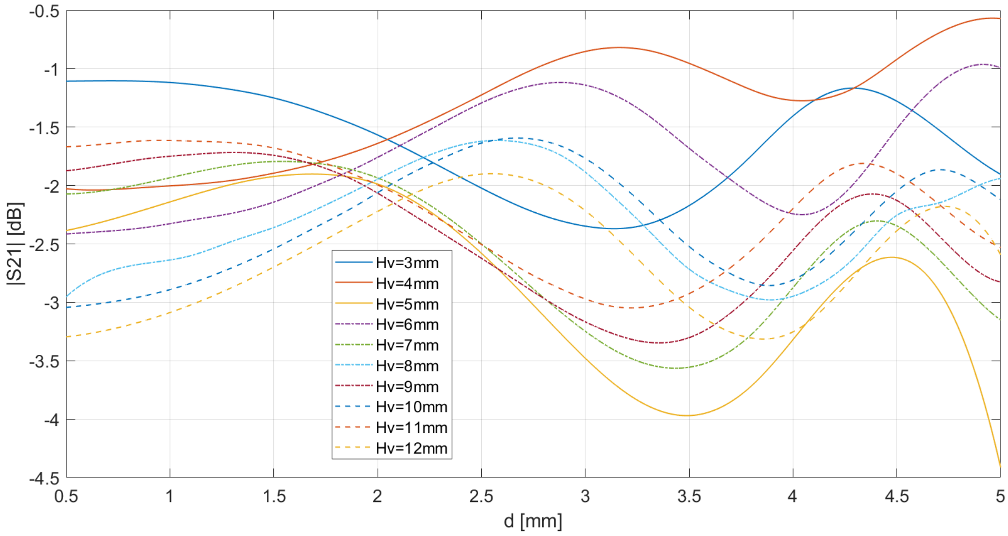

Figure 3.5: S_{21} module by fixing $H = 16\,\text{mm}$ and varying H_v

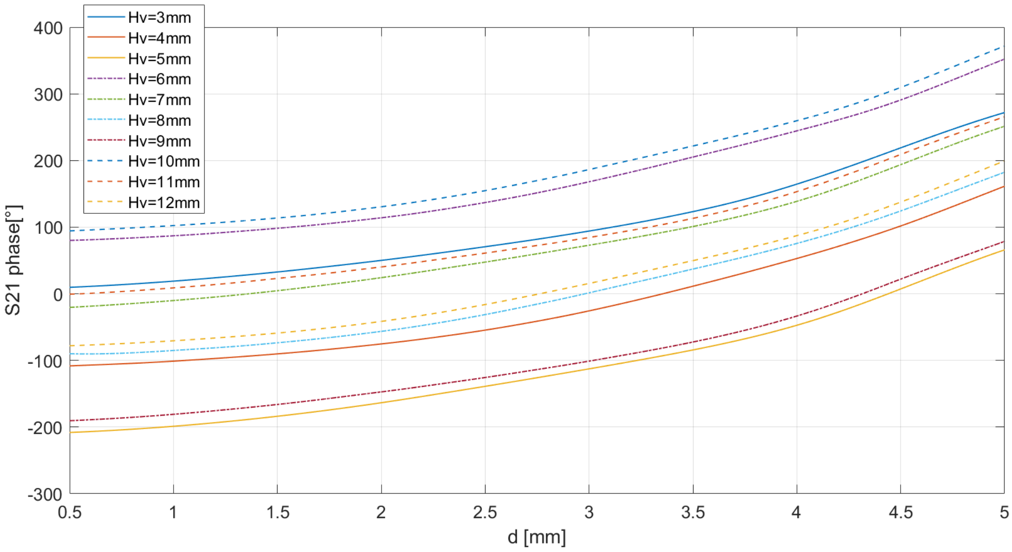

Figure 3.6: S_{21} phase by fixing $H = 16\,\text{mm}$ and varying H_v

H_v **[mm]**	$\lvert s_{21}\rvert$ **mean value [decibel]**	**phase range [°]**
3	-1.6255	262.26
4	-1.3406	269.66
5	-2.7876	274.04
6	-1.7519	272.22
7	-2.5275	271.8
8	-2.3114	272.67
9	-2.4058	269.08
10	-2.3086	277.37
11	-2.2054	266.22
12	-2.6222	277.38

Table 3.1: $|S_{21}|$ mean values and phase range.

From both the plots and the table, the values of H_v for which the module is the best optimal are 3 mm, 4 mm, and 6 mm.The reason why, is that considering an acceptable threshold of -2 dB, any value of H_v above this value is considered satisfactory with respect to performance.

Among these three values, $H_v = 6$ mm can be considered the best and the plots are reported in Figure 3.7. The reason for selecting this value is that it meets not only the threshold value in dB but also gives the widest range of phase.

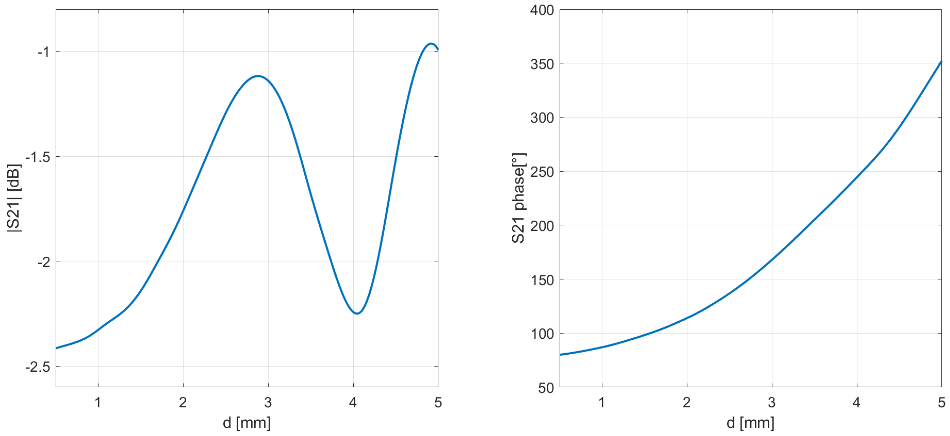

(a) (b)

Figure 3.7: S_{21} Amplitude and Phase UC of Fig.3.3

What could be interesting now is to analyse also variation of the reflection coefficient with d. The results of this analysis are reported in Figure 3.8, for the

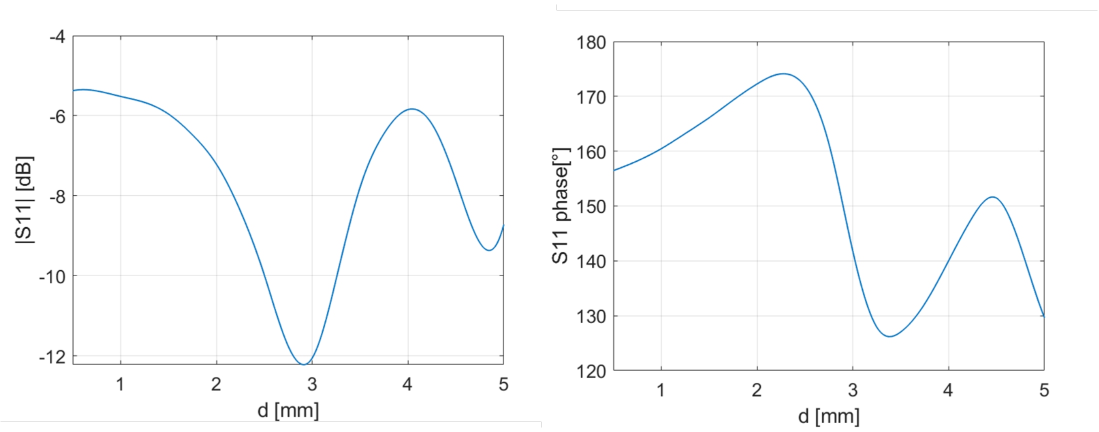

Figure 3.8: S_{11} module (right) and phase (left)

selected UC with $H_v = 6\,\text{mm}$ and $H = 16\,\text{mm}$. Here, it is possible to see that there is a negative peak in the magnitude in correspondence of a value slightly lower than $d = 3\,\text{mm}$ at the value of $-12.2\,\text{dB}$, which clearly corresponds to a positive peak in the transmission coefficient (about $-1.1\,\text{dB}$).

These results have been obtained considering normal incidence. However, since the field could impinge on the surfaces with other angles of arrival, it is necessary to study also the effect of this last, as well as what happens changing frequency.

The first results of this analysis are illustrated in Figure 3.10, where the incident angle, denoted as θ_i, varies within a range of $[0°, 70°]$ keeping $\phi_i = 0°$ (Figure: 3.9).

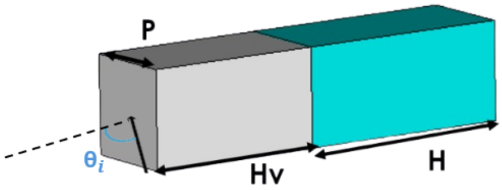

Figure 3.9: Different incident angles view

From the results presented in the plots, it is evident that the amplitude of S_{21}, or module, is the most sensitive quantity to changes in the incident angle. For angles up to approximately $\theta_i = 35°$, the curve maintains almost the same shape, while there is an important decrease in values as the angle increases. For incident angles greater than $\theta_i = 35°$, the curves begin to exhibit a significant difference in both shape and values. In particular, extreme negative peaks are observed, indicating a sharp decline in performance due to the presence of higher order resonances.

In the bottom plot of the same figure, the phase behavior is shown. From the different curves, one can notice that they exhibit an almost linear behavior for incident angles up to about $\theta_i = 50°$. More precisely, the curve has this nearly linear increase from $\theta_i = 0°$ to $\theta_i \approx 40°$ with only small deviations present at greater angles. In fact, non-linearity starts to emerge at around 40 degrees, but this only affects a little portion of the curve and is negligible. However, starting from incidence angle of $\theta_i = 55\,\text{degree}$, non-linear behavior becomes more pronunced. At this stage, the non-linear sections of the curve dominate the plot and tend to be even more as the angle increases, until the curve shows a sort of oscillating behavior, which suggests that the phase response is going to be increasingly unstable at higher angles.

This behavior indicates that the cell response is highly dependent on the incidence angle. For a small-angle range, the cell response remains rather stable. In the case of large angles, however, the cell significantly loses performance, in fact a noticeable negative peaks at high angles denotes possible weaknesses of the cell in highly angled situations.

As earlier mentioned, the other analysis is related to the UC's S_{21} behaviour at other frequencies in the considered band. This analysis reports that the UC designed at $f = 27\,\text{GHz}$ have good performance also if is simulated at the reported other two frequencies. Based on this, one can conclude that the cell is expected to work effectively across the considered 5G frequency band, which is defined in the range from $f = 26.5\,\text{GHz}$ to $f = 27.5\,\text{GHz}$.

3.3 Glass Only UC

A glass-only UC is designed here. This can be practically implemented using the unit cell represented in Fig. 3.12, where also the results in transmission coefficient amplitude and phase are reported for different height values. It essentially consists of glass block that will be holed but leaving 2 mm of the block without the hole. This section, which remains *un-holed*, has the specific purpose of preventing direct contact between the external environment and the holed part that due to the holes could be more fragile.

From the proposed UC results is noticeable that an interesting results arises for $H = 10\,\text{mm}$ especially in phase that will overcome 360°. The magnitude, on

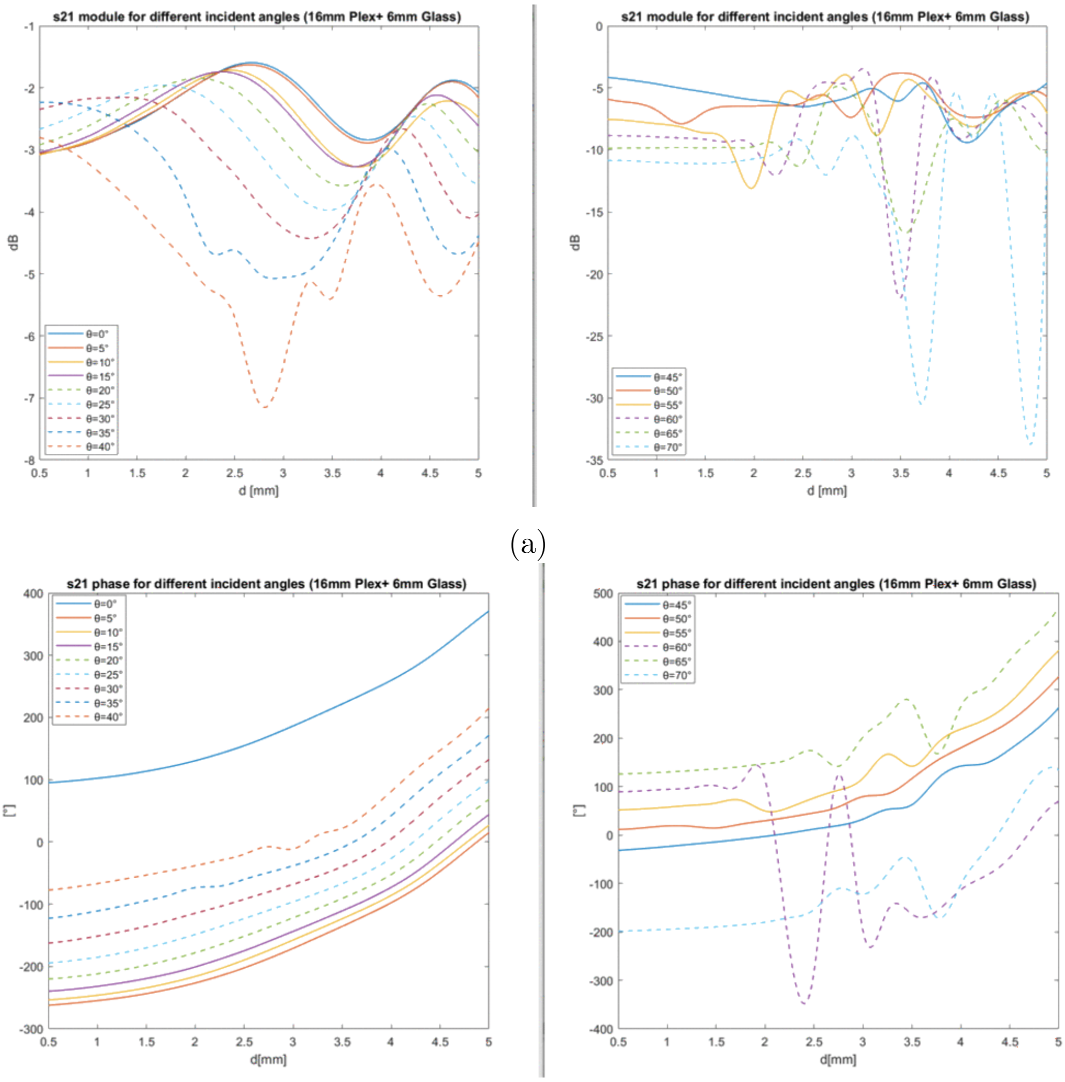

(a)

(b)

Figure 3.10

the other hand, does not assume good values. In particular, this occur for hole side values below $d = 3\,\mathrm{mm}$. Therefore an idea could be truncating the hole minimum side to this value and see also the phase response. The results are presented in Figure 3.13 and 3.14 show a module that oscillates between $-1.8\,\mathrm{dB}$ and $-0.4\,\mathrm{dB}$ and guaranteeing a phase coverage of almost 310° that represent very good performance for a UC.

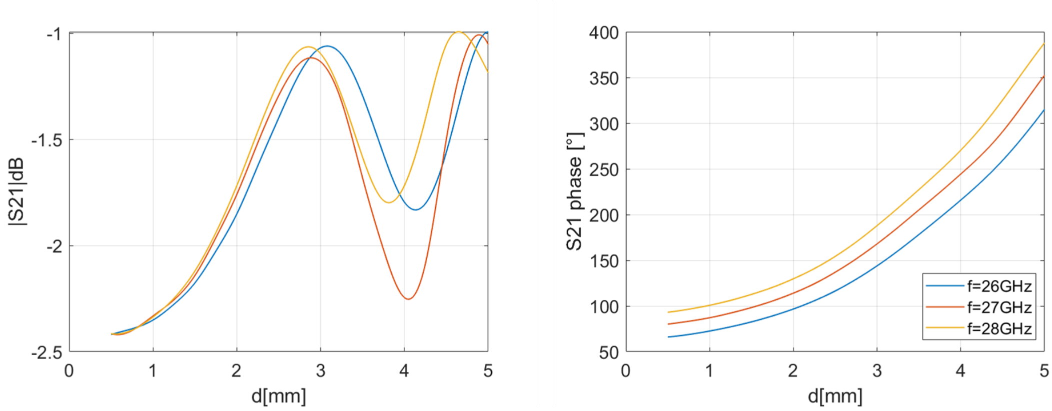

Figure 3.11: S_{21} module (left) and phase (right) for $f = 26\,\text{GHz}$, $f = 27\,\text{GHz}$ and $f = 28\,\text{GHz}$

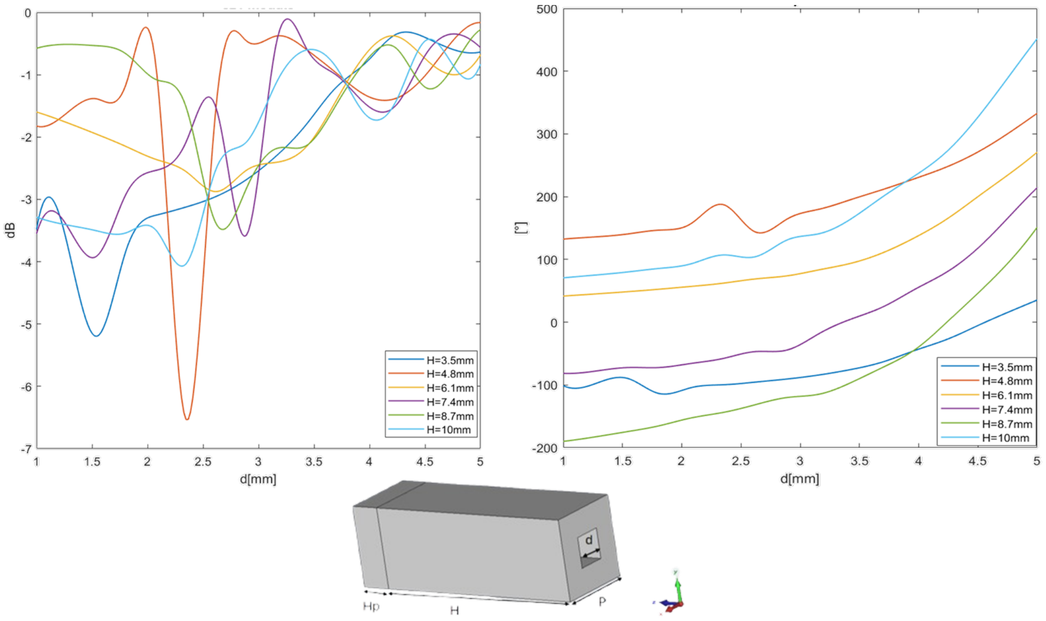

Figure 3.12: UC glass-only (bottom), S_{21} module (left) and phase (right)

3.4 Variable Heights UC

An alternative to the UCs proposed and analysed so far, could be the following one. It consists of a simple plastic blocks attached to the glass pane, where the height of the block will be the variable geometric parameter that provides the S_{21} curves. The reason why this UC is introduced is to provide an alternative UC that is easier to be manufactured, in fact the implementation of previous structures could be challenging, particularly concerning the realization of the holes. This is a problem to be considered if the idea is to perforate the plastic for example using a drilling machine. So if a drilling machine is used to perforate the plastic pane

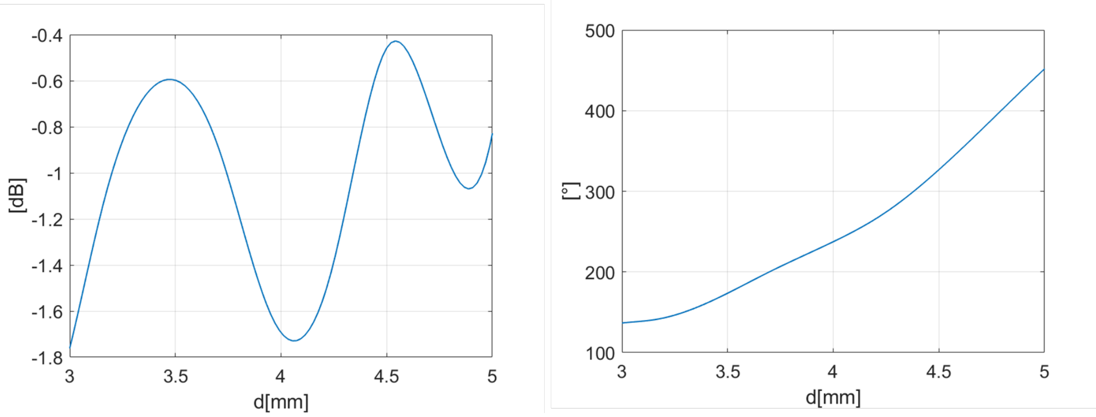

Figure 3.13: S_{21} curves for d truncated to 3 mm

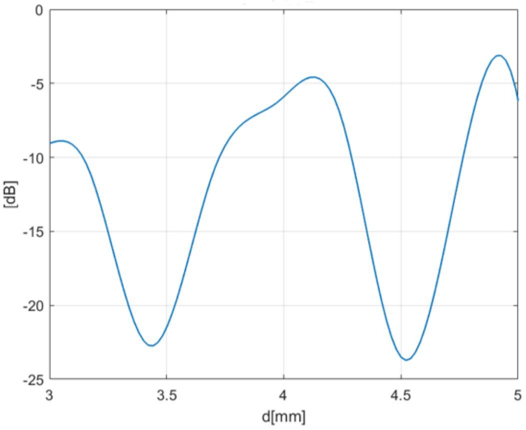

Figure 3.14: S_{11} amplitude for d truncated to 3 mm

to create the holes, is very difficult to think that a drilling machine could perform a perfect squared hole, because the most common drilling beats are circular, so in that case is impossible to generate that shape without rounding the edges. Another issue that needs attention is the resolution of the drilling machine, as high-resolution machines may not guarantee that very small holes, such as those of 0.5 mm can be realized. This problems are enhanced for the glass structure, since it is a more fragile material and adds also the cost issue that has always a strong consideration in the projects.

According to these considerations, let's start from the proposed UC, that as before is a good idea to initially consider just the plastic. The UC is shown in Figures 3.15, while in 3.16 and in 3.17 are reported the S_{21} module and phase and the S_{11} module. It is designed again at frequency of 27 GHz, with a periodicity of 0.5λ and height varies in the interval [1 mm,14 mm]. The module represent an oscillating behaviour that due to this, there's an alternation between positive and negative peaks, while the phase has a quite linear behaviour and covers a range of 260°.

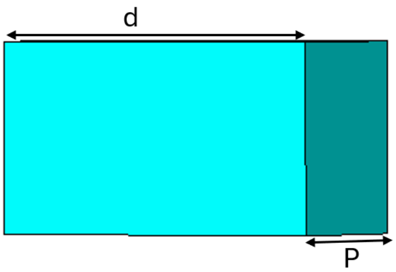

Figure 3.15: UC layout

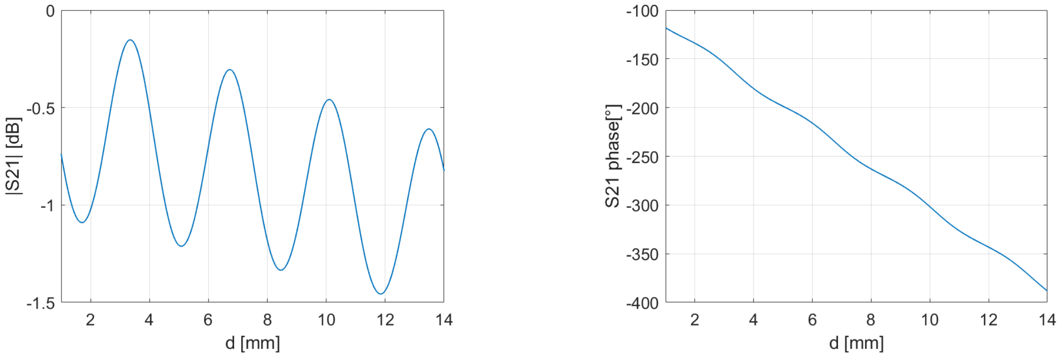

(a) (b)

Figure 3.16: S_{21} module (a) and phase (b)

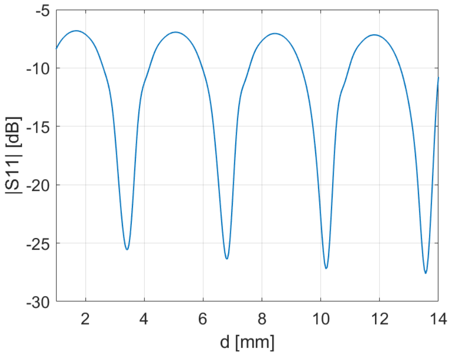

Figure 3.17: S_{11} module

Then a glass pane of 6 mm is inserted, the UC layout and the results for S_{21} module and phase are presented in Figure 3.18. Apart from the shape of the two curves that's the same as before, what is immediately noticeable is the curve of the module that suffered from an important reduction in values, which confirms again the reflection contribute taken by the glass. While, the phase curve keeps the same phase coverage as before.

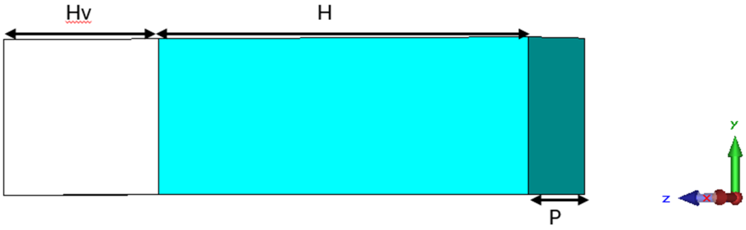

Figure 3.18: Variable Height Unit Cell plus Glass

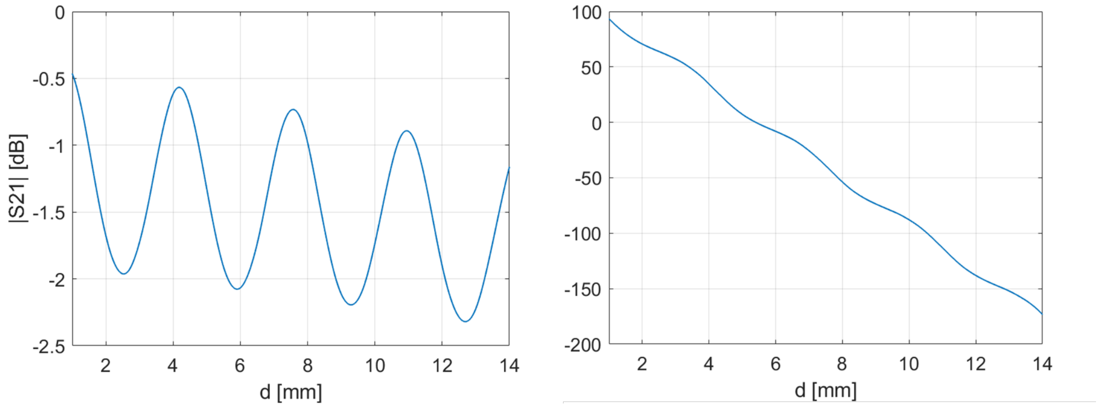

Figure 3.19: S_{21} module (left) and phase (right)

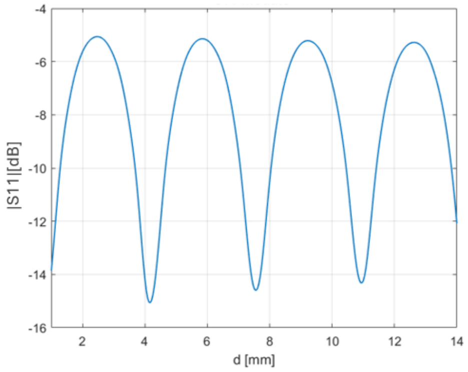

Figure 3.20: S_{11} Amplitude

3.5 Double parameter unit cell

The UCs considered until this moment exploit a single parameter variation to report their transmission capabilities and this could be a limitation if the performance of the cell needs to be increased. Therefore the proposed solution consists in having two geometric parameters in the structure that will vary. This will generate more than one curve for both S_{21} magnitude and phase, that consequently will produce a **surface** for each of them.

The idea at the base of this new approach for the analysis rely on, as before, finding the correspondence on the phase as first. However, having now a surface, this could happen for multiple values. Therefore, to have the final choice, from these values will be selected the one of them at which correspond the lowest value in reflection coefficient, that correspond to the one which will maximize the transmission. This method is described by a sort of hierarchical procedure, where finding the phase correspondence is at the top. Then, only if multiple matches occur, the second step aims to minimize S_{11}.

Following this procedure, a first UC is proposed and analyzed in Figures 3.21 and the related surfaces are reported in Fig. 3.22. The design parameters are the following: $H_v = 6\,\text{mm}$, $H = [0.9\,\text{mm}, 13.8\,\text{mm}]$ and $d = [0.5\,\text{mm}, 5\,\text{mm}]$, $f = 27\,\text{GHz}$ and $p = 0.5\lambda_0$. Another change in the layout is the hole, with a circular shape adopted to have also a representation in what happens with a different hole shape.

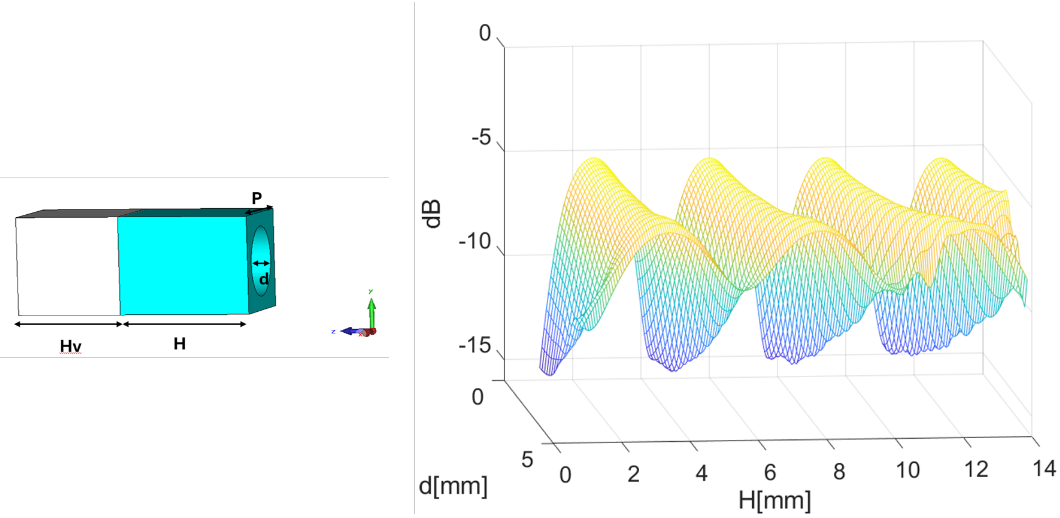

Figure 3.21: UC layout and S_{11} module surface

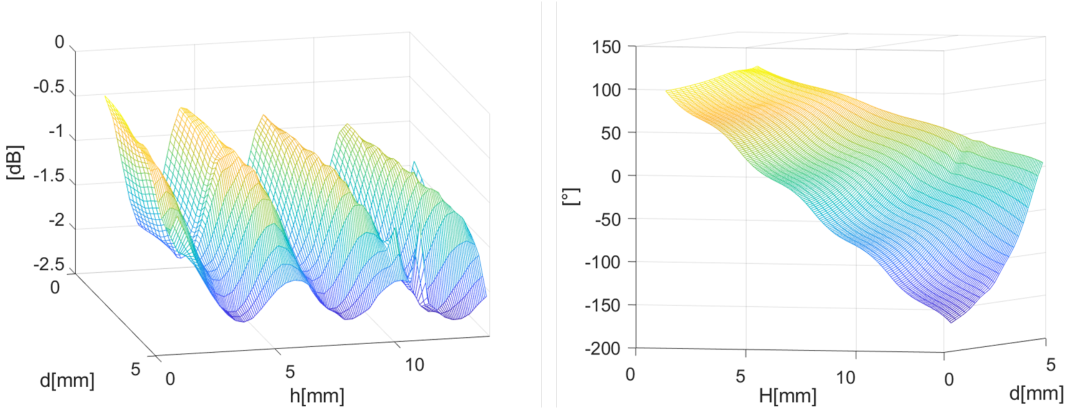

Figure 3.22: S_{21} Phase (right) and Amplitude surfaces (left)

The results show that the overall UC performance haven't much improved as expected, since the UC has the same shape as that analysed in Holed structure, indeed, phase coverage is about 278°, which very similar to previous cases, and the same happens for the reflection coefficient amplitude, which hasn't shown a net decreasing.

To achieve a more substantial reduction is necessary to do an important theoretical consideration that is very good explained in [40]. In fact, having a structure made by a glass and a plastic pane, in terms of electromagnetic field consist in having a multiple layer structure, due to the material difference, where each of them can be modelled by an equivalent transmission line (TL) model. Every TL that models a layer is described by the electric permittivity ϵ_i and magnetic permeability μ_i and their combination generates a very important parameter, the **characteristic impedance** of the medium Z_c, described by the equation 3.1.

$$Z_c = \sqrt{\mu_i/\epsilon_i} = Z_0/\sqrt{\epsilon_{eff}} \tag{3.1}$$

Where it can be also defined as the ratio within the characteristic impedance of the air Z_0 and the square root of the effective dielectric constant ϵ_{eff}. Just to understand what follows, the 3.1 is approximate substituting ϵ_{eff} with just ϵ_r, then considering that $Z_0 = 120 * \pi = 377\,\Omega$ and the mediums sequence is the following: air, glass, plastic and air. Consequently, the characteristics impedances will have in sequence the following values: $377\,\Omega - 142.5\,\Omega - 229.5\,\Omega - 377\,\Omega$.

From these numbers is possible to find a first clarification about the high reflections (it will be not only the one) that are introduced and this is due of the high difference in impedances that is present in the air-glass interface. Basically, since the mediums are modelled as TL, from the TL theory is known that, at the interface between two medium, the lower the difference between these two impedances, the lower the reflections will be.

This could be just a preliminary approach to justify, but is not the only thing that influence the reflections introduced by the proposed structures. Another for example, as could be imagined, is the thickness of the pane itself, where, always from TL theory in order to avoid multiple reflection is known that it needs to be $\lambda_g/4$. But, basing on these considerations, a good idea in solving that could be subdividing the structure in two parts, but one is now put before the glass. In this way the overall thickness will be the same, but the impedance of the plastic sheet is more near to that of the air now and this could help to reduce the reflections.

Actually, there is another thing by doing this changing that helps the match within the two impedances and is the presence of the hole. The holes present in the plastic pane will reduce the plastic density and this allows to let its characteristic impedance more similar to Z_0 than before. Is possible to find more details about this always on [40], where two figures reported also here (Figure 3.23) shows before the layout of the squared hole, evidencing the hole side with d and with W (cell width) and then the variation of the characteristic impedance in function to the ratio d/W with respect to different materials. The curves evidence the tendency of the material to have the same characteristic impedance of the air as the hole increases. Then is clear that, when $d/W = 1$ means that the cell is totally holed and $Z_c = Z_0$.

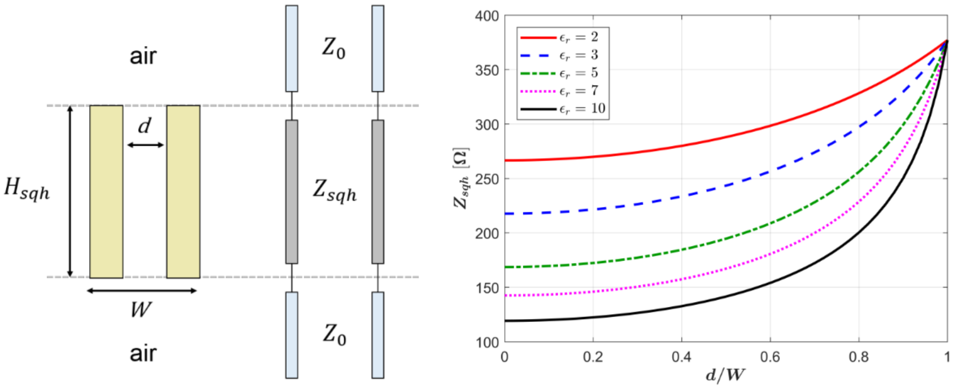

(a) (b)

Figure 3.23: (a)Squared hole Layout (b)Z_c with the variation of the ratio d/W and computed for different dielectric materials [40]

Considering all these information about the mediums, the variable double parameter analysis merged with a possible reduction in the glass pane, which now passes from 6 mm to 4 mm, an important reduction about the backlobe and the reflections is expected.

The UC analysed for this purpose is presented at Figure 3.24 with the S_{11} amplitude surface, where H_v is fixed to 4 mm, H vary in the interval [1,7] mm, d in [1,5] mm, the periodicity fixed to 5.55 mm and shows a phase variation around 300°.

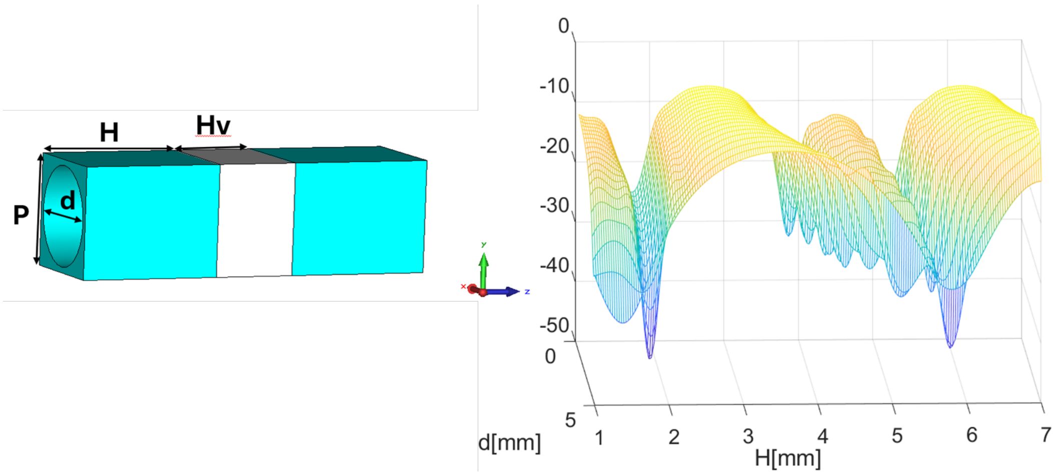

Figure 3.24: UC Layout (left) and S_{11} amplitude surface (right)

What's very interesting is the reflection coefficient module, shown in Figure 3.25 that as expected, now reports a very improvement reporting negative peaks, capable to reach also almost -45 dB, while the phase surface has a coverage around 300°.

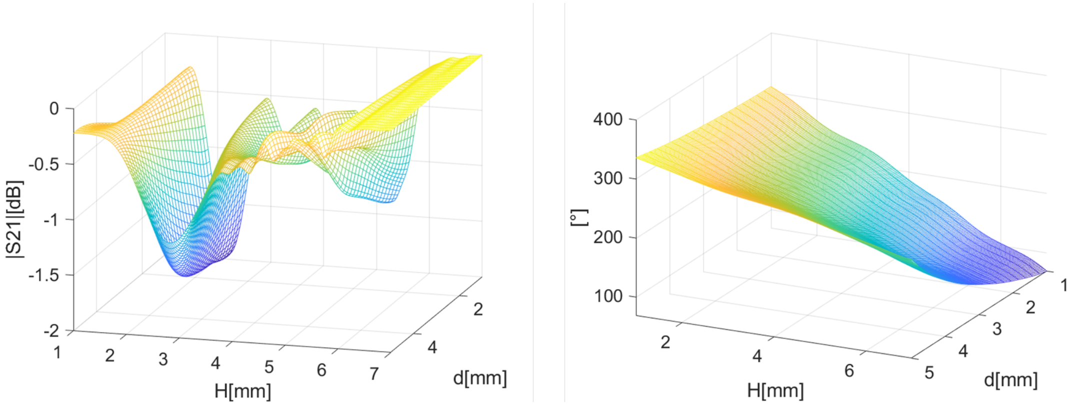

Figure 3.25: S_{21} Amplitude (left) and phase (right)

The previous UC was also simulated for a different incident angle due to the promising results in view of a SES realization, assuming an incidence of $(\theta_i, \phi_i) = (-10°, 0°)$. The results of the simulation are shown in Figures 3.26 and 3.27. The reflection coefficient reaches again around $-45\,\mathrm{dB}$, while the phase surface suffers from a reduction to 240°. For the same reason for which was before introduced, a structure which follows the same idea but only with variable heights could be now presented. The double parametric analysis here rely on parametrization of both heights of the UC (H_1 and H), this means that, while the previous structure was symmetric if looked from one side, this will be no more (Figures 3.28 and 4.33).

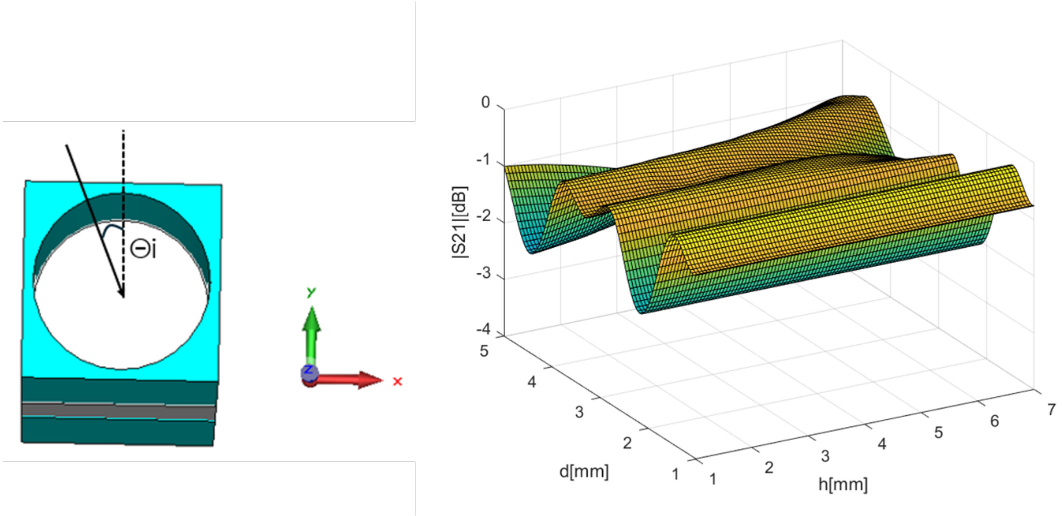

Figure 3.26: UC layout and S_{21} amplitude

The behavior is almost the same as before where a minimum of almost $-40\,\mathrm{dB}$ is obtained for the S_{11} amplitude, that is a little bit higher than before and the

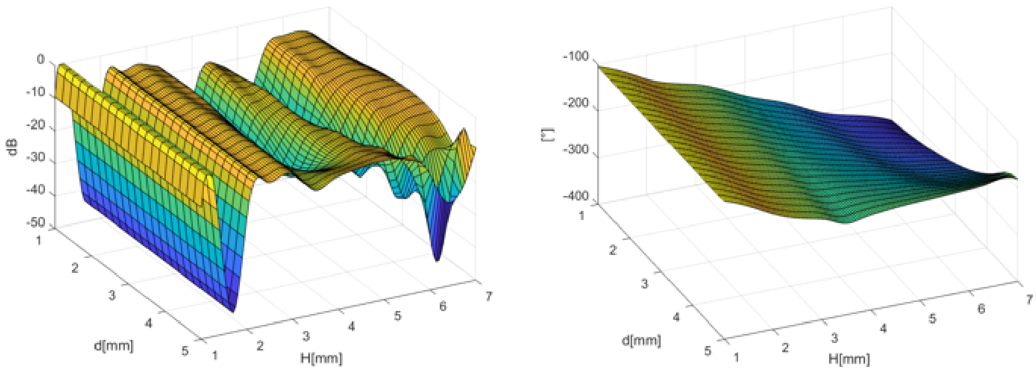

Figure 3.27: S_{11} amplitude (left) and S_{21} phase (right)

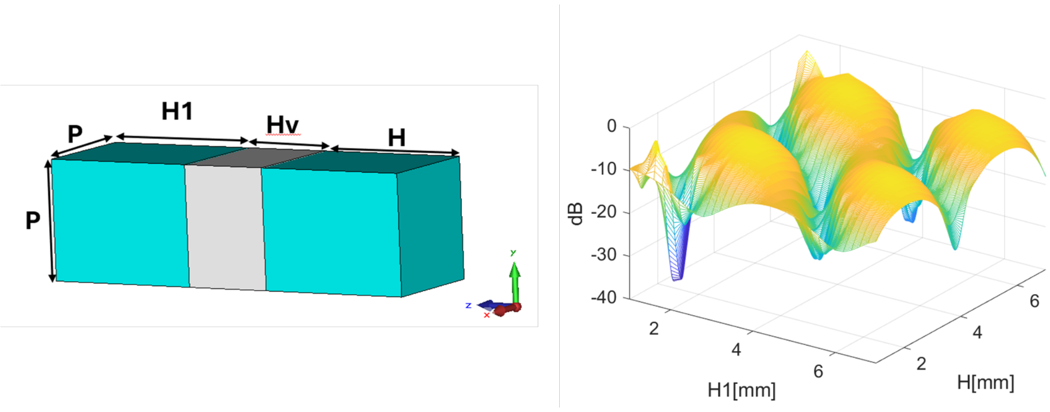

Figure 3.28: UC layout and S_{11} amplitude

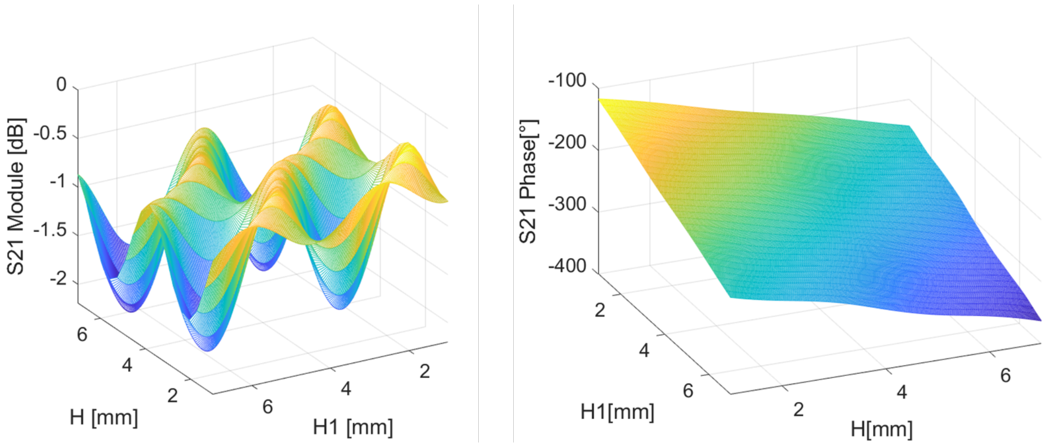

Figure 3.29: S_{21} Amplitude (left) and phase (right)

phase has instead almost the same variation.

Chapter 4

TA/SES design and numerical analysis

4.1 Introduction to TA/SES design and analysis

All the unit cells presented in Chapter 3 have been introduced to check their validity. The UC design and analysis, as already stated is the first step that has to be performed in view of TA/SES realization. In fact, the aim of this Chapter is to implement the structures related to the unit cells introduced before.

4.2 Holed Structures

Using the unit cell introduced in Section 3.2, first a TA has been designed. The considered geometry is shown in Fig. 4.1. The TA has a diameter of 23 UCs, equal to $D = 12.78\,\mathrm{cm}$ and it is discretized with 421 UCs. The feed is a circular horn located at a distance $F = 11.50\,\mathrm{cm}$ ($F/D = 0.9$). from the planar surface. The angle between the line orthogonal to the TA and the field impinging on its center is $(\theta_i, \phi_i) = (0°, 0°)$ and is designed to focus the transmitted field in a direction characterized by $(\theta_{max}, \phi_{max}) = (0°, 0°)$. The phase map that the transmitarray must provide to satisfy these constraints is shown in Figure 4.2.

The antenna is simulated with CST Microwave Studio [31], and the Radiated Pattern in E-Plane and H-Plane are shown at Figure 4.3, while in Figure 4.4 is reported the behavior of the gain vs frequency.

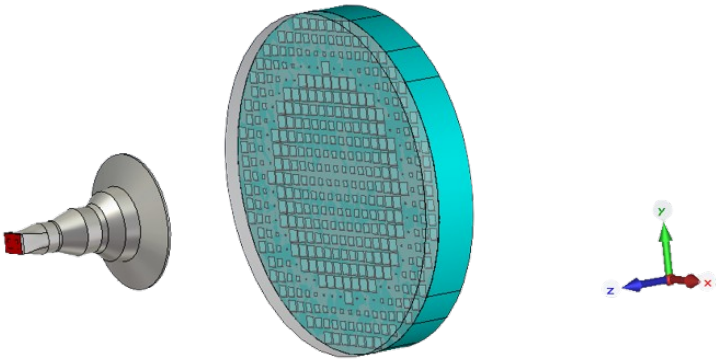

Figure 4.1: Transmitarray Antenna based on Holed UC

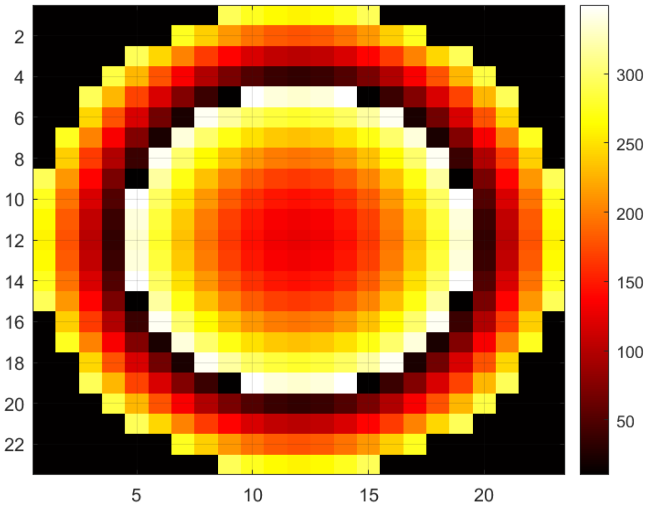

Figure 4.2: Phase Map

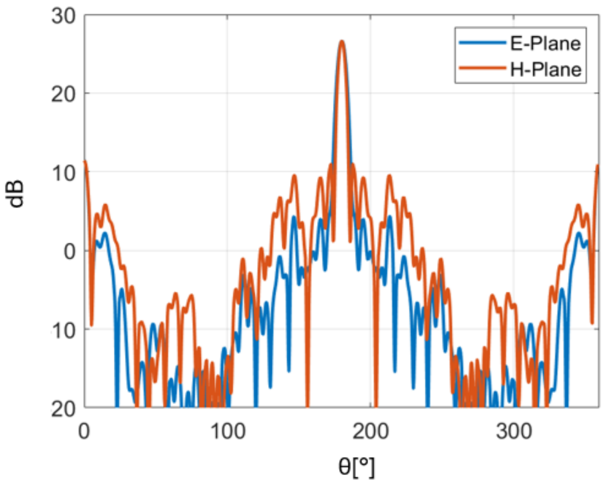

Figure 4.3: Gain variation vs frequency

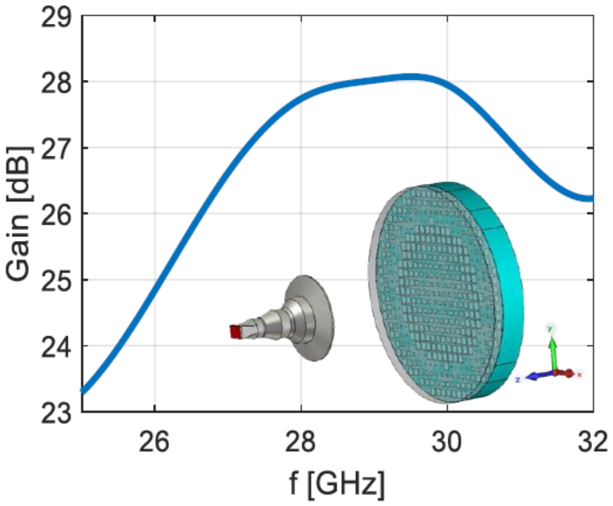

Figure 4.4: Gain variation vs frequency

These results confirm the effectiveness of the proposed UC, the $-1\,\mathrm{dB}$ bandwidth is approximately equal to $14\,\%$ and the aperture efficiency is $39\,\%$ at $27\,\mathrm{GHz}$.

To design the SES it is sufficient to remove the feed and substitute it with an incident plane wave. But before to see what happens in that case, could be worth exploring what happens when the horn is distanced.

In Figures 4.5 and 4.6 the Phase Map and the Normalized radiation pattern in E-Plane and H-Plane respectively, when the horn is distanced at $F/D = 5$ are shown.
From the phase map it emerges that the range of values is significantly decreased respect to the previous case, while before covered almost the entire phase range, now a variation of only 100° is obtained (180°,280°). This is justified by consider-

ing how can be computed the quantity that represent the distance from the horn to each cell of the structure.

$$R(i,j) = \sqrt{d(i,j)^2 + F^2} \tag{4.1}$$

The R term, which represents the distance from the horn to the each UCs, is evaluated considering the distances from the cell to the centre of the transmitting part (d) and the focal distance (F). This let $R = f(d)$. But here happens that the focal distance F is much larger than the distances d. This means that R is less sensitive to d changing.

While looking at the radiation pattern high side lobes, especially in the H-Plane are visible. This is due to the feed being far from the transmitting surface and in this condition the contribution of the incident field become more evident respect than the transmitted one.

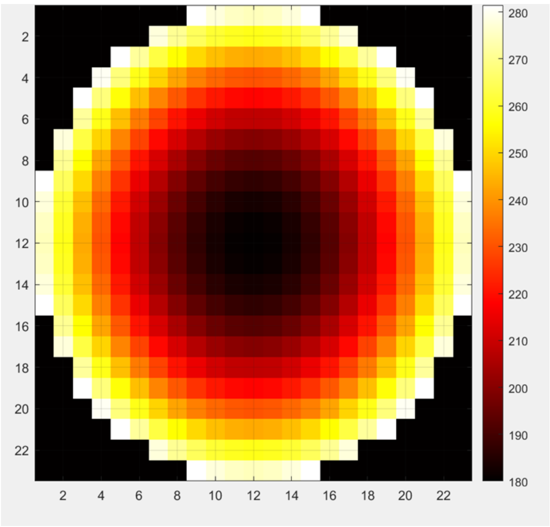

Figure 4.5: Phase Map for Holed TA structure when $F/D = 5$

The SES is now implemented and the idea was to implement a circular SES with 40 elements to the main axe, keeping the same configuration for the parameters used in the TA. The idea is now that an incoming beam that arrives at $(\theta_i, \phi_i) = (0°, 0°)$ is focused to ($\theta_b = 20°$,$\phi_b = 0°$). So, this is done again at $f = 27\,\text{GHz}$, $p = 0.5 \cdot \lambda_0 = 5.55\,\text{mm}$ and will produce a structure diameter of $222.22\,\text{mm}$.

With this configuration and basing on the phase map evaluated in Figure 4.7,

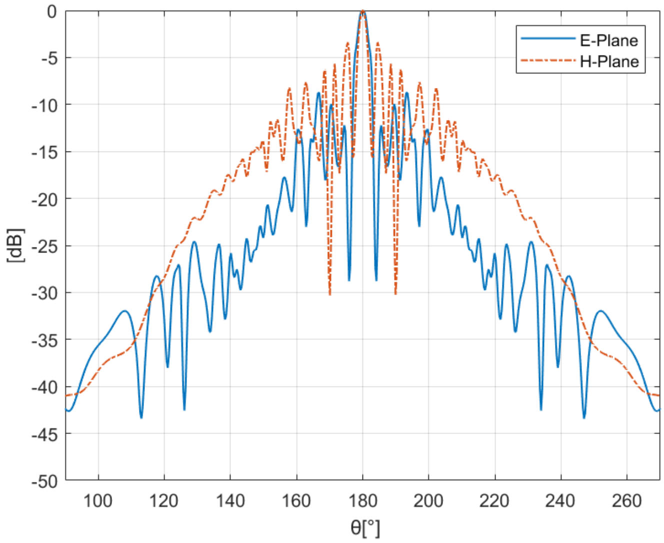

Figure 4.6: Normalized Radiation Pattern for Holed TA Structure when $F/D = 5$

is possible to obtain a Radiation Pattern as that shown in Figure 4.7. What is important to underline before the analysis continues is about the reported 3D view, which is the Farfield **Radar Cross Section** view and no more the gain.

This is something that was not possible to choose, because when in CST are simulated structures with an incident plane wave, the results are given in RCS and no Gain or Directivity are provided. As the name suggests, RCS is something that belongs to Radar measurement and is strictly related to their working principle. Indeed very briefly, a radar is a device able to detect an object by the transmission of a signal to the object itself, the the signal will be reflected by the object and the reflected signal will be collected again by the radar. So, the RCS represent the equivalent area that will reflect the radar signal and for how it's defined, represent how the object can be visible by the radar itself.

One more clarification about this consists in the type of RCS that is provided by CST, that is the **bistatic** one, in fact, RCS can be **monostatic**, **bistatic** and **multistatic**. Essentially, basing on the radar working principle, they are different one from the other respect to the position of the transmitting and receiving parts of the radar, that for the monostatic are in the same position, for the bistatic in two different positions and for the multistatic there are more receivers in different positions.

Is possible to conclude that the proposed circular structure with 40 cells on the main axis, made by 1250 element totally, that has an area for the entire structure

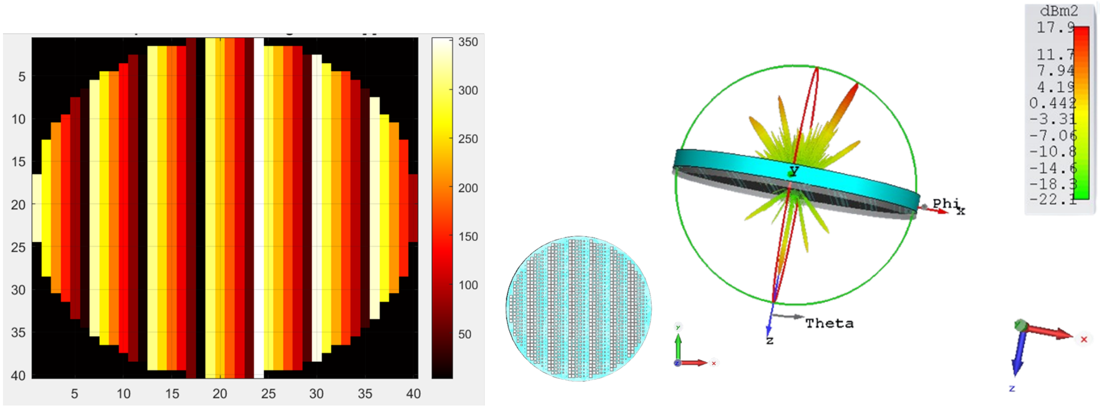

Figure 4.7: Phase map circular SES (left) and RCS 3D view (right)

of 387.84 cm^2, produces a main beam on the desired direction with a maximum of 17.9 dBm^2.

Let's see what happens implementing the same structure but rectangular, made of 31 elements width and 40 height. Phase map and the 3D view of the RCS are visible at Figure 4.8.

Now, this example has the importance to highlight that with the same number of elements, an occupied area of 381.95 cm^2 that is less than the circular one, the rectangular SES has a maximum of the RCS main lobe of 0.5 dBm^2 higher, now reaching 18.4 dBm^2. This is shown in Figure 4.10 in which the 2D view of E-Plane and H-Plane are reported respectively. The information about the scattered angle is represented in E-Plane, in fact the SES is designed again to focus an incoming plane wave from $(\theta_i, \phi_i) = (0°, 0°)$ to $(\theta_b = 20°, \phi_b = 0°)$, but these values are referred as transmission angles. However, generally has to be considered that theta goes from 0° to 360° and it is defined along the green line (for $\phi = 0°$) that is visible in 3D view, present in both Figures 4.7 and 4.8. This means that 20° on the transmitting side are 160° considering the entire structure.

Another interesting illustrations is that provided in Fig. 4.9, where are evaluated the differences between the phase values required and those who are assigned considering the S_{21} phase curve for each cell. This difference will be identified as **error** and is a graphical representation of the problem explained in Section 2.4.

The analysis can actually focus on which are the effects when the periodicity changes. The table 4.1 will summarize the result of the analysis obtained by increasing the cell periodicity to $p = 0.55, 0.61, 0.65 \cdot \lambda$.

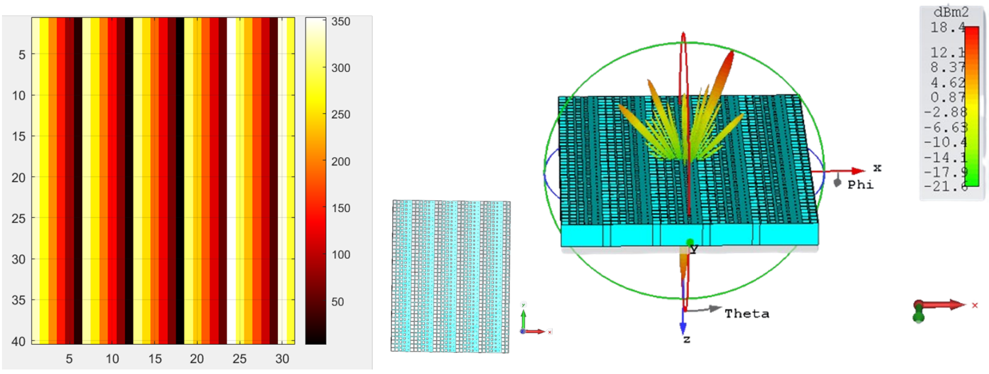

Figure 4.8: Phase map rectangular SES (left) and RCS 3D view (right)

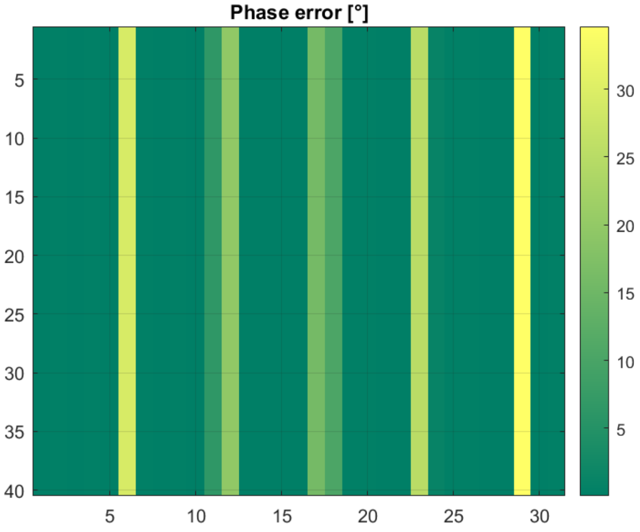

Figure 4.9: Phase error map

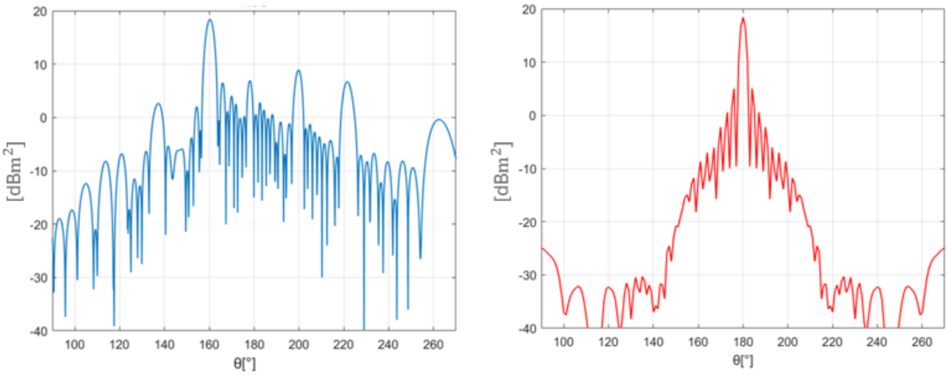

Figure 4.10: RCS in E-Plane (left) and H-Plane (right)

Clearly, as the cell periodicity increases, the maximum side of the hole can increase too, however, in order to graphically compare the results for the selected height and in the same range, the graph needs to be adapted to maximum side of the lowest periodicity and is reported in Figure 4.11.

From both table and figure can be easily seen that an interesting behaviour happens when the periodicity has a value of $0.55\lambda = 6.1\,\text{mm}$. Therefore, a good idea, looking that the transmission phase curve variation is also good for $H = 14\,\text{mm}$, is to implement the structure with these values which also helps to reduce the structure thickness. The front view will be as that on the bottom of the figure 4.8, what changes is the thickness as previously mentioned and the area, that clearly will increase to $461.33\,\text{cm}^2$.

H **[mm]**	$p = 0.5\lambda$	$p = 0.55\lambda$	$p = 0.61\lambda$	$p = 0.65\lambda$
8	138.89	168.41	151.03	158.97
9	155.79	187.24	169.29	177.78
10	167.41	201.04	181.9	191
11	187.81	225.48	203.62	213.81
12	207.18	249.46	225.9	237.24
13	217.12	262.87	237.76	249.51
14	234.27	281.76	254.25	267
15	259.31	308.75	279.9	293.31
16	272.34	326.34	296.78	310.51

Table 4.1: S_{21} phase range for different height and periodicities.

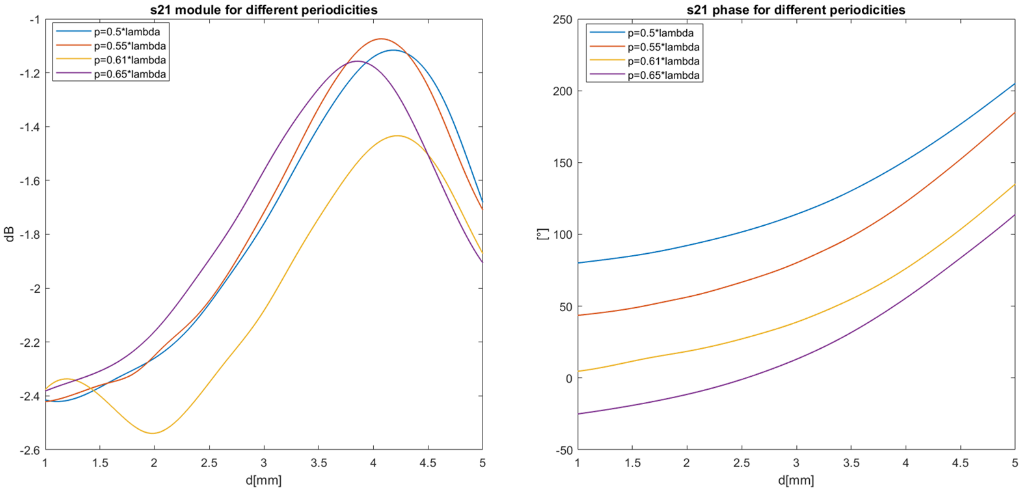

Figure 4.11: S_{21} module and phase for $H = 16\,\text{mm}$ and different periodicities

.

The RCS in E-Plane and H-Plane are shown in Figure 4.12 and 4.13 reporting an improvement in the main lobe to 20.4 dB.

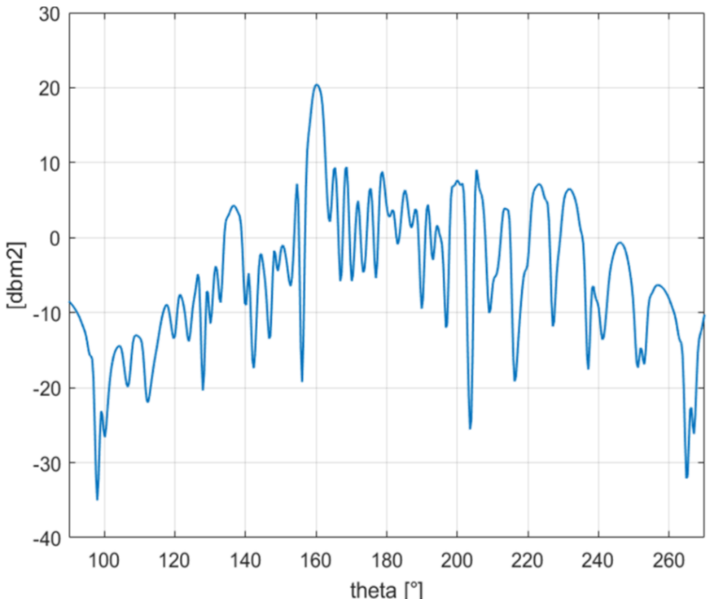

Figure 4.12: RCS in E-Plane for periodicity 0.55λ

A final structure has been developed and simulated for two main purposes. The first one, since the structure will be designed at the frequency of 28 GHz, is first of all, to see the structure performance at this other frequency, where a partial information was already given at Figure 3.11.
Then, the structure will be simulated on both CST and HFSS [20], this permits to compare the results obtained by the two software. The similarity between the two results, if it occurs, will serve as partial confirmation of the simulations correctness.

The layout is again the same as the reported in bottom of Figure 4.10, but as the previous introduced structure, the periodicity is set to $0.55\cdot\lambda$ and the plastic sheet to 14 mm and the SES has to focus an incident beam from $(\theta_i, \phi_i) = (0°, 0°)$ to $(\theta_b = 20°, \phi_b = 0°)$ An advantage respect to the structure simulated in Figure 4.12 consists in a reduction of the occupied area, due to the frequency increasing that will reduce λ now the cell periodicity is $p = 5.89\,\text{mm}$ ($\lambda_0/2$ @ $f = 28\,\text{GHz}$) instead to the $p = 6.11\,\text{mm}$ from before, that will generate a total area of $430.18\,\text{cm}^2$.

Then, the structure is simulated and the results obtained for the bistatic RCS are shown in Figure 4.14. From this representation is possible to see that generally the RCSs are so similar. For example, the main lobe has almost the same magnitude in both graphs, this can be seen from the reported legends, where one reports the values until $20\,\text{dBm}^2$ and the other until $20.7\,\text{dBm}^2$.

To better perform the comparison is necessary to put together the 2D-view and

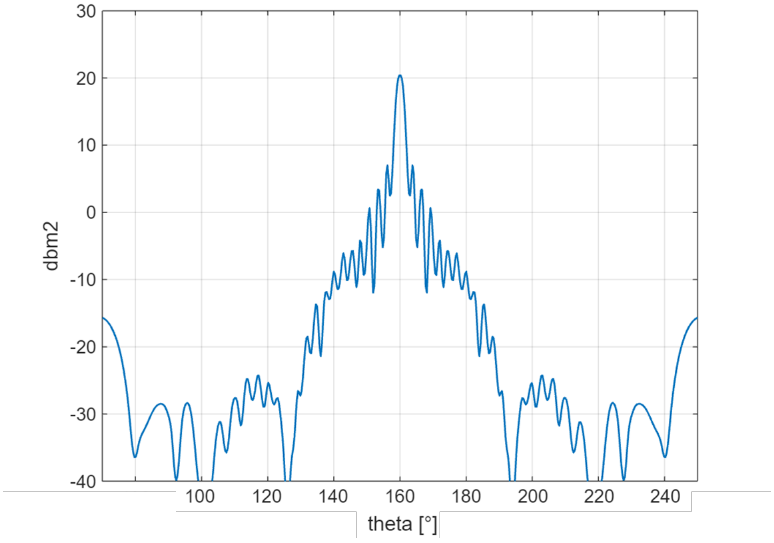

Figure 4.13: RCS in H-Plane for periodicity 0.55λ

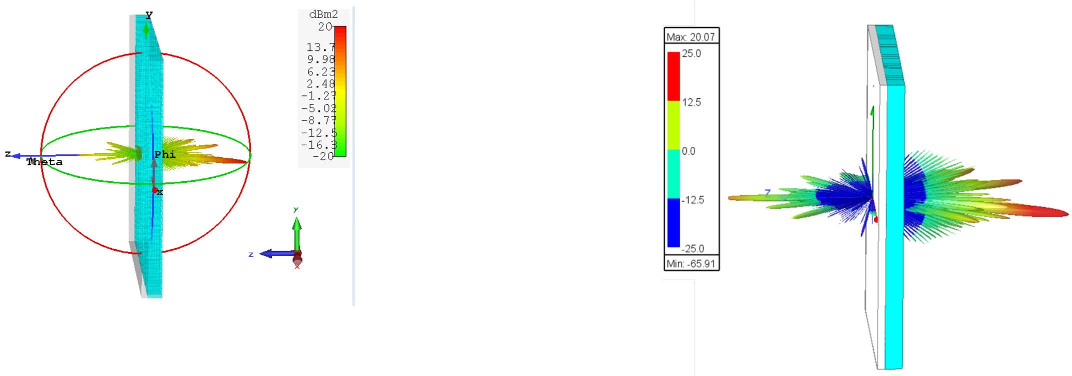

(a)

(b)

Figure 4.14: (a)3D view of the RCS on CST (b) 3D view of the Bistatic RCS on HFSS

this is provided at Figure 4.15 where the comparison is shown in the E-Plane and confirms what was previously predicted about the similarity of the patterns.

4.3 Glass-Only SES

The analysis of the UC presented in Section 3.3 can continue by implementing the SES. The design features are again: frequency of 27 GHz, 31x40 elements with periodicity 0.5λ that gives 172.22 mm width x 222.22 mm height and designed to

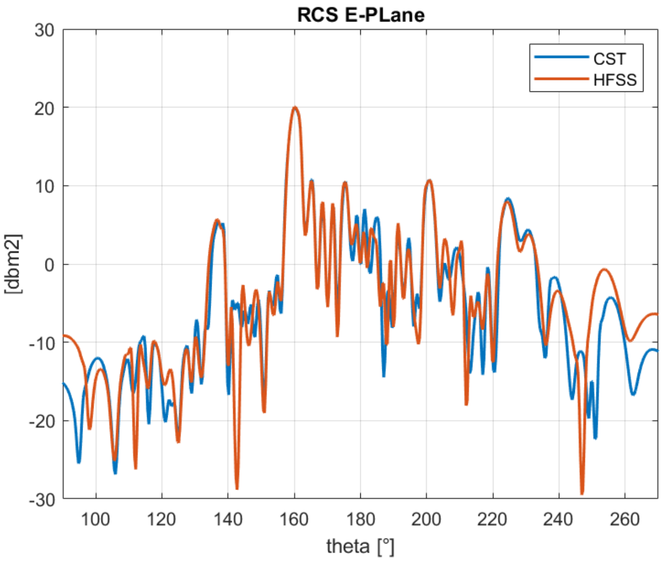

Figure 4.15: Comparison between Bistatic RCS obtained in CST and HFSS

focus an incident plane wave from ($\theta_i = 0°$,$\phi_i = 0°$) to ($\theta_b = 20°$,$\phi_b = 0°$). The phase map will be the same as that in Fig. 4.8 due to frequency, periodicity and dimension are the same, while the layout and the simulations are illustrated at Figure 4.16 and 4.17 and shows very interesting results.

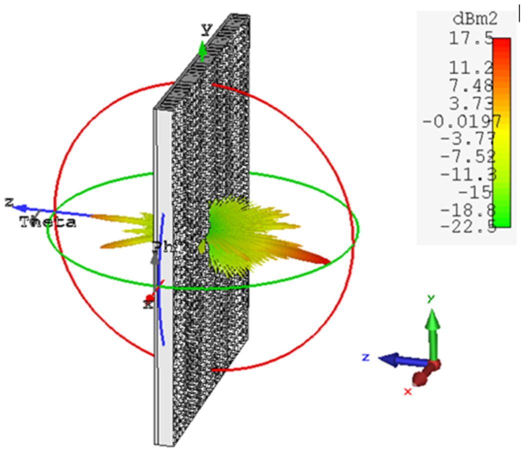

Figure 4.16: Glass-Only SES layout

The just proposed structure represents an innovative idea to directly use the window to transmit inside a building with the minimum visual impact. In this way, the window that is part of the building itself, goes from being the cause of signal attenuation to a transmitting surface capable of directing the signal within the structure itself. This will perfectly belongs to the definition of Smart

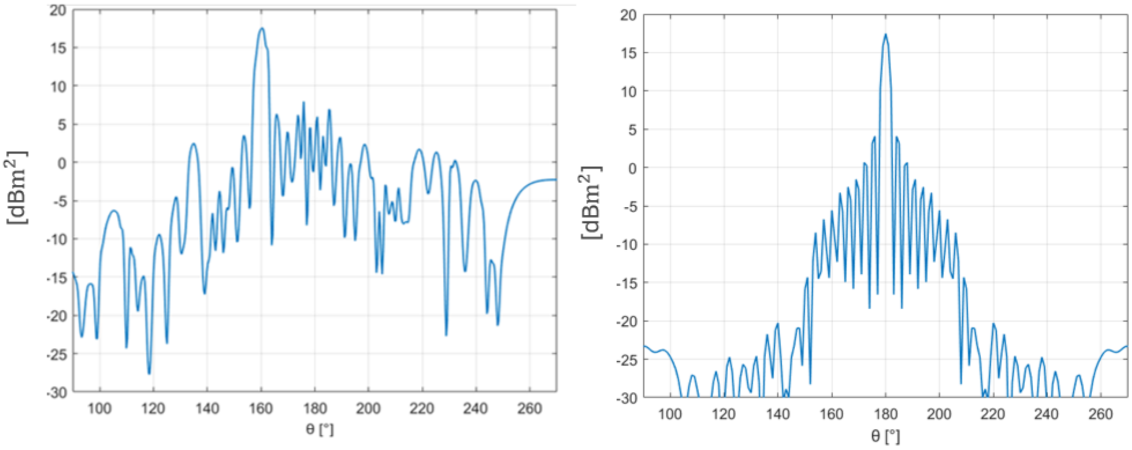

Figure 4.17: RCS in E-Plane (left) and H-Plane (right)

Electromagnetic Environment provided at the very beginning of the work, in which now the environment becomes a resource.

However, there are considerable disadvantages to working under this structure. One significant challenge is related to the material itself, indeed it is recognized that it is sensitive. This fragile nature has to be considered in the manufacturing process, requiring cautious in handling with this material. Glass, particularly for advanced applications, requires more careful handling in processing, shaping, and installation respect to other materials such as plastics, which can complicate the general procedure.

Then, glass utilized in existing structures is available in a diverse range of types, each with distinct characteristics and applications, as previously discussed at the beginning of this chapter. This brings up another important point, the electrical properties of building materials doesn't represent a focus for the windows manufacturers. Typically, the mechanical strength and thermal qualities of the glass are the most important features in construction, indeed they are crucial for maintaining the building's structural integrity and efficiency. However, if specific electrical properties are required, such as for electromagnetic purposes as those of this work, it may be necessary to replace the current glass with another that meets these new specifications.

4.4 Variable Height

The SES implemented following the first UC presented in Section 3.4. The first one without glass is made with the same dimensions as before (Fig. 4.18), therefore 31x40 elements and designed in order to focus an impinging plane wave from $(\theta_i, \phi_i) = (0°, 0°)$ to $(\theta_b = 20°, \phi_b = 0°)$ and the results are reported in Figure 4.19, where a maximum of 18.6 dBm^2 in the main lobe is measured.

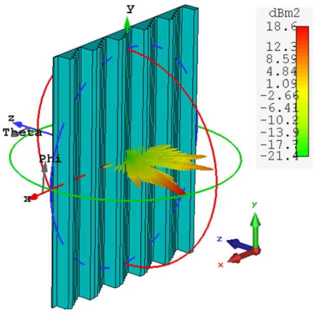

Figure 4.18: SES layout

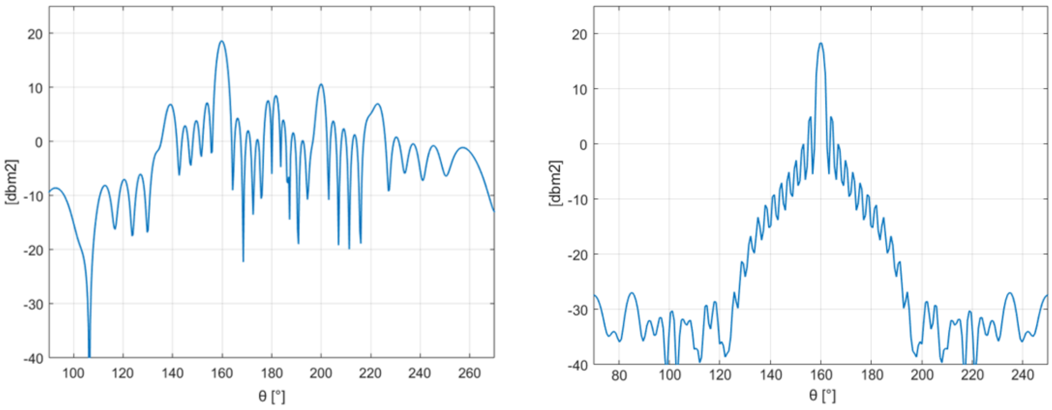

Figure 4.19: RCS in E-Plane (left), RCS in H Plane (right)

Then by adding the glass the simulated SES is shown at Figure 4.21 and is possible to see that the reflections introduced by the glass seems that doesn't affect the overall performances on the transmitting side, since again is ensured a maximum in the main lobe of 18.7 dBm^2, which is almost equal to the previous one. However, by looking at the **back lobe** is possible to see the bad effect introduced by the glass. The back lobe is an important part of the radiation pattern since it represents the contribution of the incident field which is reflected. Quantity that clearly has to be reduced as much as possible since the desired SES works in transmitting mode and the contribute reflected has to be as low as possible. By looking at the back lobes introduced by the two structures and reported at Figure 4.22 is possible to see the differences in maximum value from the SES with glass and that w/o glass. The difference is very clear and reports a maximum of 12.6 dBm^2 and 8.6 dBm^2 for the SES with glass and without respectively, providing a consistent difference of 4 dBm^2.

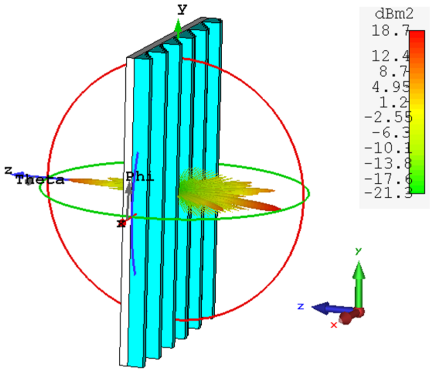

Figure 4.20: SES Farfield 3D-view

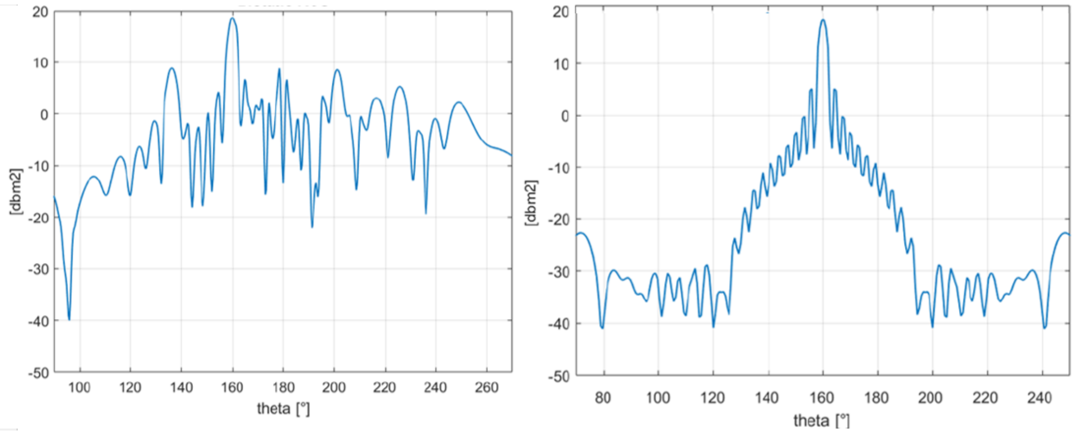

Figure 4.21: RCS in E-Plane (left), RCS in H Plane (right)

4.5 Double Parameter Structures

All the structures analyzed so far represent a good preliminary approach to implement the structure objective of this work. The general performances for the

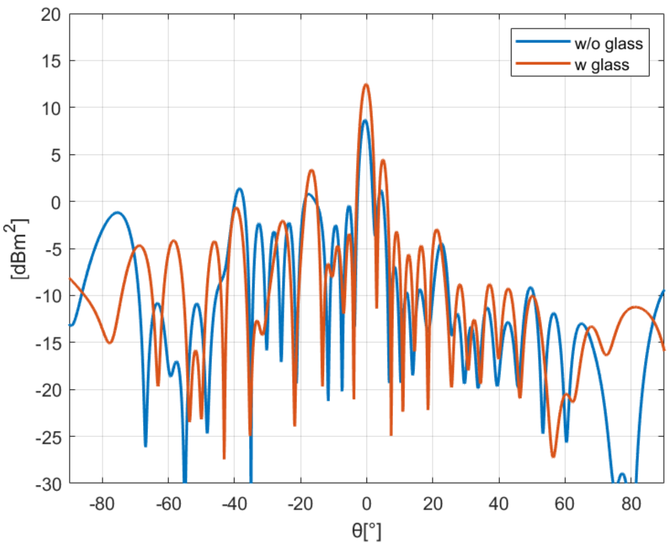

Figure 4.22: back lobes of SES w and w/o glass

proposed UCs and the simulated Bistatic RCS reports all good values and therefore they represent a good starting point. However, this is not sufficient to conclude that these represent a valid solution, because there are other parameters that need to be controlled to conclude this.

For example one of them is the already cited back lobe, that clearly is wanted to be as low as possible. When this happens means that only a lower part of the incoming field is reflected.

Considering the structure proposed so far, the back lobes are shown in Figure 4.23. The results indicate that the comparison between the main and back lobes are not so comfortable, especially in the case of holed and variable height structures, where on front of a main lobe lower than 19 dBm^2 a back lobe of around 12.5 dBm^2 is present. While in the glass-only case, the performance is a little better since the difference is higher (8.15 dBm^2 respect to 17.5 dBm^2). The front-to-back ratios which are obtained considering the previous SESs are:

- 6 dBm^2 for the Holed SES.
- 9.35 dBm^2 for the Glass-Only SES.
- 6.3 dBm^2 for the Variable Height SES.

The reason why this happens is mainly due to the behaviour of the transmission coefficient which does not have the best values and the effect of the glass on this was already explored. While for the glass-only structure it is better in

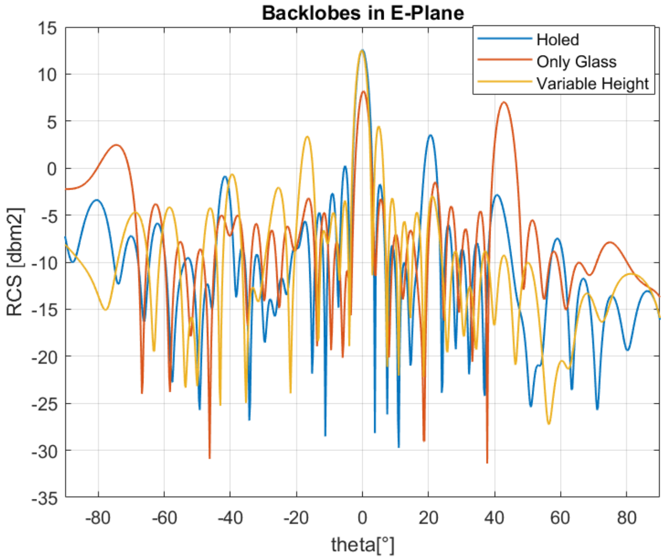

Figure 4.23: back lobe comparison within Holed, Glass-Only and Variable Height structures

the proposed range and it results in a lower undesired effect. For the just explained problem is therefore necessary to find a solution to improve the overall performance.

The idea implemented on this work to prevent high back lobe generations relies on the **double parametric analysis** mentioned at Section 3.5.

So basing on the first UC introduced at that section a SES will be now designed where an incoming plane wave at $(\theta_i, \phi_i) = (0°, 0°)$ is focused to $(\theta_b = 20°, \phi_b = 0°)$. The structure is created (Fig 4.24) with the usual parameters and the result for the radiation pattern is shown in Figure 4.25 and provides a maximum RCS of 19 dBm^2.

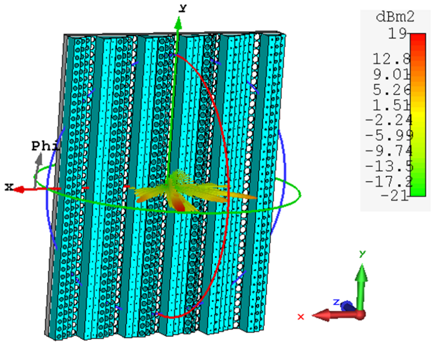

Figure 4.24: RCS 3D-view

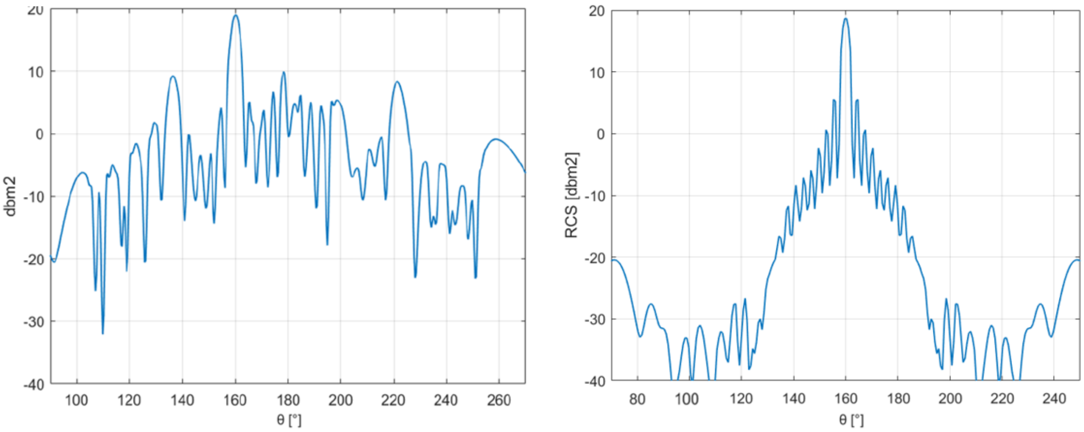

Figure 4.25: RCS in E-Plane (left), RCS in H Plane (right)

This value is higher but not so far from the previous one. However, what is now interesting is the back lobe view (Figure 4.26) in order to check if the proposed analysis works. The obtained RCS for the backlobe confirms the effectiveness of the double parameter analysis, where a maximum value of 10.5 dBm^2 is obtained with respect the 12.5 dBm^2 of the structure analysed so far (which is the same apart from the hole shape). This clearly doesn't correspond to the best reduction but is a very good starting point that can mitigate the problem but not totally solve it.

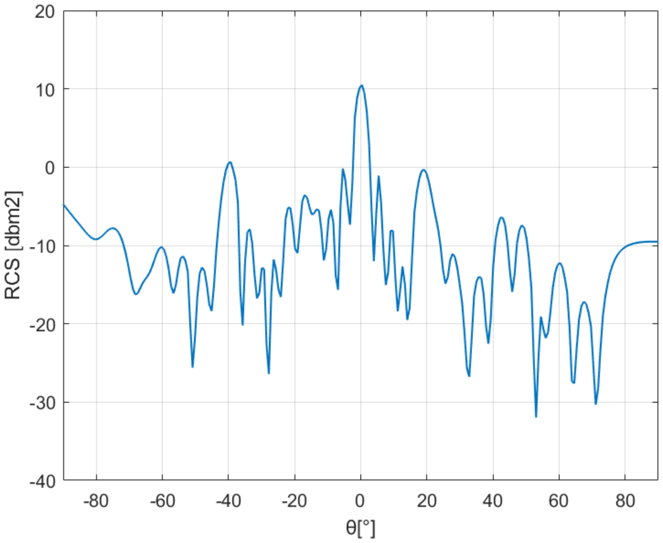

Figure 4.26: Back lobe of variable height + hole structure

Following instead the idea to subdivide the plastic pane for the reasons introduced in Section 3.5 and using the UC presented here, a TA could be now designed to see the improvements also in the entire structure. It has a diameter of 23

UCs, equal to $D = 12.78\,\text{cm}$ and it is discretized with 421 UCs. The feed is a circular horn located at a distance of $F = 11.50\,\text{cm}$ ($F/D = 0.9$) from the planar surface which impinges to the surface at $(\theta_i, \phi_i) = (0°, 0°)$ and is focused at ($\theta_b = 20°$,$\phi_b = 0°$). The angle between the line orthogonal to the TA and the field impinging on its center is 0° and is designed to focus the transmitted field in a direction characterized by $(\theta_{max}, \phi_{max}) = (0°, 0°)$. The phase map that the transmitarray must provide to satisfy these constraints is shown in Figure 4.27. Then the results of the simulated TA are shown in Figure 4.28.

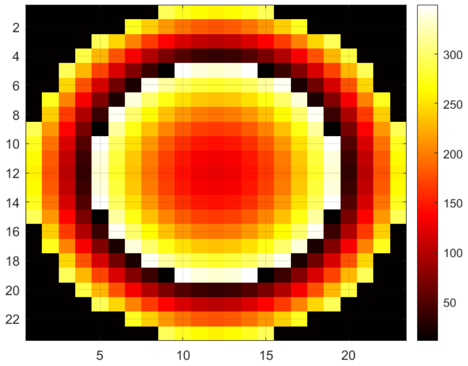

Figure 4.27: Phase Map

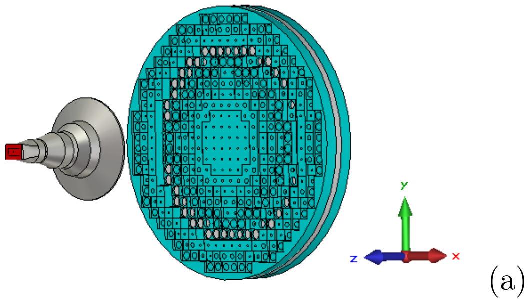

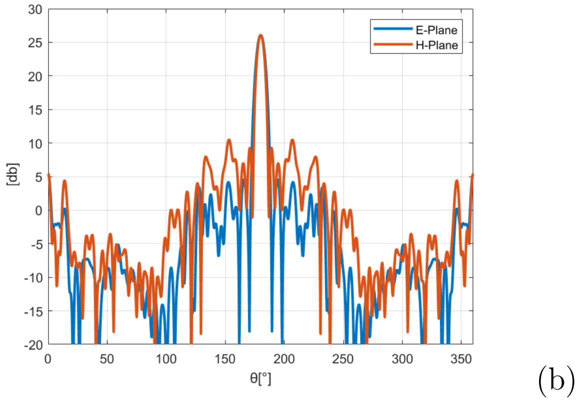

Figure 4.28: (a)Full TA structure (b) E-Plane and H-Plane Radiation Patterns

Then a SES is designed that will focus from the planar surface with always the same parameters which focuses an incident plane wave from $(\theta_i, \phi_i) = (0°, 0°)$ to $(\theta_b = 20°, \phi_b = 0°)$. So the layout and results are shown in Figure 4.29 where a peak in the main lobe of 18.6 dBm^2 is reported.

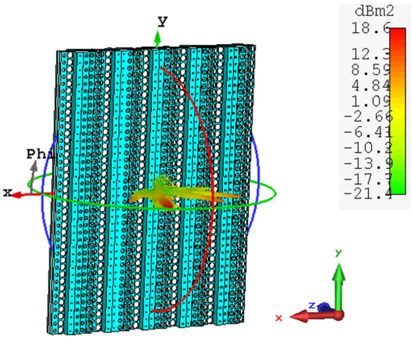

Figure 4.29: 3D RCS View

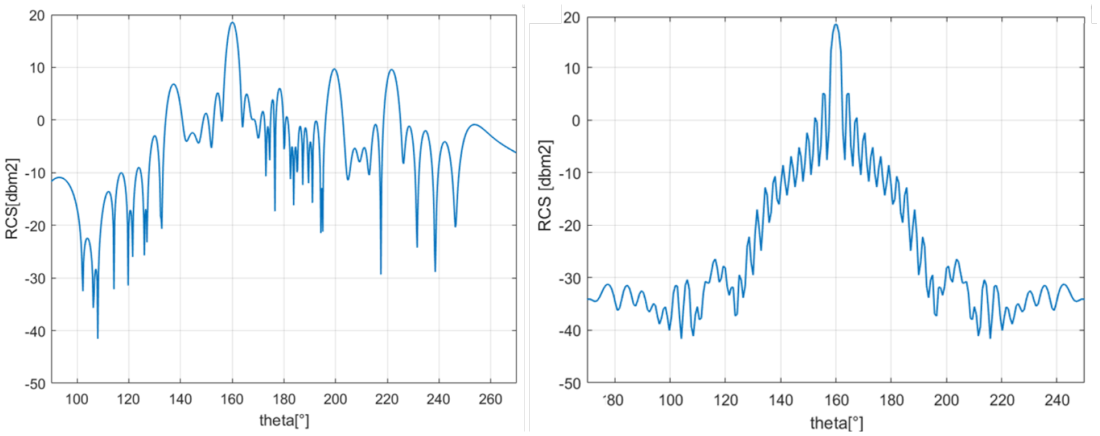

Figure 4.30: RCS in E-Plane (left) and H-Plane (right)

But what now require a particular attention is the back lobe, that finally now stands at a value of 5.6 dBm^2 representing a very important improvement to the previous structures. In Figure 4.31 could be compared to all those analysed in this section and as expected, reports that for this last structure (P-G-P) the best behavior is obtained.

If instead the UC is the last presented in Section 3.5, where two plastic blocks with different variable heights are considered, the results of the SES designed to focus the incident plane wave from$(\theta_i, \phi_i) = (0°, 0°)$ to $(\theta_b = 20°, \phi_b = 0°)$ based on this UC are shown in Figure 4.32 and 4.33. The back lobe stands again around to the same previous value, but the main lobe exhibits a reduction.

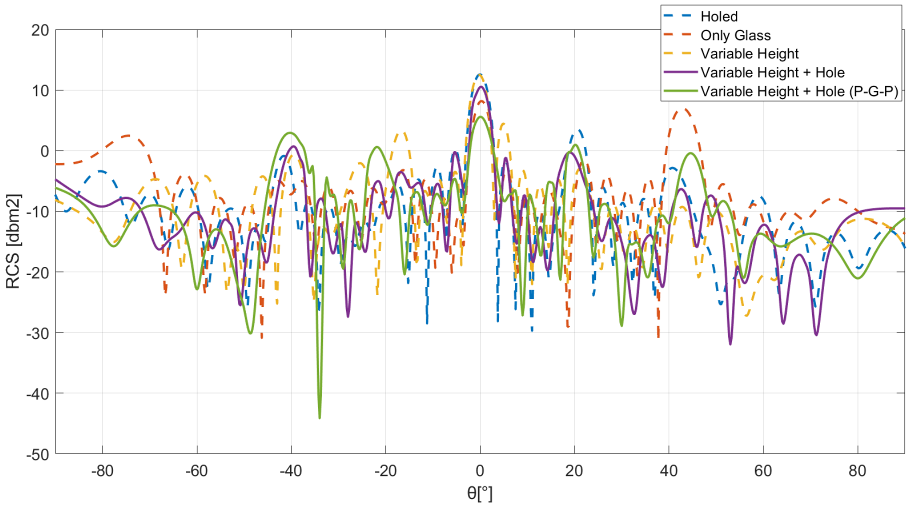

Figure 4.31: Back lobe comparison

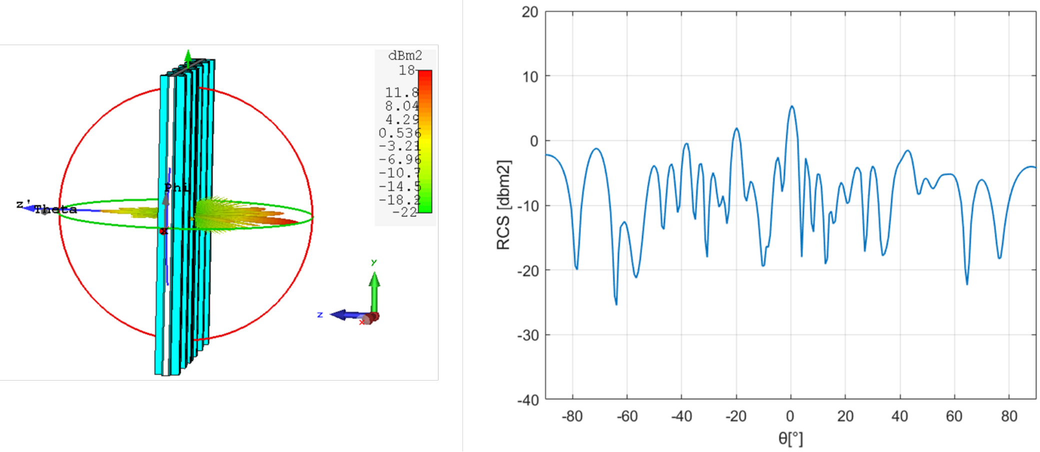

Figure 4.32: Variable Heights 3D RCS (left) and backlobe view in E-Plane (right)

So since the structure of Figure 4.29 seems to be the best, could be interesting go more in deep with its characterization and look what happens for a more realistic case in which the incoming beam arrive at a different incident angle. For example here is analysed where the plane wave impinges at ($\theta_i = -10°$,$\phi_i = 0°$) and is focused at ($\theta_b = 25°$,$\phi_b = 20°$). The structure simulated and the RCS obtained are reported at Figure 4.34 and 4.35.

As is possible to see the performances are again good also for a different incident angle. And to better characterize the proposed SES another RCS view could be provided, that is the **U-V plot**. In this type of plot the RCS is shown with respect to two new coordinates defined as in equation 4.2, that are **elevation**

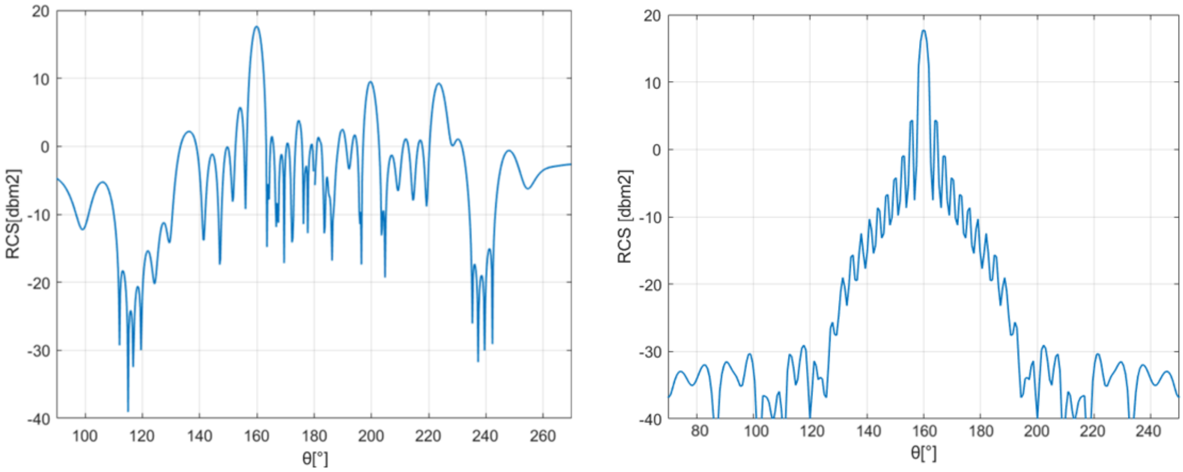

Figure 4.33: RCS in E-Plane (left) and H-Plane (right)

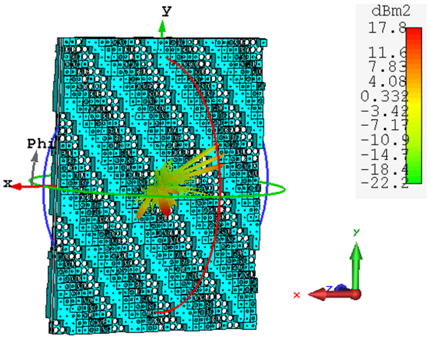

Figure 4.34: 3D RCS view for $\theta_i = -10°$

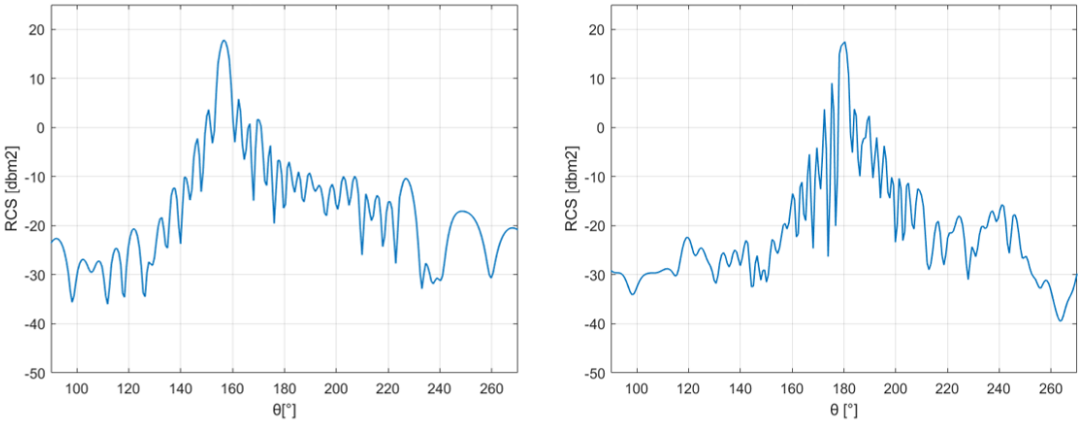

Figure 4.35: RCS in E-Plane (left) and H-Plane

angle (u) and **azimuth angle** (v).

$$u = sin\theta \cdot cos\phi \quad v = sin\theta \cdot sin\phi \tag{4.2}$$

The plot is presented in Figure 4.36 and from it is also possible to confirm the correctness of the main lobe position. But primarily, the aim for which could be helpful to look at it, is that in this way, on a 2-D view is possible to see the radiation of the SES and its behaviour for all directions.

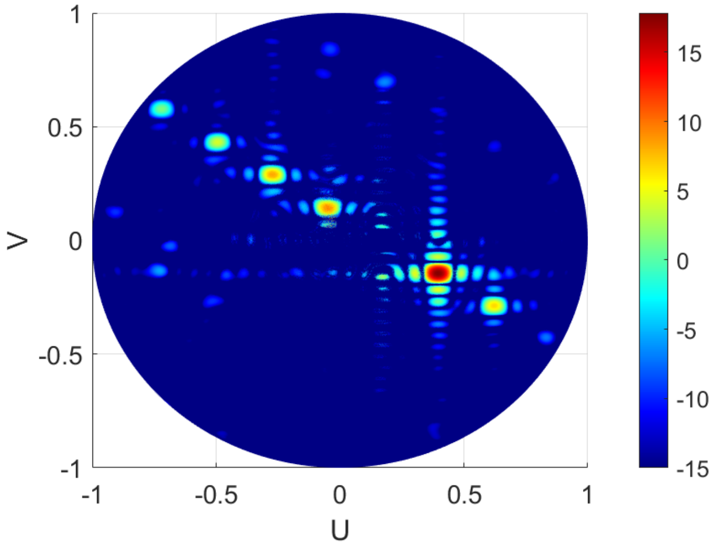

Figure 4.36: U-V plot

The final analysis about these surfaces just analysed consists in the **bandwidth (BW) evaluation**. Consider for example just the structure analysed with the double parameter analysis, the BW can be evaluated by looking at the Maximum RCS obtained not only at the design frequency, but in the band [25,30] GHz. These plots are given in Figure 4.37 and represent the maximum RCS variation of the structure made with a single plastic pane and the glass (1) (G-P VarH+Hole) analysed at the beginning of this sub-section and the surface made with plastic-glass-plastic with both only variable heights (2) (P-G-P H+H1) and the surface made with plastic-glass-plastic again with variable height and hole (3) (P-G-P VarH + hole).

The -1dB bandwidth provided are the following:

- 1.92 GHz for the (1).
- 2.47 GHz for the (2).
- 2.73 GHz for the (3).

That in percentage are respectively: 7 %, 9 % and 10.1 % confirming again that the structure (3) is that with the best performances obtained in this analysis.

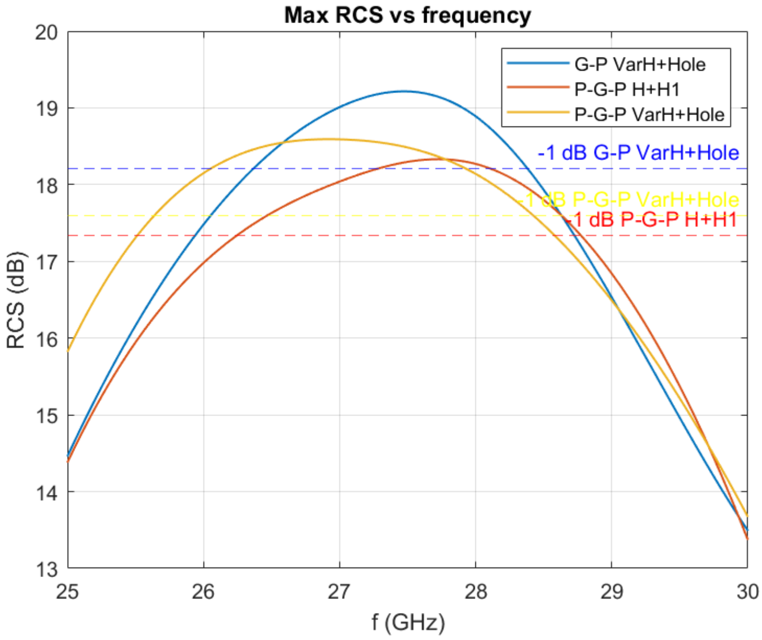

Figure 4.37: Bandwidth comparison for the proposed structures

According to the obtained BWs is possible to admit that the values achieved represent not the best values. Notice that here is reported the maximum RCS variation vs frequency, but an important consideration has to be taken. In fact, due to the phase range covered, which could appear an acceptable value, is far from 360°, the position of the maximum RCS is not always at $\theta = 160^\circ$ but will be subjected to little variation in position and this effect is more intense far from the design frequency. For example, for $f = 30\,\mathrm{GHz}$ the main lobe is located around $theta = 164^\circ$, while for the project frequency it is perfectly located at $theta = 160^\circ$. This means that the reported is not the maximum RCS, but the maximum RCS respect to the desired output beam position (160°).

The problem just underlined represent a limitation for the proposed dielectric-only UC, especially if the total structure is requested to be within a certain threshold for the total thickness. Indeed, the phase range could be enlarged just by increasing the UC thickness, but if the structure has to be mounted on a glass, the thickness cannot be so large.

Those proposed here are in the acceptable limit, since especially the first structure has 16 mm of plastic pane represents a thick structure, in which are the holes that helps to minimize the visual impact, that permits to the light passing through. While, the Plastic-Glass-Plastic structure reduces the thickness of individual panes, especially when the panes have variable heights and holes. The thickness of each pane is not fixed at 7 mm but can reach that value at most. So, in addition to the benefits for the reduced reflections, this structure also offers the best visual impact for the reasons mentioned earlier. This means it is necessary to find a compromise between phase range and total thickness, and for example, one of the future challenges and matter of research of this study could be the optimization of the UC for both thickness and phase range.

Chapter 5

Prototype Design

5.1 AM technique overview

The most efficient way to check if a designed EM surface really work apart from the simulation, is to manufacture its prototype and measure it, in this way is possible to do a further step, going from the simulation environment to the real world. The most popular technique today in doing that is by **3D-printing**, or better **additive manufacturing** (AM) technique. The aim of this paragraph is therefore to explore in what consists the AM, which are the the most commonly used techniques for printing an object and see what is present in literature about 3D-printed antennas.

In few words, the Additive Manufacturing is a group of techniques that allows to pass from digital data to a 3D object. Doing this is possible starting from a Computer-Aided Design (CAD) model (that represent the digital data) and creating the final structure depositing a material layer-by-layer by means of an automated process. This is also an explanation that helps to understand where the AM name comes from, since the combining of the material layer-by-layer is an additive process. This means the machine constructs the actual object step by step, stacking each layer on top of the one before it, until the final portion is complete. In doing that the starting digital data is divided into a sequence of two-dimensional (2D) cross-sections, each with a specific and finite thickness. These individual cross-sectional slices are then sent into 3D-printers, where they are manufactured together. Thanks to this technology, the geometry of the digital model is recreated with great fidelity in the real world, eliminating the need for the changes required by traditional manufacturing processes. According to these considerations, the AM machine functions can be seen as a "What You See Is

What You Build" (WYSIWYB) system, which means that the design digitally made is exactly what is got in the actual output [41].

Then, one of the main features which makes the AM an efficient technique and that introduced a revolution in the 3D-printing world, is its capability to deal also with structures composed by difficult shapes without spending so much time. This is indeed known as **freeform fabrication** and in other words tells that the time employed by the machine to do a complex structure is the same that spends in creating a simple cube of the same dimensions [41].

Now, since the AM was defined as techniques that allows to transform digital data in a 3D model, this cannot be done instantaneously but need several steps, therefore is necessary to take an overview about the steps that allows to create the final object. Eight are essentially the key points that allows to print an object and are also depicted in Figure 5.1:

1. **3D-CAD implementation**. The development of an object via AM technique is possible only after the object is digitally represented, in particular, the AM process starts with 3D CAD data, which can be created through various methods, including design software, automated optimization algorithms, or 3D scanning of existing parts. At the beginning this was a struggling part, because the CAD tools wasn't able to create perfect objects, where in the object many imperfections and gaps can be present that then were interpreted all in different ways by the machine. Now instead, a net increasing in CAD tools precision allows to strongly reduce these kind of problems.
2. **Conversion to STL**. The STL is the most common way to export a 3D object from a CAD tool and represent also the simplest way to describe an object only considering its geometry. This name derives by **Stereolithography** which was the first commercial AM technique and is simply based on dividing the object in several triangles that are able to approximate the object surface. And in order to obtain a good approximation, is necessary that the triangle sizes are less than the resolution of the machine, in this way, is ensured that no triangular shapes are visible in the final object.
3. **STL file transferring to AM machine and manipulation**. Once the STL file has been prepared and fixed, it may be uploaded to the AM machine. Before printing, is necessary to use visualization tools to check and do some changing to the file, for example resize if necessary. Not all AM machines can perform these functions, but software tools are available to

prepare STL files for printing. Most of the time, for the correct object building up, is necessary to create **supports** to hold it and can be set during this phase.

4. **AM machine setup**. Process that as the name suggests, consists in the setting of the AM machine parameter. It consists in setting parameters as layer thickness, building speed and options directly related to the material.
5. **Building**. While the previous part represents a manual part in which is the user that is allowed to set the parameters, after this, the following part is a computer-handled part. During these process there's the building of the structure by the layer-by-layer manufacturing process already mentioned.
6. **Platform Removal**. Operation that consists in the removing of the structure from the building platform. This is the first post-processing step and is very important because ensure a safe removal for the structure, because for example, during the previous step high temperatures can be achieved and therefore is necessary that the prototype will be cooled before being removed.
7. **Post-Processing Operations**. Post-processing is the final operation for the prototype creation, which usually requires some manual labor to finishing it. This can include simplest operations as just the removing of the support manufactured to hold the structure, or more particular operations as the application of specifics coating, or chemical treatments used to increase quality.
8. **Application**. The last step in which the object manufactured can be used for its application, if an antenna for example it could be measured.

After the crucial steps for AM are presented, is necessary to focus the attention in those who are the principal techniques that are employed in AM for the object creation. The American Society for Testing and Materials (ASTM) provides a standard about this techniques that is the F2792 [42]. According to ASTM the printing techniques can be classified into seven categories, who are:

- **Binder Jetting**.
- **Direct Energy Deposition**.
- **Material Jetting**.
- **Powder Bed Fusion**.

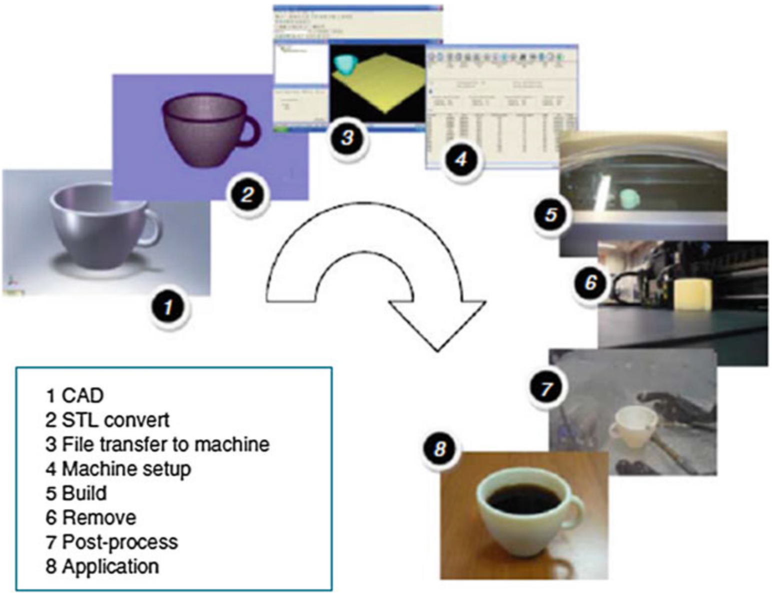

Figure 5.1: Graphical representation of the eight step in AM [41]

- **Sheet Lamination**.
- **Vat Photopolymerization**.
- **Material Extrusion**.

According to the standard the binder jetting technique is "an additive manufacturing process in which a liquid bonding agent is selectively deposited to join powder materials". This technique, that originally was called Three-Dimensional Printing (3DP) consists in depositing a binder material into a powder, layering them until the final object is manufactured. Then after the printing, the manufactured object (or parts) are left in the powder bed to solidify and will be cleaned and reinforced using infiltrants. The main advantages on this technique is that doesn't need of support structures because printed part is supported by the surrounding loose powder and that multiple parts can be printed at the same time. The main applications are plaster-based powders for visual prototypes, polymer powders for light-duty functional parts, and metal powders for functional prototypes or production [41].

The Direct Energy Deposition is instead "a process in which focused thermal energy is used to fuse materials by melting as they are being deposited", where "Focused thermal energy means that an energy source (e.g., laser, electron beam, or plasma arc) is focused to melt the materials being deposited". Directed Energy Deposition (DED) is an additive manufacturing process that creates parts by melting material as it's being deposited on a substrate and is primarily used for metals. In doing this a focusing heat source is used, as a laser or an electron beam to melt the raw material and creating the object layer-by-layer. Indeed, as the DED machine moves, each pass of the heat source creates a track of solidified material, and adjacent tracks form layers. Complex shapes can be manufactured either by using support structures or a multi-axis deposition head, which allows for movement in multiple directions, so it is especially used when is necessary deal with these complex shape. One of its main advantages consists in the ability to produce high-density parts with precise control [41].

The Material Jetting according to the F2792 "is an additive manufacturing process in which droplets of build material are selectively deposited". The Material Jetting (MJ) process is something very similar to a ink-jet printing, where materials are deposited layer-by-layer that applies droplets (small drops of material that are deposited by the print head) in a Continuous Stream (CS) or just On Demand (Drop On Demand, DOD)[40]. This kind of process exploit the UV light or heat to "cure" the material, means that after the material is deposited in tiny droplets by the print head, it is solidified or hardened using either ultraviolet (UV) light or heat. An implementation of multi-nozzle print heads can increase the speed and allow to deposit multi-material parts. While, for what concern the material used, the current MJ machines often use waxy polymers and acrylic photopolymers. Instead, for advantages and applications, the main advantages are high accuracy, minimal waste and high speed, while its principal application rely especially on prototyping, also for visual complex prototype due to the ability to print multi-material and colored parts.

Powder Bed Fusion is defined by the standard as: "an additive manufacturing process in which thermal energy selectively fuses regions of a powder bed". This is one the first commercialized manufacturing techniques that was developed at the Austin University in Texas. It includes the Selective Laser Sintering (SLS) that involves to fuse powder particles by means of a laser to build objects. To go more in detail, the machines used in doing that, who are the Laser Sintering machine, uses therefore the laser to melt plastic, metal or ceramic powders. The procedure consists in distributing and preheating the powder before employing a focused laser to fuse it into solid layers. During the construction process, loose powder serves as support for the part. After each layer is completed, the platform lowers and a new coating of powder is applied and when the item is finished, the build chamber cools to prevent warping, so the completed part can be removed and cleaned of superfluous powder. This technology is efficient and can produce precise, complicated pieces.

Sheet lamination is defined instead as: "additive manufacturing process in which sheets of material are bonded to form an object". This process consists in bonding several layers of material, that's typically paper with a thermoplastic coating, to create a part. This process is often associated with Laminated Object Manufacturing (LOM), one of the first commercialized additive manufacturing techniques, which uses a CO2 laser to cut each paper layer according to the CAD model. Some of the most important variants of sheet lamination are the adhesive bonding, thermal bonding, clamping and ultrasonic welding. In the firs one, the layers are positioned on the build platform, attached with an adhesive, cut to shape and at the end additional layers are added until the part is complete. The thermal bonding consists in cutting the sheets that will be bonded together exploiting heat. Clamping instead is used for metallic parts with simple shapes, since it is a cost-effective method that allows for disassembly and precise layer alignment. Ultrasonic consolidation is a combination of ultrasonic welding and CNC milling that uses force and vibration to stick together thin layers while keeping dimensional precision and surface polish and this approach, can also combine several materials or components. The main advantages that characterize sheet lamination are speed and low cost, but the finish quality can vary and often requires additional post-processing.

Vat Photopolymerization is defined by the standard as "additive manufacturing process in which liquid photopolymer in a vat is selectively cured by light-activated polymerization". Essentialy, the Vat Polymerization (VP) uses UV light to harden photosensitive materials via a chemical reaction known as photopolymerization. This includes layering a model in a vat of photopolymer resin. So, a UV light source is utilized to modify the resin in the appropriate pattern activating the photopolymerization, then the construction platform moves downward where the object is manufactured and once the sculpture is completed, the resin is drained and the final component is removed. Charles Hull developed this technology in the mid-1980s, which resulted in the invention of Stereolithography (SLA). SLA machines are commonly configured in one of two ways: Vector Scan, in which lasers scan the resin to cure it layer by layer, or Mask Projection, in which a bigger beam or digital projectors cure an entire layer at once, thus speeding up production. While VP provides great accuracy, fast processing, and vast build areas, it also has high costs and restricted material alternatives, but especially, Post-processing for VP-printed items can be time-consuming, as it requires the removal of excess resin and supports, as well as recurring in UV curing to ensure the part's quality [40].

Now the last process, since it is the most common on the market needs some more considerations. According to the ASTM standard the Material Extrusion (ME) is: "an additive manufacturing process in which material is selectively dispensed through a nozzle or orifice". The working principle is that the material used to create the part is first heated and melted inside a container, then it is discharged through a nozzle when pressure is exerted. The ejected material moves at a steady pace and maintains a consistent diameter if the applied pressure remains uniform. Upon exiting the nozzle, the material is in a semi-solid form, but it hardens within seconds. During this brief period, the material must fuse with the previously extruded section before solidifying. It is laid down according to a pre-established path, forming layer by layer. Then, an horizontal scanning while the flow of the material is controlled is performed and after this, the machine is vertically adjusted to build the following layer. The extrusion process can be handled in two different ways, one by exploiting temperature to control material's state, in this way the material is liquefied inside the reservoir, extruded ans solidified upon cooling. The other approach relies on chemical changes, for example by using a curing agent or also air exposure to solidify the material [41]. A typical AM machine is made up with two nozzles: one that is in charge of the material extrusion for the part creation and the other that can create the support, if needed [40]. All of the just mentioned considerations could become more clear by looking at Figure 5.2, where a typical AM machine for material extrusion is represented.

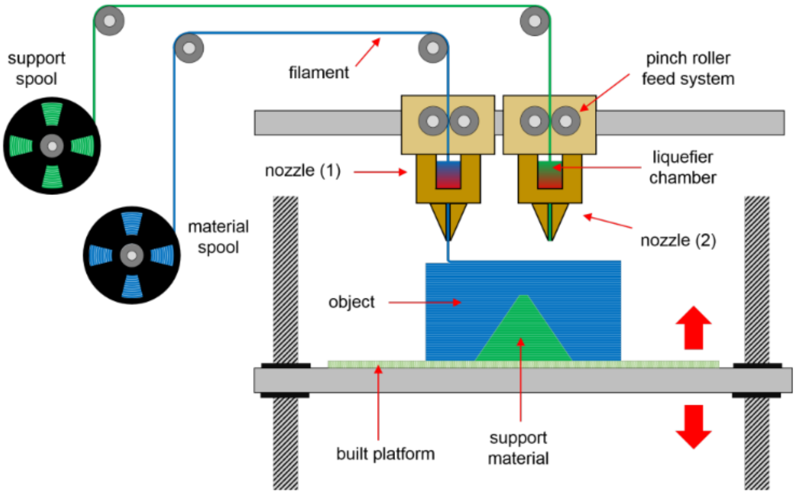

Figure 5.2: Typical AM machine schematic for material extrusion [40]

Once they have been introduced is necessary to go more in deep with the steps that composes ME process[41]:

- **Material Loading**. Extrusion-based systems require a chamber for material extrusion, ideally with a continuous supply of material, that serves as liquefaction point. And also a feed system that is typically composed of pinch rollers and their aim is to push the filament at the chamber with the necessary pressure to push the filament out of the nozzle.

- **Liquefaction**. The extrusion method works on the idea that the material inside the chamber is liquefied and then pushed through a nozzle. Heat is often delivered by heater coils arranged around the chamber and the liquefaction process is controlled by sensors with the aim to keep temperature constant. For some materials should be kept molten at the lowest feasible temperature to avoid deterioration or burning, which could leave residue and contaminate future melts. Additionally, higher chamber temperatures necessitate more cooling following extrusion.
- **Extrusion**. The operation which the material is taken out by nozzle, which determine the form and size of the filament. Having a large nozzle hole for extrusion will give a faster process but will reduce the resolution, indeed, the minimum part that the machine can print is determined by the nozzle diameter. No feature should be smaller than this diameter, and in reality, features should be greater than the nozzle diameter in order to be correctly replicated with sufficient strength. As a result, extrusion-based technologies are better suited to larger components with features and wall thicknesses that are at least twice the extrusion nozzle's nominal diameter. At the end, the material flow is regulated by the pressure difference between the chamber and the surrounding environment[40][41].
- **Solidification**. After the extrusion process, the material should keep its shape and size, but some effects as gravity, surface tension and cooling effects can cause changes. Some materials as gels may shrink and become porous during the drying and molten materials may be distorted. For this a good strategy to minimize distortion is to implement a gradual cooling process and always check the temperature difference between chamber and environment [41].
- **Positional Control**. To create vertical layers, an extrusion machine constructs a platform that moves along the vertical axis. The extrusion head will be horizontally moved on a plotting system that's made with two orthogonal linear drives, belt drives or lead screws, which must be powerful and responsive and allows a consistent material deposition and rapid direction changes. Taking care that direction changes cause inertia that affects material flow, that can potentially cause to excess deposition if not properly

adjusted. Therefore, to keep precision the part's outline is drawn slowly to ensure accurate material flow, while the internal filling is made faster.

- **Bonding**. To let bonding works, there needs to be enough residual heat to help the materials stick together. Or an alternative relies on filaments usage that contain a solvent or wetting agent for bonding with surrounding parts.
- **Support generation**. The support importance was already introduced in previous pages. Essentially, it is a temporary structure manufactured by the machine that support the printed object during its creation, preventing for example collapsing or deforming during layer buildings. There are two ways to build the support: of the same object material or of different material. The last is possible because, as already mentioned, usually AM machines are made with two nozzles and one is just for the support, while if the machine has a single nozzle, the support has to be of the same material. The advantage in have two nozzles is that the procedure will be faster and the nozzle used for the support can be made by a material easily to be removed at the end. Some tips for support making are the following: using different colours, especially when the structure is very complex this will help in its removal, using a weaker material that when the printing has finished can be easily removed or if isn't possible, at least using a material that could be easily removed by means of a solvent [40].

Now, the most common ME-based technology for AM is the so called **Fused Deposition Modelling** (FDM), invented by Stratasys in USA [43]. FDM uses a heating chamber to liquefy a polymer that is passed to the machine as a filament that is pushed into the chamber by a "tractor wheel" arrangement and is the pushing itself that creates the extrusion pressure. The main advantages in using FDM is the number of materials that can be used and the mechanical properties that characterize parts who are made using this technology, since objects made using FDM are one of the strongest that could be obtained for AM processes which involves usage of polymers. But as is possible to imagine, FDM is a trademark, therefore the general name of this technology is **Fused Filament Fabrication** (FFF) and was introduced by the members of the RepRap project to give a term that would not be restricted by legal limitations in its usage[40].

Before was mentioned as advantage the capability of FDM to deal with a large number of materials, they're **polymers** and their general properties were introduced at previous Chapter. So what is necessary now is to see the features of each of this polymers in view of AM technique and always in [40] they're well presented. First of all is necessary to introduce the **ABS**, since according to the [41], its "plus" version (ABSplus) was the most commonly used at the beginning (since it was developed for earlier FDM technologies). ABS is the acronym of Acrylonitrile Butadiene Styrene that is widely used in ME and injection molding processes, which presents good heat resistance and very good resistance to the impact.

Then, the **PLA**, PolyLactic Acid, one of the more sustainable polymers since it derives from renewable sources such as corn or sugar cane instead of petrol, indeed, is a biodegradable and bioactive thermoplastic aliphatic polyester. Thanks to its "green" properties, today is instead the PLA the most commonly used. In comparison to ABS, the PLA is easier to print and can achieve high details for the object. However, ABS has higher mechanical and thermal properties, since it is characterized by higher strength and resistance to temperature than the PLA.

Now, is the time to introduce the unique naturally transparent material, that is the **Polycarbonate** (PC). PC is a robust, translucent plastic polymer with high strength and impact resistance, characterised by its ability to tolerate high temperatures and resist UV radiation, making it appropriate for both indoor and outdoor use.

Nylon or PA, is another common synthetic polymer that can be melted into fibers or films. The Nylon present the highest mechanical strength respect all the other structure, but is characterized also by a good material memory, that represents its ability to return in initial position after being deformated.

Polyethylene Terephthalate (PET) is a widely used thermoplastic polymer that belongs to the polyesters. Also PET is characterized by its clarity and transparency (in its transparent version), apart of its durability and strength that are very good also here, it belongs to **recyclable** material, means that once it is no more used for its original purpose, it can be remodelled into another object.

Thermoplastic Elastomers/Thermoplastic Polyurethane. TPE and TPU are very flexible filaments made by mixing some polymers as plastic and rubber. Due to their high elasticity the filament used for AM, tends to buckle in the extruder causing a fail in printing.

All these are therefore the most commonly used materials for FDM technique and each of them got a researched feature for the work purpose, that consists in transparency. Each of these six materials can be bought by means of a transparent filament that therefore can be used to manufacture one of the previously proposed structure. To better introduce the prototype developed in this work, it may be helpful to review what is present in literature on 3D-printed antennas.

In [44] for example a dielectric-only reflectarray (RA) is developed with a UC made just with a squared-hole, where the hole is directly exploited to control the phase. Having a very similar situation with many of the structures proposed in the previous chapter. After the UC design an important phase occurs, that consists in re-design of the UC to be suitable for Additive Manufacturing. The UC has been simulated and is made by a UV-curable photopolymer produced by Stratasys with $\epsilon_r = 2.77$ and $tan(\delta) = 0.021$ and all the results are reported at Figure 5.3.

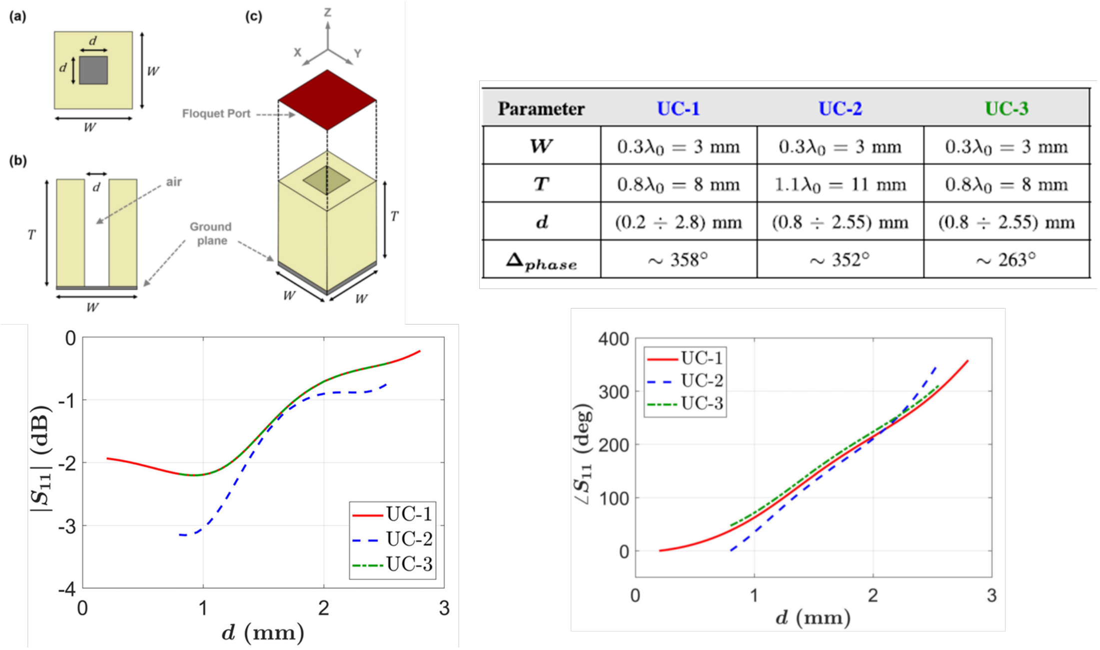

Parameter	UC-1	UC-2	UC-3
W	$0.3\lambda_0 = 3$ mm	$0.3\lambda_0 = 3$ mm	$0.3\lambda_0 = 3$ mm
T	$0.8\lambda_0 = 8$ mm	$1.1\lambda_0 = 11$ mm	$0.8\lambda_0 = 8$ mm
d	$(0.2 \div 2.8)$ mm	$(0.8 \div 2.55)$ mm	$(0.8 \div 2.55)$ mm
Δ_{phase}	$\sim 358°$	$\sim 352°$	$\sim 263°$

Figure 5.3: UC layout (top-left), UC configurations (top-right), Reflection coefficient module and phase (bottom) [44]

As is possible to see there are three proposed configurations for the UC. The UC-1 was the first designed in order to just control the phase, indeed a phase variation of 358° is obtained. But, in order to print this UC the range of the hole has to be reduced, in particular the minimum value has to be increased in order to avoid errors. To counteract to this reduction, the thickness will be increased to 11 mm to have almost the same coverage of before. Printing a 11 mm structure will take many times for the printing, therefore is necessary in UC-3 to return at the same thickness of UC-1 of 8 mm and the phase range is reduced to 263 mm. Now, the RA can be realized with 2704 elements arranged on a 52*52 elements matrix with a diameter of $15.6\lambda_0$ where $f_0 = 30\,\mathrm{GHz}$ and the horn is positioned at $F = 186\,\mathrm{mm}$.

Finally, the antenna prototype was manufactured using the Objet30 printer with **VeroWhitePlus** material from Stratasys. The prototype was printed in a single job lasting 4 hours and weighs approximately 200 g, during the printing also a support structure was made using PLA material. One of the main features in fabricating this antenna is the cost,indeed total cost of the antenna, including the manufacturing process, materials for the RA prototype, and support, was around 50 euros. Then, it was characterized in anechoic chamber and the results are shown in Figure 5.4.

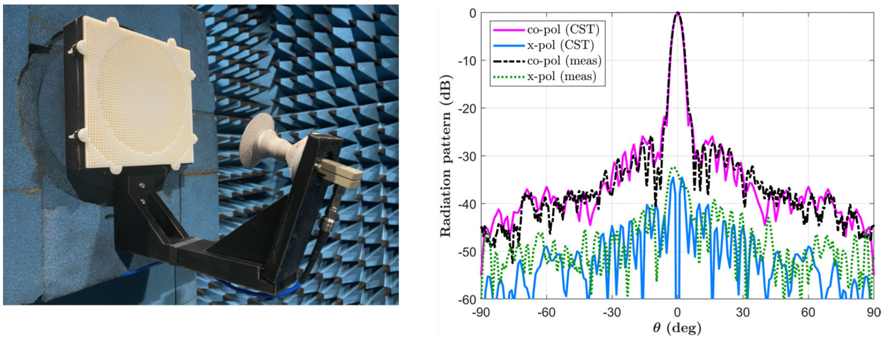

Figure 5.4: Prototype (left) and Results (right) [44]

The measured values obtained for both co-polar and cross-polar components agreed well with the simulated values. Indeed, the prototype has a gain of 30.8 dBi at 30 GHz, corresponding to an aperture efficiency of 39.6 %. The gain peaks at 31.3 dBi at 31 GHz, with an aperture efficiency of 44.4 %. The -1 dB gain bandwidth is 24.4 %, and the 3 dB gain bandwidth is 39.1 %.Values that now can finally be compared to the simulated results (23.9 % and 38.3 %).

Looking instead something done in TA technology, in [45] a beam-scanning Transmitarray that works in Ka-Band is first simulated and then printed using AM technique and then the experimental results are provided. The UC used for this is made by three layers of the same dielectric material: a central square hole layer and two tapered squared hole. This design, considering what is told at previous chapter about the fact that each medium is identified by its own characteristic impedance, allows indeed to have a lower difference within the consequent characteristic impedances, increasing the impedance matching. The layout can be seen at Figure 5.5.

The material was characterized electromagnetically using the **waveguide method**,

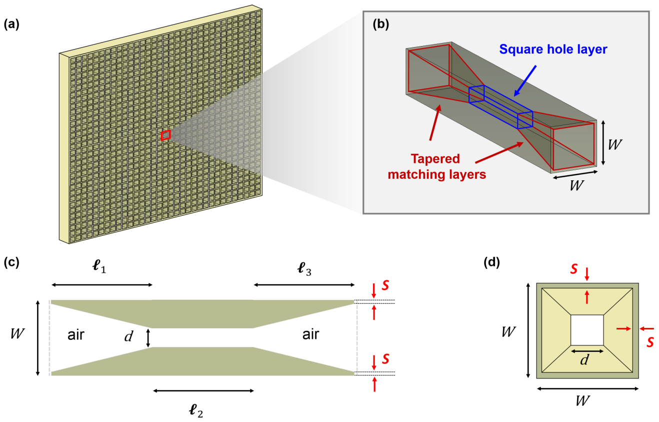

Figure 5.5: TA (a) and UC view (b), side UC view (c) and UC section (d) [45]

giving an average dielectric constant of $\varepsilon_r = 2.77$ and a loss tangent of $\tan\delta = 0.021$, that is the same of before. Considering now the manufacturing requirements and a parametric analysis, the side of the unit cell is fixed at $0.3\lambda_0 = 3\,\text{mm}$. The heights of each layer are $l_1 = l_2 = l_3 = 11\,\text{mm}$, resulting in a total cell thickness $T = l_1 + l_2 + l_3 = 3 \times 11\,\text{mm} = 33\,\text{mm} \approx 3.3\lambda_0$. The resolution of the 3D printer as before, take a limitation in maximum and minimum hole sizes, setting them 2.65 mm and 0.5 mm, respectively. This choice slightly affects the matching between the mid-layer's equivalent characteristic impedance and Z_0, reducing the amplitude of S_{21}, though a 360° phase range is still achieved. Then, the prototype is finally manufactured and a horn is positioned at $F = 150\,\text{mm}(F/D = 1)$ and the structure before simulated and then measured provides very good results, as shown in Figure 5.6. The prototype is fabricated using the 3D-printer Object30 by Stratasys which exploits PolyJet technology, exploiting again the Material Jetting AM technique.

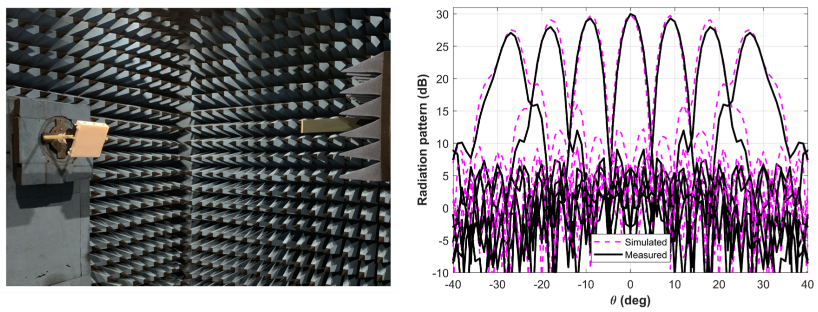

Figure 5.6: Prototype view in anechoic chamber (left) and simulated/measured results (right) [44]

They reports: in the considered range for θ_f, the gain exhibit a decrease lower than 3 dB, from a maximum of 29.97 dB at 0° to 27.07 dB for $\theta_f = \pm 30°$.

A more recent design is reported in [46], where a Transmitarray for mm-wave application is designed, then 3D printed and tested. The UC used for this purpose consists in an elliptical cylinder holed at two ends with a rectangular base and is shown at Figure 5.7 together with s_{21} amplitude and phase.

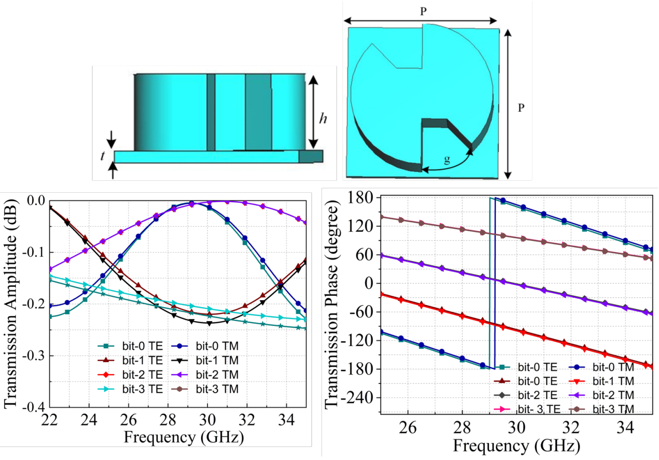

Figure 5.7: Transmission coefficient amplitude (left) and phase (right) and UC layout(top) [46]

Where the in the legend are reported the bits in which is discretized the phase, indeed, in order to reduce the UC design complexity, the obtained phase profile is discretized using 2-bit phase quantization. This means that all the phase values which belongs to a range will be expressed by just 2-bits and since here 2-bits are used the phase range is divided in 4 intervals each of them represented by 2 bits. The effect of the phase discretization allow to transform the phase map as reported in Figure 5.8. Therefore, the height of the elliptical cylinder, that is the variable dimension for the phase control, is 1.2 mm, 3.45 mm, 5.6 mm, and 7 mm, which correspond to the discretized phase states of 0°, 90°, 180°, and 270°, respectively.

Finally, the TA is designed and 3D printed with its own horn made with ABS ($\varepsilon_r = 2.2$) made of a diameter of $4.6\lambda_0$ ($f_0 = 30$ GHz) and then characterized in anechoic chamber, providing a 3 dB gain bandwidth of 33 % and a peak gain of 20 dBm^2 at the central frequency 30 GHz.

A last work could be presented and belongs to what is done in [47], where again a 3D printed Transmitarray Antenna is reported for mm-wave application. An-

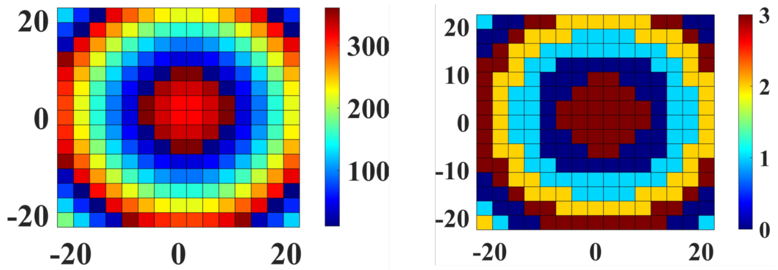

Figure 5.8: Phase map before(left) and after(right) discretization [46]

other reason for which it results very interesting is due to the UC shape, that's equal to some characterized in Chapter 3 and in particular is analysed in section 3.2. The mentioned cell, so called squared-hole, is reported here with results for Transmission coefficient amplitude and phase at Figure 5.9. The curves are obtained by let the diameter of the hole to vary between 0.1 mm and 4.9 mm. The size/periodicity is 5 mm and the total height is 20 mm, and the material has a dielectric constant (ε_r) of 2.65 and a loss tangent ($\tan\delta$) of 0.01, corresponding to ABS.

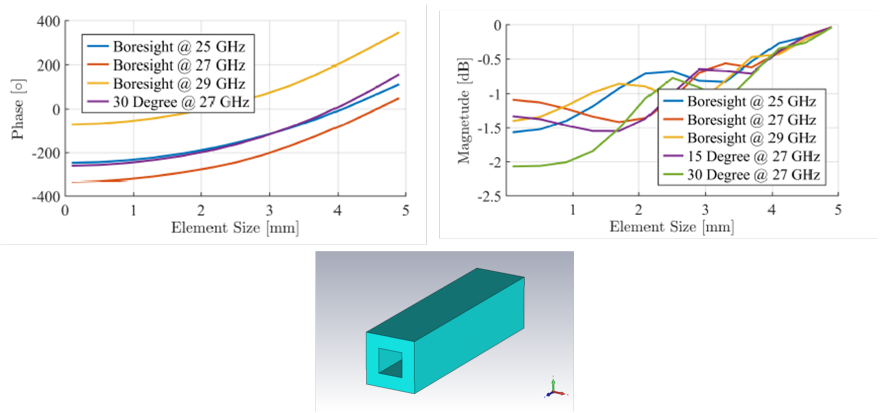

Figure 5.9: Transmission coefficient module (left) and phase (right) of squared hole UC [47]

After the evaluation of the required phase map, the TA is designed into a structure of 20x20 elements and with the feed positioned at 70 mm and simulated. Then, by means of a Raise3D Pro 2 printer that exploit the FDM technique [48] the structure is printed (Figure 5.10) and then measured, where results closely matched the simulations, showing an aperture efficiency of 45 % and gain of 26.6 dBi.

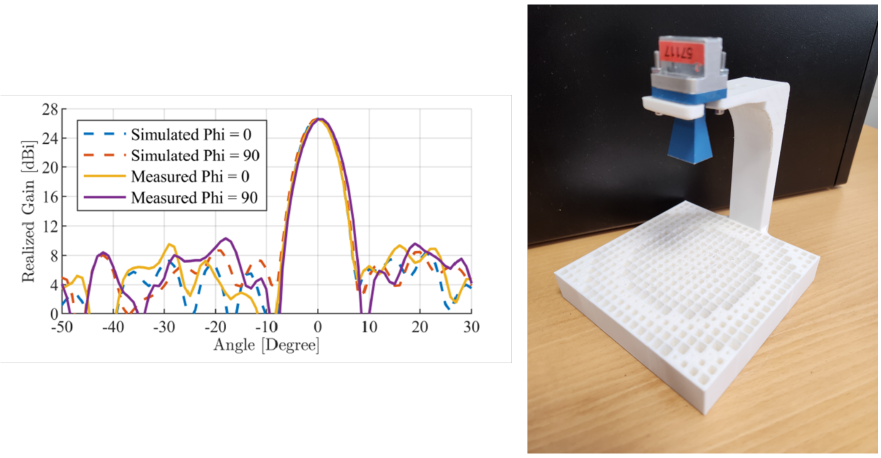

Figure 5.10: Simulated and Measured results (left) and prototype (right) [47]

5.2 PETG-based Prototype

Basing on all the considerations done, the next step is the practical manufacturing of a prototype with the AM technique. Due to the facilities present at Politecnico di Torino this Section rely on a Transmitarray design. Since until this moment a generic plastic is used for all the simulations, now is the moment to make a choice about it. At the beginning of the previous chapter an introduction about plastics and their electrical features was done and according to that a decision to represent the plastics used for the simulations with the values of $\epsilon_r = 2.7$ and $tan(\delta) = 0.01$ was taken. Considering also the transparency, which represent the other important constraint and following what is told about it on the previous paragraph, the PETG seems to be the perfect candidate, since it is popular for it clarity and transparency. Also the low-cost represent a key feature in the choice of this material, since a 1 kg filament can be bought approximately with 25€.

Now, before the physical manufacturing of the TA, is necessary introduce the possible structure which could be done. The first one is very similar to the first introduced on the paragraph 4.2 where Preliminary TA results are introduced and is made by a glass and a holed plastic pane. However, due to the better performances of the horn at 30 GHz, the frequency will be set to that value. The UC is the same of that introduced at Section 3.2 and reported at Figure 5.11, but now designed with:

- $f = 30\,\text{GHz}$
- $p = 5.2\,\text{mm}$

- $H = 14\,\mathrm{mm}$
- $H_v = 6\,\mathrm{mm}$
- $d = [0.8, 4.8]\mathrm{mm}$

The UC behaviour is reported at Figure 5.12 and what is noticeable is the limited phase range, that however, for this purpose also 250° could be sufficient.

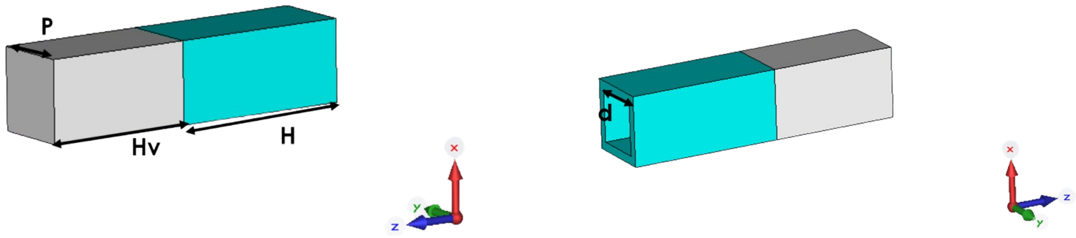

Figure 5.11: Transmission coefficient module (left) and phase (right)

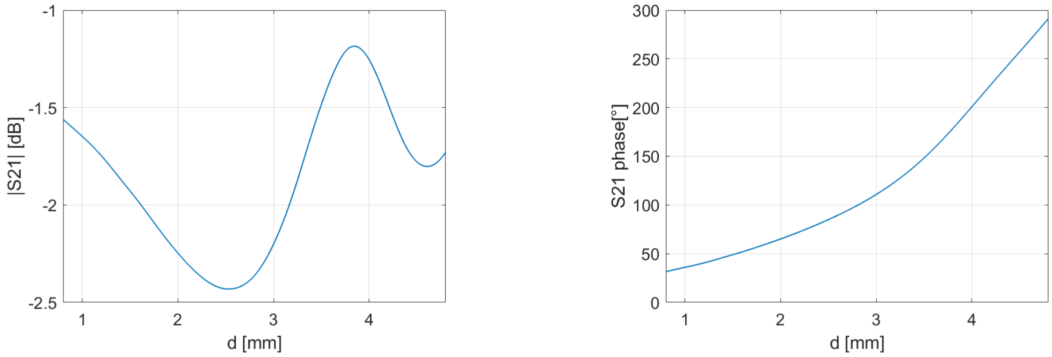

Figure 5.12: Transmission coefficient module (left) and phase (right)

The structure is then designed and its layout with the Gain 3D view in far-field (FF) are given at Figure 5.14, while the Cartesian plot is provided at Figure 5.15. According to the reported results, the structure present a maximum gain of 25.3 dB, that's not the best value and also, a huge contribute in the back side.

Considering now the potential in the P-G-P structure, could be interesting see what happens in implementing a TA that follows the same idea. So the UC is

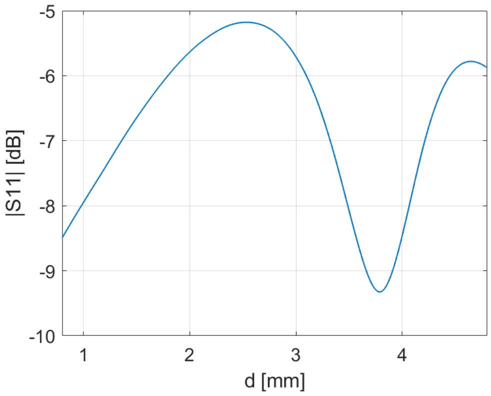

Figure 5.13: S_{11} Amplitude

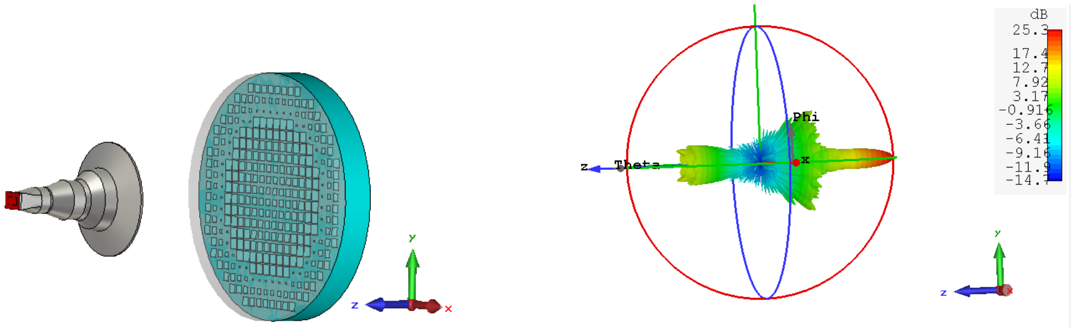

Figure 5.14: Structure Layout and 3D FF view

made as shown in Figure 5.16 where the PETG is divided into two 7 mm pieces and all the other values are kept the same, also the results of the S-curves are reported too. However, as it possible to see, the module here experiences a non-negligible reduction, while instead the phase stays almost the same. This effect will have a huge influence on the simulated TA (Figure 5.18) where here just an improvement on the maximum of the main lobe is reported (25.8 dB) in contrast of a worsening in the incidence side, where a huge back lobe is now obtained. This is an important demonstration of what was said in the previous chapter about the matching. Indeed, dividing in this way the structure allow to have more matching in the interface air-PETG and generally it should reduce reflections. However, it is not the only effect who has impact on reflections. Considering again the previous speech, it was said that every medium can be approximated as a Transmission Line that is described by its own characteristic impedance which carries information about the medium, but from TL theory is known that also the length of the TL affect the reflections, represented here by the thickness of the medium. And an effective approach to reduce multiple reflections is to fix that length to $\lambda_0/4$.

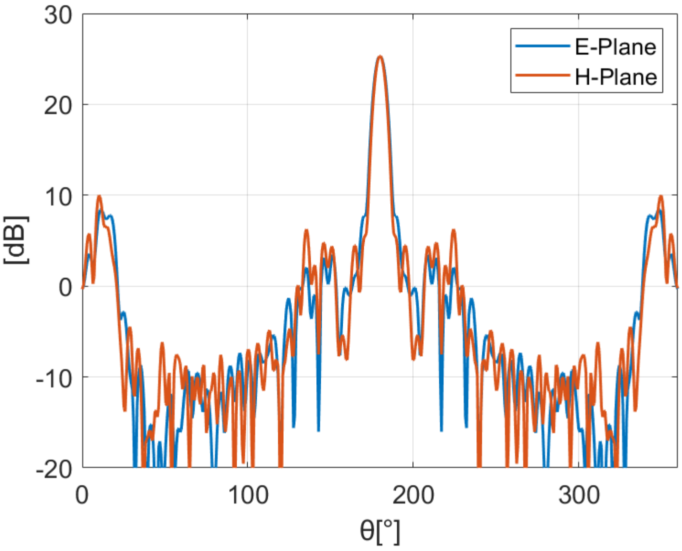

Figure 5.15: Gain in FF

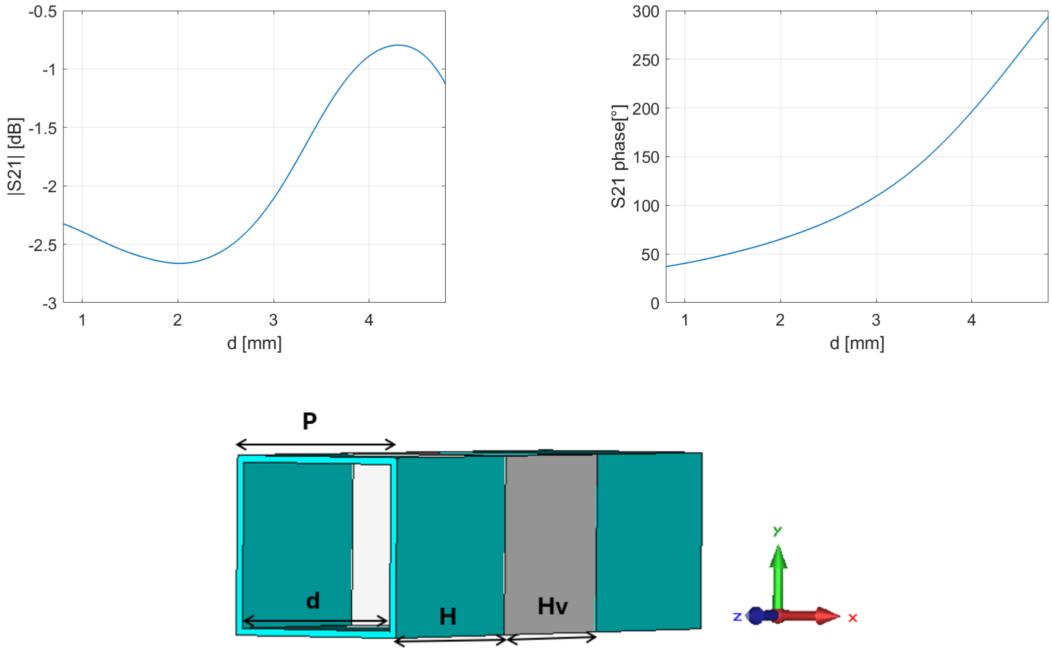

Figure 5.16: S_{21} Module and Phase of PETG-Glass-PETG UC (top) and UC-layout (bottom)

Just for theoretical purposes, a TA made by only PETG sheet will be simulated, where the UC is as that introduced at Fig. 3.4. The expectations are that it will clearly provide the best performance, due to the glass absence, that will substantially reduce the reflections. Indeed, this is confirmed by looking at Fig.

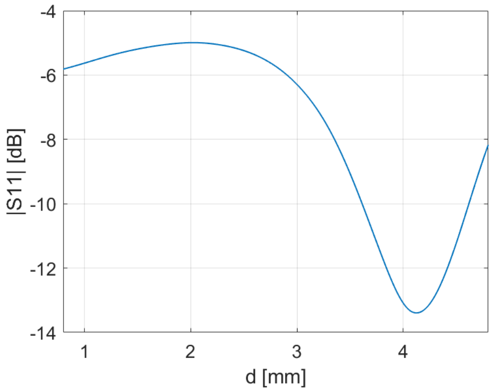

Figure 5.17: S_{11} Amplitude UC Fig. 5.16

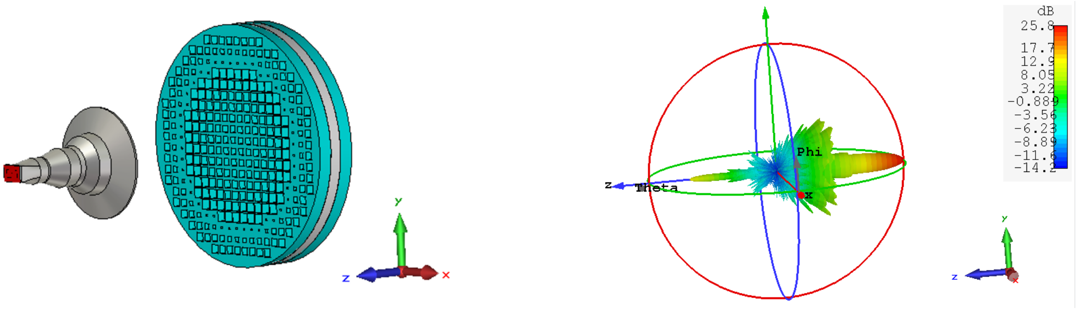

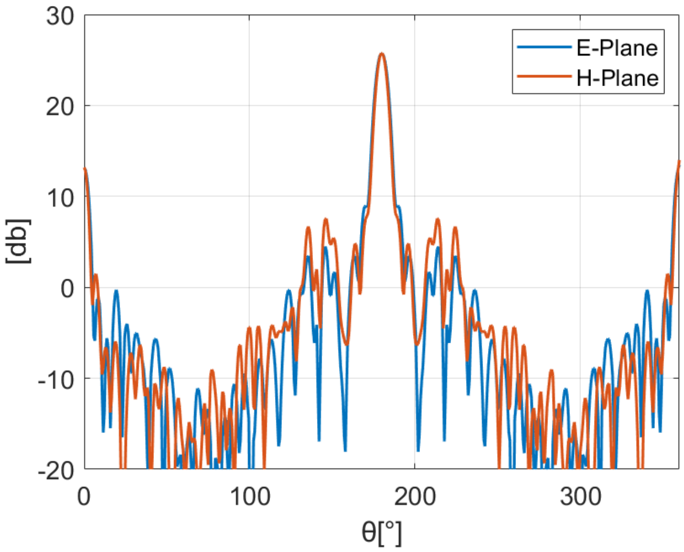

Figure 5.18: Structure P-G-P layout and gain 3D-view (top), Radiation pattern plot (bottom)

5.19 where the module and phase of the transmission coefficient are plotted and underline the improvements respect than before.

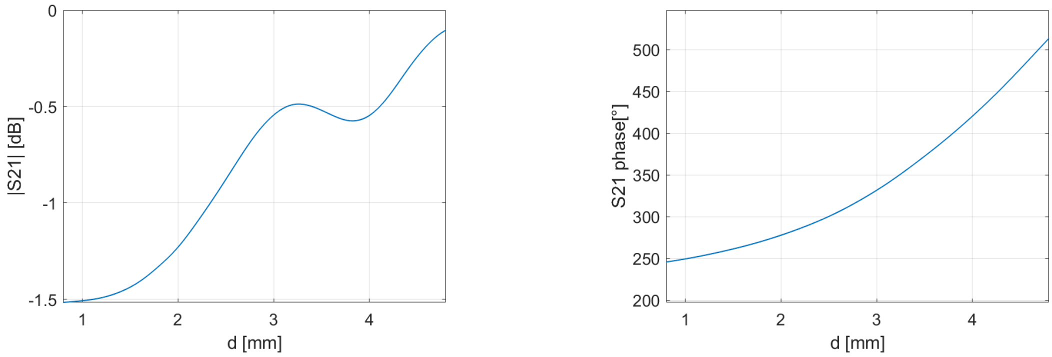

Figure 5.19: S_{21} Module and Phase of PETG-Only UC

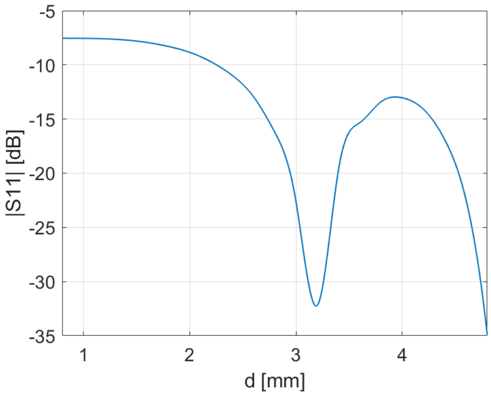

Figure 5.20: S_{11} Amplitude UC Fig. 5.19

Basing on this, a structure is implemented and its simulated Gain for both 3D-view and Cartesian view are illustrated at Figure 5.21. The results substantially confirm what was predicted in having a huge max gain (27.6 dB) and a very low contribute in the incidence side that is reflected.

Considering the just proposed TAs, now is the moment to deal with its manufacturing process, starting to the generation of the single PETG pane introduced at 5.21. The 3D printer used for this process is the **Raise 3D Pro3**, that's essentially a printer who exploits the AM technique of material extrusion and more precisely, the Fused Filament Fabrication (FFF, also known as FDM). The used filament is the CR-PETG bought from Creality Store.

The preliminary part for the printing consists in the **machine setup**. First of all, the considered 3D printer has 2 extruders, but since no support here is needed, only one will work, that clearly will be loaded with the PETG filament. Once the material is loaded the other preliminary part consists in the machine setup

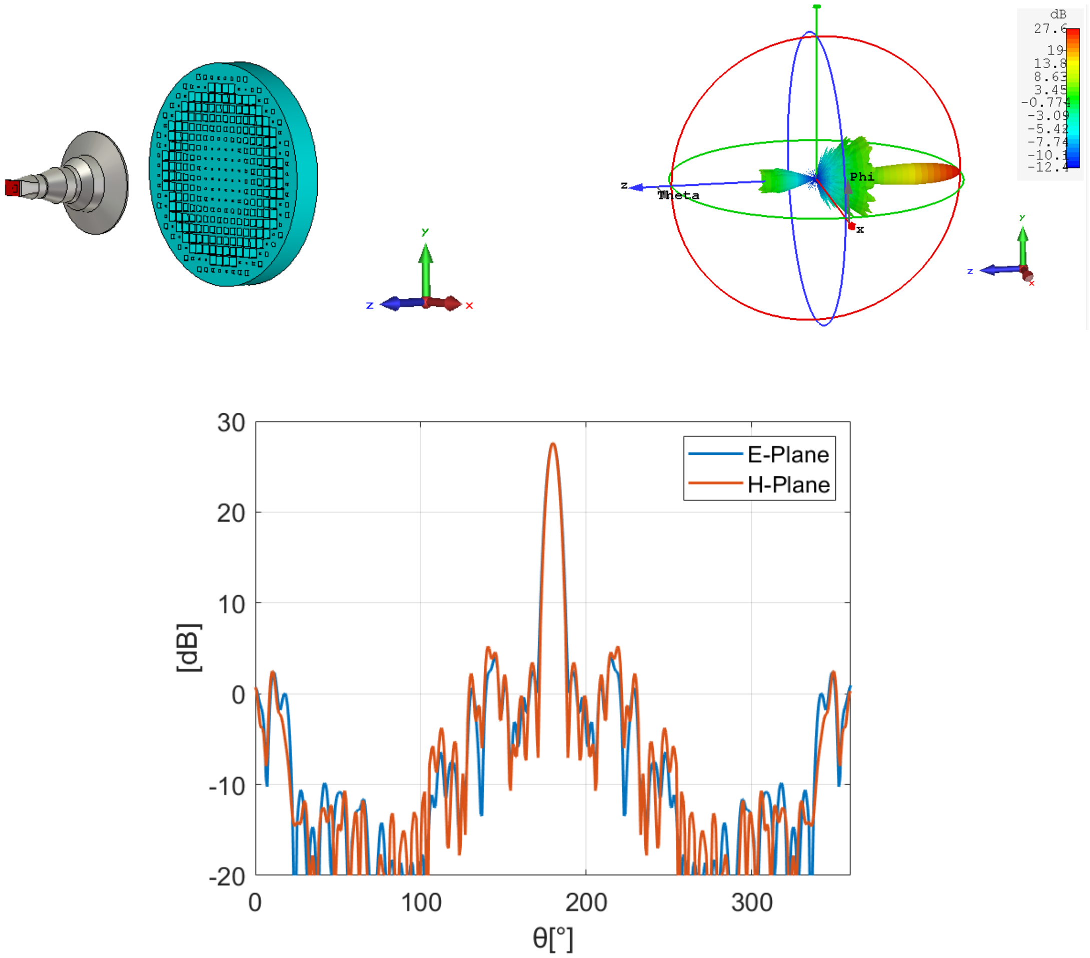

Figure 5.21: Structure Plastic-Only layout and gain 3D-view (top), Radiation pattern plot (bottom)

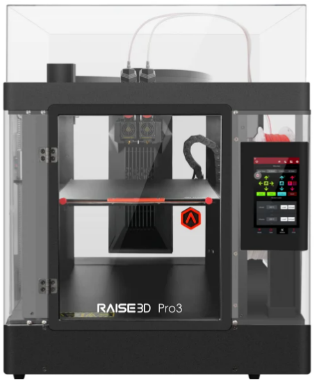

Figure 5.22: Raise 3D Pro3 (www.it.rs-online.com)

via **IdeaMaker** software, which is an interface from the user and the machine. The .stl project will be loaded into the program and at this point it will give the possibility to set the main options to correctly printing the structure. The main options are the following:

- **Layer height**. At the very beginning, the information about the single layer height is required. Since AM prints layer by layer, needs to be specified the height of each of them and for this application is set to 0.2 mm. Here there is also the possibility to set a different height for just the first layer, that could be helpful when the total height is not a multiple of the height resolution.
- **Extrusion width**. For more accurate results can be set to the minimum supported value of 0.4 mm. This is the reason why the hole diameter goes from 0.8 mm to a maximum of 4.8 mm. In particular the maximum is set in this way in order to have at least 0.4 mm to two adjacent holes.
- **Retraction speed**. It represents the speed in which the extruder has to come back avoiding the deposition of extra material.
- **Infill**. Expressed in percentage, represents the volume filling of the object. Here set to 100 %.
- **Support Generation**. The part that allows to generate the support and since here isn't required can be skipped.
- **Skirt**. It can be set to perform an **anchoring operation** for the structure borders, prevent them rising. Or for increase printing quality, some loops can be performed before the object printing starts. For the intended purpose no anchoring is necessary, while two loops of 3 mm each are done.
- **Temperature**. Finally is possible to set the temperature. First of all, the extruder temperature has to be set that is different for each material and here is fixed to 245°. Then, the internal temperature must to be correctly set avoiding any object deformation (here set on 60°).
- **Speed**. One of the key-parameter to be set to achieve a correct printing. Every material must be printed with different speed, because if for example the printing speed is lower than the required one, it will cause an unwanted extra-deposition of material or if for example is higher, the deposited material could be lower than the required. Particular attention needs the first layer, that usually is printed at lower speeds.

In order to test the feasibility of the TAs and test the properties of the material in printing, a good starting point could be the printing of the TA depicted in Figure 5.21 since it is composed by only plastic. So, after the exportation of the .stl file the printing process starts, setting the parameters on IdeaMaker as previously introduced. The printing process lasted 20 hours and the results of the Prototype are provided at figure 5.24.

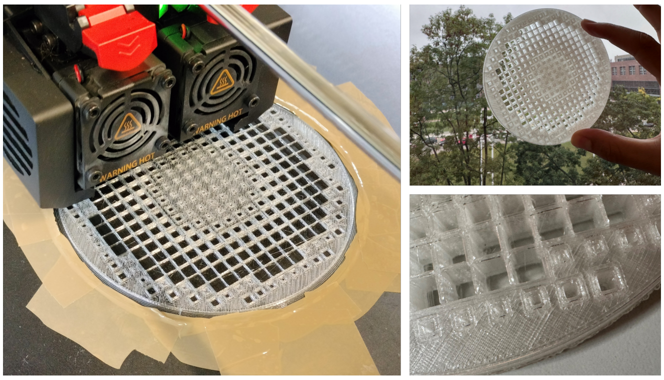

Figure 5.23: Prototype views

From the provided figures is immediately possible to see that despite the transparency ensured by the PETG, after the manufacturing process the prototype doesn't guarantee the expected transparency. Especially from the case in which is attached to the window is possible to see that where it is present, is very difficult to see what there is beyond the window.

So, here the experimental part had the aim to demonstrate that another way has to be taken for the prototype. Indeed, considering that, always from the Figure 5.24 is possible to see that the printing procedure seems to be one of the main limitation in doing this, due to the deposition of the material by the extruder that is performed at each layer by depositing the melted material by some diagonal lines and these last results to have a high visual impact.

For this reason a good starting point could be the implementation of a different AM technique. Just to confirm that it could be a reliable approach, a sample of resin is printed via a VAT photopolymerization showing a very improvement with respect to the PETG (Figure 5.24) and defining therefore, a new path that could be followed for future works.

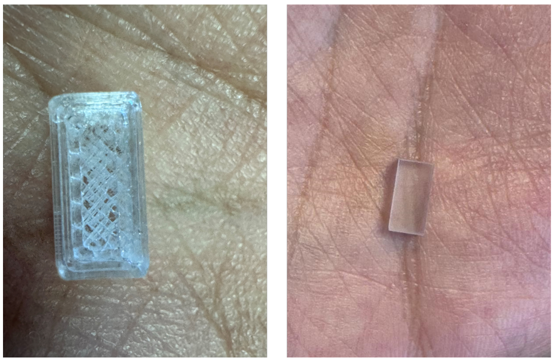

Figure 5.24: PETG sample printed via Material Extrusion (left) and Resin sample printed via Vat photopolymerization (right)

Conclusions

The work explores the possibility to increase the performances of last communication technologies, such as 5G and beyond, exploiting the introduction of a device as the Smart Electromagnetic Skin (SES). These are devices that operates in urban or also in industrial scenario, because generally are integrated into building's facade, that allows to increase the coverage inside their application environment, without increasing the number of base stations. SES are planar or curved surfaces discretized with a suitable number of Unit Cells (UCs) with resonant or sub-wavelength size, designed in such a way to provide anomalous reflection or transmission, thanks to which an incident field can be redirected in not Line of Sight (LoS) regions. The UC is described by the variation of one (or more) of its geometrical parameter, which provides the evolution of reflection coefficient and transmission coefficient vs the parameter itself. This thesis examines how the SES can be used to address a key-issue in these types of scenarios. In addition to the high propagation losses that are typical of this communication technology, signals also suffer from significant penetration losses that can be an issue for indoor users. Therefore, sometimes is convenient to establish an Outdoor-To-Indoor (O2I) link, that here is developed by an Optically-Transparent SES which works in transmitting mode that can be integrated into a window of a building's facade. In this way, the environment becomes a resource instead that an obstacle for the signal propagation and will be identified by a new definition, that is the Smart Electromagnetic Environment. The design is carried by an innovative approach that consists in a full-dielectric structure, deleting the metallizations that were already investigated in literature.

A preliminary approach consists in the overview of the SES design. This kind of devices derives from Transmitarray Antennas (TA) and therefore, the design procedure is very similar. At the beginning the definition of the Unit cell is necessary to determine the behaviour of the Transmission coefficient, then is necessary to determine the phase required by each cell to perform the wanted transmission and since at each of these values will correspond a value of the variable geometrical parameter of the UC, the entire structure will be created designing each cell with the parameter that provides that phase (or which generates the lowest error). The main difference consists in the type of the incoming field, that while in TAs is that of a feed located near to the structure, the one of the SES is that of a feed (Base Station) located far from the structure, that can be approximated as a plane wave.

The following step consists in the material selection and for its features in cost-effectiveness, transparency, electrical properties and its practicality to be manufactured, **plastics** seems to be the best candidates. According to this, several structures are implemented for the work purpose. So, starting from the UC a first idea consists in having a perforated plastic block mounted on a window 3.2, so thanks to its good response a SES is implemented and its ability to focus an incoming beam is demonstrated in Section 4.2. An interesting UC is also provided in 3.4, where with a simpler structure made by a variable height plastic block is analysed, also here providing promising results for the main lobe in 4.4. A glass-only structure is also implemented to explore the feasibility in perforating directly a window's glass pane leaving an un-holed part as protection from the holes to the external environment. The results demonstrate the effectiveness of the results, that are also promising in a restricted variation range of the geometrical parameter.

All the simulated results demonstrated the effectiveness of the just proposed structure for the main lobe contribute, however exhibit also huge back lobes contributes that is mainly due to the glass presence. So, a technique base on double parameter variation 3.5 in order to reduce the reflections is adopted. This allows the generation of surfaces for the transmission and reflection coefficients. Therefore by means of hierarchical procedure, is now possible, during the SES creation, to assign to the cell the geometrical parameter value that met the phase specification and simultaneously reduces the reflection coefficient. This procedure has adopted by a structure made by a circular-hole perforated unit cell, that shows a first important back lobe reduction in 4.5 respect to the previous one structures. A final solution always with the same technique, consists also in splitting the plastic block in two half, where one is now positioned before the glass. This allows to increase the matching between mediums, therefore giving another substantial reduction for the reflected contribute. Its feasibility also for different input wave angles is explored and its validity confirmed also in terms of bandwidth comparison.

The reliability of the proposed structures is also confirmed by the TA preliminary results, before in chapter 4 and then in chapter 5. Very important is this last, because a preliminary approach about the physical realization of a TA based on the proposed structures is investigated. After the Additive Manufacturing (AM) technique were explored, especially the Material Extrusion a transparent PETG filament was taken to create a first Prototype.

Further improvements for future works can be implemented to improve the proposed solutions. One of the main challenges could be trying to reduce the total structure thickness while keeping the same (or improving) performance in order to facilitate manufacturing procedure and reduce the visual impact. From a practical point of view, the usage of polymers of different natures used for the prototype (such as resin) that will guarantee an higher transparency could be investigated.

Bibliography

[1] Andrea Massa et al. “The Road to Smart Electromagnetic Environments: The Future of Wireless Communications”. In: *2022 IEEE International Symposium on Antennas and Propagation and USNC-URSI Radio Science Meeting (AP-S/URSI)*. 2022, pp. 1516–1517.

[2] Theodore S. Rappaport et al. “Millimeter Wave Mobile Communications for 5G Cellular: It Will Work!” In: *IEEE Access* 1 (2013), pp. 335–349.

[3] Ahmed H. Abdelrahman Fan Yang Atef Z. Elsherbeni Payam Nayeri. *Analysis and Design of Transmitarray Antennas*. 2017.

[4] Muhammad Muhammad et al. “Wideband Multi-layer Frequency Selective Surface Based Transmitarray Unit Cell for Satellite Communication Applications”. In: *2019 International Symposium on Antennas and Propagation (ISAP)*. 2019, pp. 1–3.

[5] Tao Yin et al. “Wideband High-Efficiency Transmitarray Antenna Using Compact Double-Layer Dual-Linearly Polarized Elements”. In: *IEEE Antennas and Wireless Propagation Letters* 22.10 (2023), pp. 2372–2376.

[6] P. Rezaei S. H. Ramazannia Tuloti and F. Tavakkol Hamedani. “High-Efficient Wideband Transmitarray Antenna”. In: *IEEE Antennas and Wireless Propagation Letters, vol. 17, no. 5, pp. 817-820* (2018).

[7] Guang Liu et al. “A Millimeter-Wave Multibeam Transparent Transmitarray Antenna at Ka-Band”. In: *IEEE Antennas and Wireless Propagation Letters* 18.4 (2019), pp. 631–635.

[8] Han Chang, Fei-Peng Lai, and Yen-Sheng Chen. “Transparent Transmitarray Antenna With Large Aperture for Significant Gain Enhancement in Millimeter-Wave 5G Communication Networks”. In: *IEEE Antennas and Wireless Propagation Letters* 23.2 (2024), pp. 663–667.

[9] *KLayout layout viewer and editor*. 2023.

[10] H. -P. Li T. -J. Li G. -M. Wang and H. -S. Hou. "Circularly Polarized Double-Folded Transmitarray Antenna Based on Receiver-Transmitter Metasurface". In: *IEEE Transactions on Antennas and Propagation* (2022).

[11] Xin Dai, Geng-Bo Wu, and Kwai-Man Luk. "A Wideband Low-Profile Reconfigurable Transmitarray Using Magnetoelectric Dipole Elements". In: *IEEE Transactions on Antennas and Propagation* 70.9 (2022), pp. 8008–8019.

[12] Kavitha Narayanasamy et al. "A comprehensive analysis on the state-of-the-art developments in reflectarray, transmitarray, and transmit-reflectarray antennas". In: *International Journal of RF and Microwave Computer-Aided Engineering* 30.9 (2020), e22272.

[13] Yu Xiao; Fan Yang; Shenheng Xu; Maokun Li; Kaiqiang Zhu; Houjun Sun. "Design and Implementation of a Wideband 1-Bit Transmitarray Based on a Yagi–Vivaldi Unit Cell". In: *IEEE Transactions on Antennas and Propagation, vol. 69, no. 7, pp. 4229-4234* (2021).

[14] Angelo Freni et al. "Low-Profile and Low-Visual Impact Smart Electromagnetic Curved Passive Skins for Enhancing Connectivity in Urban Scenarios". In: *Electronics* 12.21 (2023). ISSN: 2079-9292.

[15] Giacomo Oliveri et al. "Holographic Smart EM Skins for Advanced Beam Power Shaping in Next Generation Wireless Environments". In: *IEEE Journal on Multiscale and Multiphysics Computational Techniques* 6 (2021), pp. 171–182.

[16] Roberto Flamini et al. "Toward a Heterogeneous Smart Electromagnetic Environment for Millimeter-Wave Communications: An Industrial Viewpoint". In: *IEEE Transactions on Antennas and Propagation* 70.10 (2022), pp. 8898–8910.

[17] Giacomo Oliveri et al. "Holographic Smart EM Skins for Advanced Beam Power Shaping in Next Generation Wireless Environments". In: *IEEE Journal on Multiscale and Multiphysics Computational Techniques* 6 (2021), pp. 171–182.

[18] Paolo Rocca et al. "On the Design of Modular Reflecting EM Skins for Enhanced Urban Wireless Coverage". In: *IEEE Transactions on Antennas and Propagation* 70.10 (2022), pp. 8771–8784.

[19] Néstor J. Hernández Marcano, Hannes Bartle, and Rune Hylsberg Jacobsen. “Patch Antenna Arrays Beam Steering for Enhanced LEO Nanosatellite Communications”. In: *2020 IEEE Wireless Communications and Networking Conference (WCNC)*. 2020, pp. 1–6.

[20] *ANSYS HFSS software.*

[21] F. Zardi et al. “Design of Cost-Effective and Performant Electromagnetic Skins via Non-Radiating Sources”. In: *2023 IEEE International Symposium on Antennas and Propagation and USNC-URSI Radio Science Meeting (USNC-URSI)*. 2023, pp. 1413–1414.

[22] Francesco Zardi, Giacomo Oliveri, and Andrea Massa. “Design of EM Skins for Windowed Building Facades by Means of Non-Radiating Currents”. In: *2022 IEEE International Symposium on Antennas and Propagation and USNC-URSI Radio Science Meeting (AP-S/URSI)*. 2022, pp. 1866–1867.

[23] G. Oliveri et al. “On the Synthesis of Multi-Bit Reconfigurable Passive Skins for Smart EM Environments”. In: *IEEE Antennas and Wireless Propagation Letters* (2024), pp. 1–5.

[24] Junwen Tang et al. *Transmissive RIS for 6G Communications: Design, Prototyping, and Experimental Demonstrations*. 2022.

[25] Waqas Khalid et al. “Simultaneous Transmitting and Reflecting-Reconfigurable Intelligent Surface in 6G: Design Guidelines and Future Perspectives”. In: *IEEE Network* 37.5 (2023), pp. 173–181.

[26] Rana Sadaf Anwar, Lingfeng Mao, and Huansheng Ning. “Frequency Selective Surfaces: A Review”. In: *Applied Sciences* 8.9 (2018). ISSN: 2076-3417.

[27] Chen Xu et al. “Methods to improve 5G signal transmittance in modern buildings”. In: (Mar. 2024).

[28] Amirmasood Bagheri et al. “Enhancing 5G Propagation into Vehicles and Buildings using Optically Transparent and Polarisation Insensitive Metasurfaces over Wide-Incidence Angles”. In: (Jan. 2023).

[29] Giacomo Oliveri et al. “Optically-Transparent EM Skins for Outdoor-to-Indoor mm-Wave Wireless Communications”. In: *IEEE Access* 12 (2024), pp. 65178–65191.

[30] Seokyeon Hong, Yongwan Kim, and Jungsuek Oh. “Automobile Laminated Glass Window Embedded Transmitarray and Ray Tracing Validation for Enhanced 5G Connectivity”. In: *IEEE Transactions on Antennas and Propagation* 70.8 (2022), pp. 6671–6682.

[31] *CST Microwave Studio version:2015.00*. 2015.

[32] A.Zh. Khachatrian. “About the approximation of a field of an extended source by a sphere wave in the far illumination region”. In: *Results in Optics* 15 (2024), p. 100652. ISSN: 2666-9501.

[33] Tse-Tong Chia. “Prediction of electromagnetic scattering from metasurfaces”. In: *2016 10th European Conference on Antennas and Propagation (EuCAP)*. 2016, pp. 1–5.

[34] Fan Yang and Yahya Rahmat-Samii. *Surface electromagnetics: with applications in antenna, microwave, and optical engineering*. Cambridge University Press, 2019.

[35] *https://omnexus.specialchem.com*.

[36] Bartlomiej Salski et al. “Complex permittivity of common dielectrics in 20–110 GHz frequency range measured with a Fabry–Pérot open resonator”. In: *Applied Physics Letters* 119.5 (Aug. 2021), p. 052902.

[37] *https://passive-components.eu*.

[38] *https://arcodoubleglazing.com*.

[39] *www.efficientwindows.org*.

[40] Andrea Massaccesi. “Dielectric Transmitarray Antennas: from Design to Realization using Additive Manufacturing Technique”. PhD thesis. Politecnico di Torino, 2019.

[41] Ian Gibson et al. *Additive Manufacturing Technologies*. Nov. 2020. ISBN: 978-3-030-56127-7.

[42] ASTM ASTM. “F2792-12a: Standard Terminology for Additive Manufacturing Technologies”. In: *ASTM international* (2012).

[43] Stratasys. *Fused deposition modelling*.

[44] Andrea Massaccesi et al. “Three-Dimensional-Printed Wideband Perforated Dielectric-Only Reflectarray in Ka-Band”. In: *IEEE Transactions on Antennas and Propagation* 71.10 (2023), pp. 7848–7859.

[45] Andrea Massaccesi, Gianluca Dassano, and Paola Pirinoli. “Beam Scanning Capabilities of a 3D-Printed Perforated Dielectric Transmitarray”. In: *Electronics* 8.4 (2019). ISSN: 2079-9292.

[46] Gazali Bashir, Amit K. Singh, and Ankit Dubey. “A Wideband 3D Printed Digital Metasurface Transmitarray Antenna for mm-Wave Applications”. In: *2024 18th European Conference on Antennas and Propagation (EuCAP)*. 2024, pp. 1–5.

[47] Daniel E. Serup, Shuai Zhang, and Gert Frolund Pedersen. "Detailed Design Procedure for Low-Cost High-Efficiency 3D Printed Transmitarray Antennas for mm-wave Applications". In: *2024 18th European Conference on Antennas and Propagation (EuCAP)*. 2024, pp. 1–5.

[48] *Raise3D Pro 2*.

Appendix

A Matlab Code for TA Phase Map Evaluation and Research Algorithm

```
%Phase Map Evaluation
f=27e9;
lambda=3e8/f;
FonD=0.9;
p=0.5*lambda;
D=23*p;
F=D*FonD;
k=2*pi/lambda;

%number of element on the main axe
num_el=D/p;

%grid definition
[x y]=meshgrid(0:num_el,0:num_el);
x = (x(1:end, 1:end) + 0.5)*p;
y = (y(1:end, 1:end) + 0.5)*p;
cx=num_el*p/2;
cy=num_el*p/2;

d=sqrt((x - cx).^2 + (y - cy).^2); %distance from each
   element to the center

angt=deg2rad(0);
angf=deg2rad(0);
w=0; %counter for the number of element
for i=1:num_el
    for j=1:num_el
```

```
        if(d(i,j)<D/2)
            Ri(i,j)=sqrt(d(i,j)^2+F^2);
            psi(i,j)=rad2deg(k*(Ri(i,j)-sin(angt)*(x(i,j)*cos(angf)+y(i,j)*sin(angf))));
            psi(i,j)=mod(psi(i,j),360);
            w=w+1;
        else
            psi(i,j)=NaN;
        end
    end
end
figure()
imagesc(psi)
title('Element␣phases␣of␣s21␣with␣angled␣beam␣[Âř]')
grid on
axis on
colorbar
colormap(hot)

% Single element length

ampvhv6 = importfile('ampv(hv6).txt', 2, 24);
phvhv6 = importfile('phv(hv6).txt', 2, 24);

d=ampvhv6{:,"d"};
amp=ampvhv6{:,"Value"};
ph=phvhv6{:,"Value"};
ph(9:end)=ph(9:end)+360;

d_l=linspace(min(d),5,1000);
amp=spline(d,amp,d_l);
ph=spline(d,ph,d_l);

figure()
plot(d_l,amp, LineWidth=1)
grid on
title('s21␣module␣for␣UC␣width␣of␣16mm␣and␣Hv=6mm')
ylabel('|s21|␣[dB]')
xlabel('d␣[mm]')
xlim([0.5 5])

```

```
figure()
plot(d_l,ph,LineWidth=1)
grid on
title('s21␣phase␣for␣UC␣width␣of␣16mm␣and␣Hv=6mm')
ylabel('s21␣phase[Âř]')
xlabel('d␣[mm]')
xlim([0.5 5])

%Length map
%check max difference between near values
for i=1:length(ph)-1
    err(i)=abs(ph(i+1)-ph(i));
end
max_d=max(err);

err=zeros(1,length(d_l));
mat_len=zeros(23,23);
mat_ph=zeros(23,23);
mat_amp=zeros(23,23);
err1=zeros(23,23);
err2=zeros(23,23);
mat_err=zeros(23,23);
y_pstart=ph(1);
y_pend=ph(end);


for i=1:num_el
    for j=1:num_el
        phase_val=psi(i,j);
        if ~isnan(phase_val)
            if phase_val>=y_pstart && phase_val<=y_pend
                index=find(ph>phase_val-max_d/2 & ph<
                   phase_val+max_d/2);
                if isvector(index)
                    index = index(floor(length(index)/2) +
                       1);
                end
                mat_ph(i,j)=ph(index);
                mat_len(i,j)=d_l(index);
                mat_amp(i,j)=amp(index);
            else
```

```
                if phase_val<=y_pstart
                    err1(i,j)=abs(y_pstart-phase_val);
                    err2(i,j)=abs((phase_val+360)-y_pend);
                    if err1(i,j)<=err2(i,j)
                        mat_ph(i,j)=ph(1);
                        mat_len(i,j)=d_l(1);
                        mat_amp(i,j)=amp(1);
                    else
                        mat_ph(i,j)=ph(end)-360;
                        mat_len(i,j)=d_l(end);
                        mat_amp(i,j)=amp(end);
                    end
                end
                if phase_val>=y_pend
                    err2(i,j)=abs(y_pend-phase_val);
                    err1(i,j)=abs(y_pstart-(phase_val-360));
                    if err1(i,j)<=err2(i,j)
                        mat_ph(i,j)=ph(1);
                        mat_len(i,j)=d_l(1);
                        mat_amp(i,j)=amp(1);
                    else
                        mat_ph(i,j)=ph(end)-360;
                        mat_len(i,j)=d_l(end);
                        mat_amp(i,j)=amp(end);
                    end
                  end
            end
        else
            mat_len(i,j)=NaN;
            mat_ph(i,j)=NaN;
            mat_amp(i,j)=NaN;
        end
        end
end

figure()
pcolor(x,y,mat_len)
imagesc(mat_len)
grid on
axis on
title('Single␣element␣Length')
```

```
147 colorbar
148 
149 figure()
150 pcolor(x,y,mat_amp)
151 imagesc(mat_amp)
152 grid on
153 axis on
154 title('Single␣element␣amplitude')
155 colorbar
156 
157 % phase error map
158 mat_err=abs(mat_ph-psi);
159 figure()
160 h=imagesc(mat_err)
161 grid on
162 axis on
163 title('Phase␣error␣[Âř]')
164 colorbar
165 colormap(summer)
166 set(h, 'AlphaData', ~isnan(mat_err));
```

Listing 1: Research Algorithm from phase map to s_{21} phase curve

At the very beginning of the presented code the focus is the Phase map evaluation. Therefore is necessary to provide all the values that will be used in the first 8 code lines. In particular, since this code was used for TA developed in Section 4.2, here are reported its design parameters. After frequency and wavelength are introduced, the parameter F/D is set to 0.9, the diameter to $23 * p$, means that on the main axe 23 cell will be present and is 133.33 mm.

Then the grid in which the phase map will be inserted can be defined with the elements x and y specified at lines 15 and 16. Then the centre of the structure is evaluated in both x and y coordinate. At the end of this a grid is generated basing on the specified number of elements and every cell of the grid has a side equal to the cell periodicity.

Finally the distance from each element to the centre of the structure can be evaluated at line 20, that will essentially produce a matrix in which at the position (i, j) is reported the distance from the centre of the cell (i, j) to the transmitting part centre. After this all the element to evaluate the phase map are ready, therefore the direction of the scattered beam is specified at lines 22 and 23 and into a cycle is possible to implement the formula expressed in equation 2.3. Within this cycle, is first necessary to check if the cell under consideration is within the structure, just by checking if its distance to the center is lower than the radius of the entire structure. Then the distance from the horn to the cell has to be evaluated and then finally, the phase required by that cell is obtained after being scaled into the 0°-360° interval.

Once that the phase map is evaluated, the result will be as that in Figure 4.1 and the hearth of this research algorithm can be presented.

First of all the files that contains the points of the S_{21} module and phase curves (exported from CST) needs to be imported. Some post-processing operations are required, for example at line 53 there is the correction of the *phase jump* that is present on this specific case for the phase curve. The term 'phase jump' refers to a situation where two nearby points on a phase curve show a large difference in values, that from a graphically point of view means that the curve will be abruptly pulled down or pulled up. Therefore, to solve this, it is necessary, if the curve is pulled down, to take the point where this occurs and, starting from that point until the last value, add 360°, while if the curve is pulled up, 360° will be subtracted. Just to give a better idea to this, an example is reported in Figure 25.

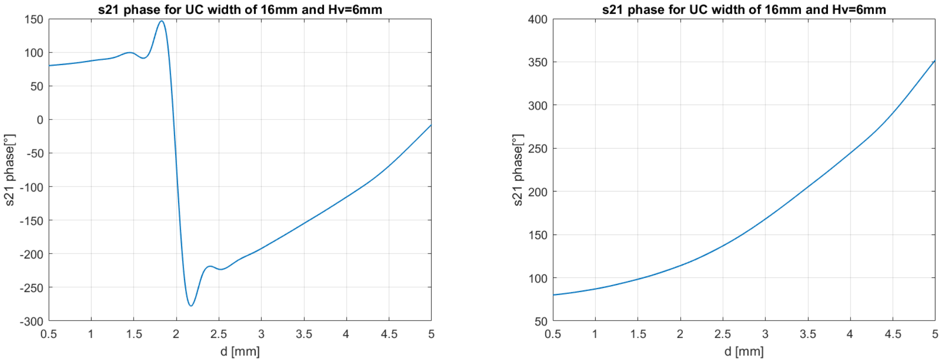

(a) (b)

Figure 25: example of s_{21} phase with phase jump before (a) and after correction (b)

The other post processing operation consists in increasing the sample density of the module and phase curves by *spline interpolation* on Matlab. Since only 24 points are evaluated on CST due to the larger computational time, the interpolation is implemented in order to let the curve be smoother, thanks to 1000 points now.

Another crucial step must be considered before the research algorithm implementation. It is important to determine the highest difference between two consecutive phase values, that is done on line 77 of the code.

This step is very important because it is extremely improbable that the exact phase value required by a cell, obtained in the phase map evaluation, will exactly match a value on the phase curve, even with 1000 interpolation points. Performing the calculation of the maximum difference between two consecutive points, that will be stored in a variable named max_d (as shown in line 80), is necessary because allows the research procedure to search a phase inside an interval of the phase curve defined by a width equal to max_d. Thank to this, is ensured that there will be at least one match within the specified interval.

Finally, after some matrix and vectors initialization at line 93 starts the algorithm. At the beginning, since during the phase map evaluation the grid cells who are out from the structure are set to 'NaN', is important to check if the current (i,j) value of the psi matrix in which all the phase map values are stored isn't NaN, otherwise this value will be set to NaN too.

At this point is necessary to check if the current value is within the phase curve, if this is true in a variable "index" will be stored the index of all the value that belongs to the interval explained just before, that therefore take into account the maximum difference between consequent values. But as told before, this will guarantee that at least one value is within this interval, but many times more than one value will be inside it and therefore as set in the next lines, the variable index will be a vector and the middle value (as approximation) will be selected. After this is necessary to store the results of this operation into three matrices.

- mat_{ph} will take the value of the curve assigned to the cells.
- mat_{len} the most important matrix, since it will have the abscissa value that correspond to the value stored in the previous matrix. The importance of this matrix is due to the fact that will be the matrix used to practically implement the structure.
- mat_{amp} the same thing done for the phase is repeated for the amplitude, therefore here is possible to find the amplitude values assigned to the cells.

Now, in line 106 starts to be considered the case in which the value that has to be searched in the curve isn't present.
Two cases can occur:

1. The value is lower than the minimum of the curve. Notice that in the

reported case it correspond to the starting value.

2. The value is higher than the maximum value of the curve. That here correspond to the last curve value.

In each condition, two errors will be defined: err_1 that evaluate the difference with the starting value and err_2 with the last value. Notice that a ±360° value is added or subtracted depending if the current phase value is in the case 1 or 2. For instance, if case 1 is satisfied, the phase error is first calculated relative to the starting value, and then, after adding 360°, it is recalculated relative to the final value. The smaller of the two phase errors will determine the selected value.

Finally, the hearth of the research algorithm is clear and at the end the map of the resulting length and of the amplitude will be provided with a map that will evaluate the phase error encountered during all the evaluations.

B DXF Generation File

B.1 Function dxfRectangle

```
function dxfRectangle(fid,Center,Width,Height)

X1 = Center(1) - Width/2;
X2 = Center(1) + Width/2;

 Y1 = Center(2) + Height/2;
 Y2 = Center(2) - Height/2;

fprintf(fid, '0\n');
fprintf(fid, 'SECTION\n');
fprintf(fid, '2\n');
fprintf(fid, 'HEADER\n');
fprintf(fid, '0\n');
fprintf(fid, 'ENDSEC\n');


fprintf(fid, '0\n');
fprintf(fid, 'SECTION\n');
fprintf(fid, '2\n');
fprintf(fid, 'ENTITIES\n');
fprintf(fid, '0\n');
```

```
fprintf(fid, ’SOLID\n’);
fprintf(fid, ’8\n’);
fprintf(fid, ’0\n’);

 % Write vertex (X1,Y1)
 fprintf(fid, ’10\n’);
 fprintf(fid, ’%f\n’,X1);
 fprintf(fid, ’20\n’);
 fprintf(fid, ’%f\n’,Y1);
 fprintf(fid, ’30\n’);
 fprintf(fid, ’0.0\n’);

 % Write vertex (X1,Y2)
 fprintf(fid, ’11\n’);
 fprintf(fid, ’%f\n’,X1);
 fprintf(fid, ’21\n’);
 fprintf(fid, ’%f\n’,Y2);
 fprintf(fid, ’31\n’);
 fprintf(fid, ’0.0\n’);

 % Write vertex (X2,Y1)
 fprintf(fid, ’12\n’);
 fprintf(fid, ’%f\n’,X2);
 fprintf(fid, ’22\n’);
 fprintf(fid, ’%f\n’,Y1);
 fprintf(fid, ’32\n’);
 fprintf(fid, ’0.0\n’);

 % Write vertex (X2,Y2)
 fprintf(fid, ’13\n’);
 fprintf(fid, ’%f\n’,X2);
 fprintf(fid, ’23\n’);
 fprintf(fid, ’%f\n’,Y2);
 fprintf(fid, ’33\n’);
 fprintf(fid, ’0.0\n’);

 fprintf(fid, ’0\n’);
 fprintf(fid, ’EOF\n’);


end
```

Listing 2: Function used to create a rectangle .dxf

The current function generate a dxf file that represent a rectangle as a bi-dimensional object. It receives four input parameters:

- *fid* is the identifier of the file in which the dxf will be written.
- *Center* is the center of the current rectangle.
- *Width* is the rectangle width.
- *Height* is the rectangle height.

At the first lines of the code is necessary to define the Header and the solid entities. Then, the rectangle is written vertex per vertex, where x_1 and x_2 are respectively left and right edges of horizontal coordinates and y_1 and y_2 upper and lower edges of the height, as illustrated in Figure:26

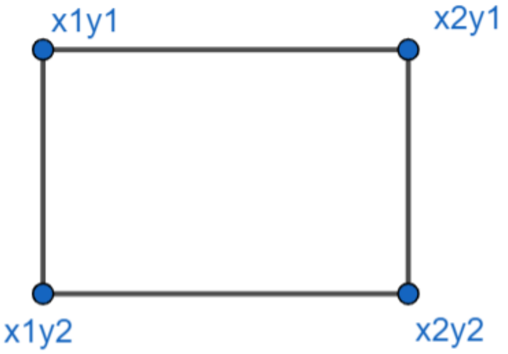

Figure 26: Rectangle written in the .dxf file

B.2 dxf File Creation

```

fid = fopen('file.dxf', 'wt');
len = load('-mat', 'mat_len');
mat_len=len.mat_len;

f=27e9;
lambda=3e8/f;
p=0.5*lambda*1e3;
[Nx,Ny]=size(mat_len);

```

```
for i = 1:Nx
    for j = 1:Ny
        if ~isnan(mat_len(i,j))
            X = (i-1/2-Nx/2)*p;  % Center X
            Y= (j-1/2-Ny/2)*p;  % Center Y
            l=mat_len(i,j);
            dxfRectangle(fid,[X Y],l,l)
        else
            X=NaN;
            Y=NaN;
            l=NaN;
            dxfRectangle(fid,[X Y],l,l)

        end
    end
end

fclose(fid);
```

Listing 3: Function that generates the .dxf file

So, after dxfRectangle was presented, here there's the code to generate the file for CST.
At the beginning is open in writing mode the file and is imported the matrix mat_{len} cited in A, then all the necessary parameters as frequency, wavelength and periodicity are set.

A cycle will evaluate the centers of each cell in both coordinates x and y, that clearly are inside the structure, and will be multiplied for the cell periodicity in such a way to be consistent with structure dimensions. Then the side of the hole will be taken by the matrix mat_{len} and the rectangle (or square) will be generated thanks to the previous function.

Notice that here width and height passed to the function are the same, since the aim is to create a square.

B.3 .dxf file generation for Variable Height Structure

```
function dxfRectangle(fid,Center,Side,Depth)

```

```
X1 = Center(1) - Side/2;
X2 = Center(1) + Side/2;

 Y1 = Center(2) + Side/2;
 Y2 = Center(2) - Side/2;

fprintf(fid, '0\n');
fprintf(fid, 'SECTION\n');
fprintf(fid, '2\n');
fprintf(fid, 'HEADER\n');
fprintf(fid, '0\n');
fprintf(fid, 'ENDSEC\n');


fprintf(fid, '0\n');
fprintf(fid, 'SECTION\n');
fprintf(fid, '2\n');
fprintf(fid, 'ENTITIES\n');
fprintf(fid, '0\n');
fprintf(fid, 'SOLID\n');
fprintf(fid, '8\n');
fprintf(fid, '0\n');

 % Write vertex (X1,Y1)
 fprintf(fid, '10\n');
 fprintf(fid, '%f\n',X1);
 fprintf(fid, '20\n');
 fprintf(fid, '%f\n',Y1);
 fprintf(fid, '30\n');
 fprintf(fid, '%f\n',Depth);

 % Write vertex (X1,Y2)
 fprintf(fid, '11\n');
 fprintf(fid, '%f\n',X1);
 fprintf(fid, '21\n');
 fprintf(fid, '%f\n',Y2);
 fprintf(fid, '31\n');
 fprintf(fid, '%f\n',Depth);

 % Write vertex (X2,Y1)
 fprintf(fid, '12\n');
```

```
 fprintf(fid, '%f\n',X2);
 fprintf(fid, '22\n');
 fprintf(fid, '%f\n',Y1);
 fprintf(fid, '32\n');
 fprintf(fid, '%f\n',Depth);

 % Write vertex (X2,Y2)
 fprintf(fid, '13\n');
 fprintf(fid, '%f\n',X2);
 fprintf(fid, '23\n');
 fprintf(fid, '%f\n',Y2);
 fprintf(fid, '33\n');
 fprintf(fid, '%f\n',Depth);

 fprintf(fid, '0\n');
 fprintf(fid, 'EOF\n');


end
```

Listing 4: Rectangle generation for Variable Height .dxf file generation

The reported code aims to generate the rectangles for the variable height and differentiates from the previous function by the insertion of another parameter: *depth*.

Indeed, what is important here are no more the width and the height of the rectangle, since are fixed to the cell periodicity (they're substituted by a single parameter that is the square side) but the depth of the rectangle (thickness). Respect to the previous function here is necessary the introduction of a third parameter in the square generation that will specify its z-coordinate, not considered before.

Then, the function used to generate the .dxf file is the same as that is B.2, but this time in mat_{len} are stored the heights of each block.

C SES generation

C.1 SES circular phase map evaluation

```
function phase_mapPW(f,p,D,num_el,angti,angfi,angtb,angfb)

%Function to evaluate the phase map for an incident plane wave

lambda=3e8/f;
k=2*pi/lambda;

%grid definition
[x y]=meshgrid(0:num_el,0:num_el);
x = (x(1:end, 1:end) + 0.5)*p;
y = (y(1:end, 1:end) + 0.5)*p;
cx=num_el*p/2;
cy=num_el*p/2;
d=sqrt((x - cx).^2 + (y - cy).^2); %distance from each element to the center

%Phasemap evaluation
w=0; %counter for the number of element

for i=1:num_el
    for j=1:num_el
        if(d(i,j)<D/2)
            psi(i,j)=rad2deg(-k*((x(i,j)*(sin(angti)*cos(angfi)+sin(angtb)*cos(angfb)))+(y(i,j)*(sin(angti)*sin(angfi)+sin(angtb)*sin(angfb)))));
            psi(i,j)=mod(psi(i,j),360);
            w=w+1;
        else
            psi(i,j)=NaN;
        end
    end
end
figure()
imagesc(psi)
title('Element␣phases␣of␣s21␣with␣angled␣beam␣[Âř]')
grid on
axis on
colorbar
colormap(hot)

```

```

end
```

Listing 5: Function to evaluate SES circular phase map

The proposed function, as the title suggests, allows to evaluate the phase map for a *circular* SES, therefore considering an infinite plane wave illumination. After the input of the parameters necessary to implement the equation 2.3, that are in the same order as they're reported: the frequency, periodicity, structure diameter, incicent angles θ_i and ϕ_i and scattering angles θ_b and ϕ_b.

As output the proposed function will provide a graphical representation of the map and the matrix *psi* that has stored all the values.

C.2 SES rectangular phase map evaluation

```

function [psi,map]=phase_maprect_PW(f,p,Nx,Ny,angti,angfi,
   angtb,angfb)

%Function to evaluate the phase map for an incident plane
   wave

lambda=3e8/f;
k=2*pi/lambda;

%grid definition
[x y]=meshgrid(0:Nx,0:Ny);
x = (x(1:end, 1:end) + 0.5)*p;
y = (y(1:end, 1:end) + 0.5)*p;

%Phasemap evaluation
w=0; %counter for the number of element

for i=1:Ny
    for j=1:Nx
            psi(i,j)=rad2deg(-k*((x(i,j)*(sin(angti)*cos(
               angfi)+sin(angtb)*cos(angfb)))+(y(i,j)*(sin(
               angti)*sin(angfi)+sin(angtb)*sin(angfb)))));
            psi(i,j)=mod(psi(i,j),360);
            w=w+1;
```

```
    end
end

figure()
map=imagesc(psi)
title('Element␣phases␣of␣s21␣with␣angled␣beam␣[Âř]')
grid on
axis on
colorbar
colormap(hot)

end
```

Listing 6: Function to evaluate SES rectangular phase map

The code is almost equal to the previous one and changes only in the input parameters, because now the diameter is no more needed and is substituted by N_x and N_y that represent the number of horizontal and vertical element respectively.

C.3 Research Algorithm for double parameter analysis

```

f=27e9;
p=0.5*3e8/f;
Nx=31;
Ny=40;
angti=0;
angfi=0;
angtb=degtorad(20);
angfb=0;
[psi,map]=phase_maprect_PW(f,p,Nx,Ny,angti,angfi,angtb,angfb);


%INTERPOLATION

s21ph = importfile('s21ph.txt',[3,36,69,102,135,168,201,234,267,300],[33,66,99,132,165,198,231,264,297,330]);
```

```
s21ph=reshape(s21ph,31,[]);

for i=1:10
    s21ph(:,i)=deg2rad(s21ph(:,i));
    s21ph(:,i)=unwrap(s21ph(:,i),pi);
    s21ph(:,i)=rad2deg(s21ph(:,i));
end

for i=1:31
    s21ph_inv(:,i)=s21ph(i,:);
end

s11amp_inv=importfile('s11ampinv.txt'
   ,[3:12:363],[12:12:372]);
s11amp_inv=reshape(s11amp_inv,10,[]);
d = importfile2('s11ampinv.txt',3, 12);
h = importfile3('s21amp.txt',3, 33);


for i=1:length(h)-1
    d_l=linspace(min(d),max(d),20);
    s21ph=spline(d,s21ph_inv(:,i),d_l);
    mat_s21(:,i)=s21ph';
end

for i=1:length(d_l)
    h_l=linspace(min(h),max(h),200);
    s21ph=spline(h(1:end-1),mat_s21(i,:),h_l);
    mat_s21_2(:,i)=s21ph;
end

figure()
for i=1:length(d_l)
    plot(h_l,mat_s21_2(:,i))
    title('s21␣phase')
    xlabel('H[mm]')
    ylabel('[Âř]')
    hold on
end

figure()
```

```
[X, Y] = meshgrid(d_l,h_l);
surf(X, Y, mat_s21_2);
xlabel('d[mm]')
ylabel('H[mm]')
zlabel('[Âř]')

for i=1:length(h)-1
    d_l=linspace(min(d),max(d),20);
    s11amp=spline(d,s11amp_inv(:,i),d_l);
    mat_s11(:,i)=s11amp';
end

for i=1:length(d_l)
    h_l=linspace(min(h),max(h),200);
    s11amp=spline(h(1:end-1),mat_s11(i,:),h_l);
    mat_s11_2(:,i)=s11amp;
end

figure()
for i=1:length(d_l)
    plot(h_l,mat_s11_2(:,i))
    title('s21␣phase')
    xlabel('H[mm]')
    ylabel('[Âř]')
    hold on
end

figure()
[X, Y] = meshgrid(d_l,h_l);
surf(X, Y, mat_s11_2);
xlabel('d[mm]')
ylabel('H[mm]')
zlabel('dB')


%%Length map
%check max difference between near values

for i=1:length(d_l)
    for j=1:length(h_l)-1
        err(j)=abs(mat_s21_2(j+1,i)-mat_s21_2(j,i));
```

```
    end
    max_d(i)=max(err);
end
max_s21err=max(max_d);

for i=1:length(d_l)
    for j=1:length(h_l)-1
         err(i)=abs(mat_s11_2(j+1,i)-mat_s11_2(j,i));
    end
    max_d(i)=max(err);
end
max_s11err=max(max_d);

for i=1:length(d_l)
    for j=1:length(h_l)
            mat_s21_2(j,i)=mat_s21_2(j,i)+360;
    end
end

figure()
[X, Y] = meshgrid(d_l,h_l);
surf(X, Y, mat_s21_2);
xlabel('d[mm]')
ylabel('H[mm]')
zlabel('[Âř]')


for i=1:Ny
    for j=1:Nx
          phaseval=psi(i,j);
          index=zeros(1,length(d_l));
          val=zeros(1,length(d_l));
          c=0;
           for k=1:length(d_l)
               err1(k)=min([abs(phaseval-min(mat_s21_2(:,k))
                  ),abs(phaseval+360-min(mat_s21_2(:,k)))]);
               err2(k)=min([abs(phaseval-max(mat_s21_2(:,k))
                  ),abs(phaseval+360-max(mat_s21_2(:,k)))]);
              if (phaseval<=max(mat_s21_2(:,k)) && phaseval
                 >=min(mat_s21_2(:,k))) || (phaseval+360<=
                 max(mat_s21_2(:,k)) && phaseval+360>=min(
```

```
                 mat_s21_2(:,k)))
               indice=find((mat_s21_2(:,k)>=phaseval-max_s21err/2 & mat_s21_2(:,k)<phaseval+max_s21err/2)|(mat_s21_2(:,k)>=phaseval+360-max_s21err/2 & mat_s21_2(:,k)<=phaseval+360+max_s21err/2));
                c=c+1;
                if isvector(indice)
                   index(k) = indice(floor(length(indice)/2) + 1);
                else
                    index(k)=indice;
                end
                val(k)=mat_s11_2(index(k),k);
              end
           end
         if c==0
            err_mat=[err1',err2'];
            [minin,ind]=min(err_mat);
            [minimum,indx]=min(minin);
            if indx==1
                mat_d(i,j)=d_l(ind(1));
                mat_h(i,j)=max(h_l);
                mat_s11amp(i,j)=mat_s11_2(end,ind(1));

            else
                mat_d(i,j)=d_l(ind(2));
                mat_h(i,j)=min(h_l);
                mat_s11amp(i,j)=mat_s11_2(1,ind(2));



            end
         else
        [minim,ind]=min(val);
        mat_d(i,j)=d_l(ind);
        mat_h(i,j)=h_l(index(ind));
        mat_s11amp(i,j)=mat_s11_2(index(ind),ind);
         end
    end
end

```

```
169
170 figure()
171 %pcolor(x,y,mat_len)
172 imagesc(mat_h)
173 grid on
174 axis on
175 title('Single␣element␣Length')
176 colorbar
177
178 figure()
179 %pcolor(x,y,mat_len)
180 imagesc(mat_d)
181 grid on
182 axis on
183 title('Single␣element␣d')
184 colorbar
185
186 %
187 % figure()
188 % %pcolor(x,y,mat_amp)
189 % imagesc(mat_amp)
190 % grid on
191 % axis on
192 % title('Single element amplitude')
193 % colorbar
194 %
```

Listing 7: Function to evaluate SES rectangular phase map

The code starts with the phase map evaluation made with C.2. After this an important interpolation phase in order to evaluate the surface has been carried. For both S_{21} and S_{11} the imported curves are been evaluated varying the two parameter, but in order to have a denser surface, is necessary to implement the interpolation for both the geometric parameters. This is done by re-organizing the imported file as a matrix, in which the rows report a variation respect parameter and the column respect to an other, therefore, the interpolation can be handled before for the rows and then for the columns.

Finally, at line 124 there the research algorithm is developed and is immediately possible to see that here the procedure is more compact than the previous one. It consists in simply evaluating 2 error vectors: $err1$ that will take the value of the difference between the current phase value needed and the minimum of the current column of the matrix in which the phase curves are stored (the difference is also done for the value increased of 360°) and $err2$ that instead, evaluates the difference with respect to the maximum value. In other words, since in each column is stored a phase curve obtained by means of a parameter variation, the general behaviour of the phase curve (after phase jump correction, if necessary) has a maximum and a minimum, one error is evaluated in relation to the first and the other error to the second.

The next step is to check if the current phase value is within the current curve and if it's true, into a variable *indice* are stored all the values present in the interval that has the phase value at the center and ± the half of the value which represent the maximum difference evaluated within two consecutive values (more detail about this are present in A). Notice that, here as for the error evaluations the check is made for the current phase value and the current value 360°. This is done for the reason why the phase not always is in the 0°-360°, so if necessary it is moved to positive values (line 110). However, this operation not ensure it again, indeed, the upper limit could be passed, for this reason is necessary to check values also for 360°.

As before, the parameter in line 134 could find different values in that interval and therefore the selected value will be the central one and will be stored in the *index* variable. At the end of this operation, the index will be used to find the correspondent value in the matrix that stores the s_{11} curves.

Very crucial is the definition of a *control variable* that's c, which is set to 0 at each cycle and it will be set to 1 if the there's a match in the considered curve. If no match occur for all the curves, this means $c = 0$ inside a matrix err_{mat} will be stored in first column err_1 and in the other err_2. The idea is clearly to select the value that provide the lowest error and for doing that, at line 146 are identified the minimum of each column and the index in which it can be found. Since the output will provide a minimum for each column, two values are given and again a selection of the minimum has to be performed. The output at line 147 will provide the absolute minimum in term of value and the index that tell if it belongs to $err1$ or $err2$. After these computations, the values of the geometric parameters selected can be stored in two matrices (mat_d and mat_h), while a third matrix (matS_{11} amp) will store the selected values for the reflection coefficient.

Now, since the reported code has been implemented for the structures proposed in section 4.5, in mat_d are stored the hole diameters, while in mat_h the height of each block.

Then, from lines 161 to the end of the algorithm, is reported what instead happens if at least on correspondence is found of the phase value inside the matrix that stores all the phase curves. Essentially, following the algorithm purpose, the minimum of the S_{11} stored in val is identified with its index and the values stored in the two matrices mat_d and mat_h will be filled with the related value.